STRUCTURE AND FUNCTION OF AIRWAY SURFACE LAYER OF THE HUMAN LUNGS & MOBILITY OF PROBE PARTICLES IN COMPLEX FLUIDS

Liheng Cai

A dissertation submitted to the faculty of the University of North Carolina at Chapel Hill in partial fulfillment of the requirements for the degree of Doctor of Philosophy in the Curriculum in Applied Sciences and Engineering

Chapel Hill
2012

Approved by:

Michael Rubinstein

Brian Button

Richard C. Boucher

Richard Superfine

Sergei Sheiko

ABSTRACT

LIHENG CAI: Structure and Function of Airway Surface Layer of the Human Lungs
& Mobility of Probe Particles in Complex Fluids
(Under the direction of Michael Rubinstein)

Numerous infectious particles such as bacteria and pathogens are deposited on the airway surface of the human lungs during our daily breathing. To avoid infection the lung has evolved to develop a smart and powerful defense system called mucociliary clearance. The airway surface layer is a critical component of this mucus clearance system, which consists of two parts: (1) a mucus layer, that traps inhaled particles and transports them out of the lung by cilia-generated flow; and (2) a periciliary layer, that provides a favorable environment for ciliary beating and cell surface lubrication.

For 75 years, it has been dogma that a single gel-like mucus layer, which is composed of secreted mucin glycoproteins, is transported over a "watery" periciliary layer. This one-gel model, however, does not explain fundamental features of the normal system, e.g. formation of a distinct mucus layer, nor accurately predict how the mucus clearance system fails in disease.

In the first part of this thesis we propose a novel "Gel-on-Brush" model with a mucus layer (the "gel") and a "brush-like" periciliary layer, composed of mucins tethered to the luminal of airway surface, and supporting data accurately describes both the biophysical and cell biological bases for normal mucus clearance and its failure in disease. Our "Gel-on-Brush" model describes for the first time how and why mucus is efficiently cleared in health and unifies the pathogenesis of major human diseases, including cystic fibrosis and chronic obstructive pulmonary disease. It is expected that this "Gel-on-Brush" model of airway surface layer opens new directions for treatments of airway diseases.

A dilemma regarding the function of mucus is that, although mucus traps any inhaled harmful particulates, it also poses a long-time problem for drug delivery: mobility

of cargos carrying pharmaceutical agents is slowed down in mucus. The second part of this thesis aims to answer the question: can we theoretically understand the relation between the motion of a probe particle and the local structure and dynamics of complex fluids such as mucus, or even one step back, simple polymer solutions and gels?

It is well known that the thermal motion of a particle in simple solutions like water can be described by Stokes-Einstein relation, in which the mean-square displacement of the particle is (1) linearly proportional to time and (2) inversely proportional to the bulk viscosity of the solution. We found that these two statements become questionable if the particle size is relatively small and the solutions become complex fluids such as polymer solutions and gels. The motion of small particles with size smaller than the entanglement length (network mesh size) of a polymer solution (gel) is sub-diffusive with mean-square displacement proportional to the square root of time at relatively short time scales. Even at long time scales at which the mean-square displacement of the particles is diffusive, the mean-square displacement of the particles is not necessarily determined by the bulk viscosity, and is inversely proportional to an effective viscosity that is much smaller than the bulk value.

An interesting question related to the particle motion in polymer gels is that whether particles with size larger than the network mesh size can move through the gel? An intuitive answer would be that such large particles are trapped by the local network cages. We argue that the large particles can still diffuse via hopping mechanism, i.e., particles can wait for fluctuations of surrounding network cages that could be large enough to allow them to slip though. This hopping diffusion can be applied to understand the motion of large particles subjected to topological constraints such as permanent or reversible crosslinked networks as well as entanglements in high molecular weight polymer solutions, melts, and networks.

Dedicated to

my parents, who are the reason for my existence;

my wife, for her wholeheartedly love and support;

my brother, for his cheering me up.

ACKNOWLEDGEMENTS

It is a great pleasure for me to record my appreciation to a number of individuals who have helped me either directly or indirectly, in achieving the task of initiating and completing this dissertation.

I would like to acknowledge, first and foremost, my thesis advisor, Prof. Michael Rubinstein. I am deeply indebted to him for his supervision, encouragement, patience, and rigorous yet pleasant training during these exciting five years, which have directly contributed to my general understanding of polymer physics, influenced my way of thinking about and performing scientific research, and brought me into the dazzling and exciting soft matter world. I decided to get involved into polymer physics after my undergraduate without knowing even what polymers are. It was Dr. Rubinstein who taught me in person, using his classical text "Polymer Physics", to build up my background in polymer physics through countless hours of face-to-face instructions and debates squeezed from his precious time. But without doubt he is a strict advisor, never accepting any ambiguous speculations or arguments, leaving me no choice but to refine my work to seek for precise presentations. But he never pushes, allowing me to ponder the questions, seek for best solutions, and offering timely and enlightening directions. Numerous scenarios pumped out of my head are that he was standing in front of a big whiteboard, explaining problems by waving his big yet cute arms trying to visualize the physical pictures; helping me go through each line of the papers I wrote, every slide of the presentations I prepared, and every statement I attempted to make. But what he did is way beyond what I can mention here. He cares about students. He encouraged me to communicate with other scientists, provided me opportunities to know them in person, and helped me initiate collaborations with them. It can never be overstated that he is a leading and standard example of how to combine research of highest standard with a kind-hearted attitude.

Time back to 2007. I still remember the first day when I came to Chapel Hill, I visited Dr. Rubinstein in his office, saying that I would like to have some experience in experiments besides theory. One can imagine how impractical that could be for a theoretical group, and this pursue had not come to be true until almost two years later. I can never forget that it was a very hot summer afternoon, Dr. Rubinstein brought me in person to Prof. Brian Button's laboratory on the other side of the campus in Cystic Fibrosis Center, in which Prof. Richard C. Boucher was the director.

Not formally appointed as such, Prof. Button, together with Prof. Boucher, acted as co-supervisors and played an important role that can never be exaggerated in my experimental project. Dr. Brian trained me hand-by-hand how to deal with cells, operate microscope, design experimental apparatus for specific needs, and more than the technical side, influenced me directly on personal aspects such as how to communicate and present. It was Dr. Button who introduced me to other labs around the research center, provided me freedom to use any lab resources to purse intellectual challenges, spared his precious time to discuss with me about any experimental results I had. Countless discussions and debates happened, and a lot of times, with the participation of Dr. Rubinstein and Dr. Boucher. Dr. Boucher is such a knowledgeable professional knowing every corner of the whole field, that always has a great vision on pointing the experiments to the eventually proofed right directions, gluing efforts from various aspects to achieve the final goal. I did benefit tremendously from the way he thinks about science; the way he handles questions and problems, either from the scientific or non-scientific side.

I would say I am the luckiest guy fortunate enough to have such great mentors.

This is not all yet, as I would have never succeeded without the help of current and former members in Dr. Rubinstein's group, fellows at Cystic Fibrosis Center, and professors around the department. I am grateful to Dr. Sergey Panyukov for his insightful discussions and significant contributions to the second part of my dissertation. He is such a great professional with incredible capability to transform physical pictures to rigorous yet elegant mathematical forms, and of course, always easy and friendly to talk

TABLE OF CONTENTS

LIST OF TABLES

LIST OF FIGURES

xvi

Part I

Structure and Function of Airway

Surface Layer of the Human Lungs

CHAPTER 1

INTRODUCTION

The primary physiological role of the lung is a gas exchanger. In order to support the metabolic activities of the organism it has to deliver O_2 from the environmental air into the blood and remove CO_2 from blood. [1, 2] The amount of gas exchanged by the lung ranges between 40 and 800 liters per hour in humans depending on body size and physical activity. [3]
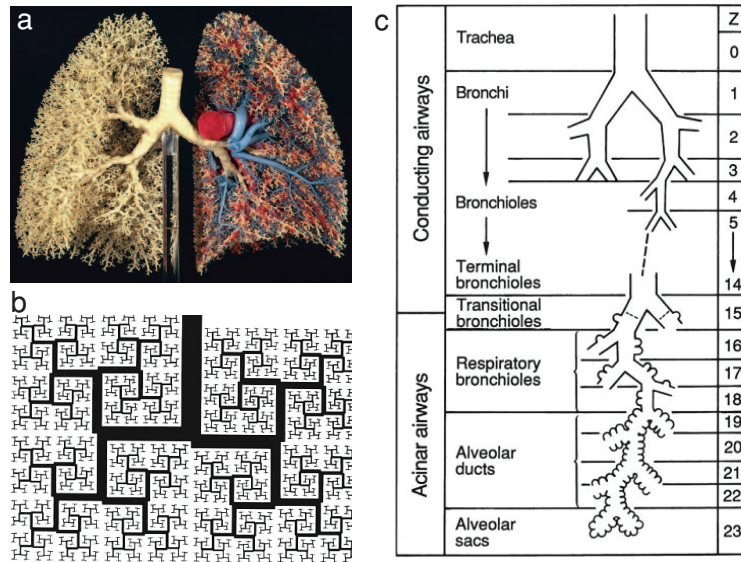
Figure 1.1: Fractal structure of the human lung. a, A resin cast of human lung [4]; b, Fractal tree of Mandelbrot [5]. c, Model of airway branching in human lung from trachea (generation $z = 0$) to alveolar (generations $z = 20$ to 23) [1].

The lung is structurally optimized for the most efficient delivery of such a large amount of fresh air. The structure of the lung resembles the self-similar fractal tree (Figure 1.1), which has on average 23 generations of dividing airways starting from the trachea, branching through the bronchi, the bronchioles, and ending at the alveoli . [1, 4, 6, 7] This self-similarity of the airway tree minimizes air resistance, establishes

sufficiently large surface of contact between air and the blood, optimizes packing of this fractal tree structure into the lung. [1] This smart design makes the lung a perfect gas exchanger allowing delivery of large amount of air to all alveoli at the same time and in approximately the same amount, but it also brings the lung to a variety of risks.
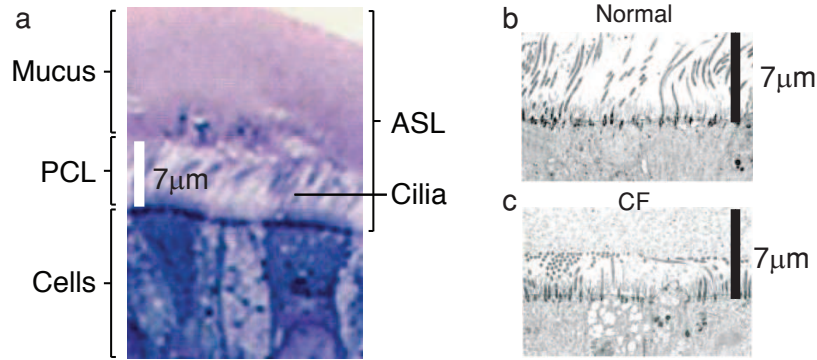
Figure 1.2: Components of the human airway surface layer (ASL). a, Light microscopy view of the airway surface layer (ASL), comprising of the mucus layer and the periciliary layer (PCL). Cells were fixed with Osmium Tetraoxide in perfluorocarbon, Epon-embedded, and stained with Richardson's [8]. b, c, Fine structure of mucus/PCL interface in normal (b) and cystic fibrosis (CF) (c) cultures. Normal and CF cultures were fixed at 24 hours with perfluorocarbon (PFC)/Osmium tetroxide (OsO4) and examined under low-power transmission electron microscope (TEM) (adapted from ref. [9]). The PCL for normal people has a thickness about 7 μm (b), whereas it is collapsed for cystic fibrosis (CF) patients.

The extensive gas exchange process exposes the lung, especially the epithelial surface of the conducting and respiratory airways (Figure 1.1c) between the trachea and the alveoli, to a tremendous amount of infectious and toxicant particulates. In addition to gas exchange, therefore, it is necessary for the lung to develop defense mechanisms to protect it from harmful substances.

One of the primary defense mechanisms of the lung is mucociliary clearance (MCC). [10–13] The airway surface layer (ASL) is a critical component of the mucociliary clearance system. It consists of two parts [14–16]: (1) a mucus layer, that traps inhaled particles and transports them out of the lung by cilia-generated forces; and (2) a periciliary layer (PCL) that provides a favorable environment for ciliary beating and cell surface lubrication (Figure 1.2a). The critical importance of the MCC is illustrated by

its failure in human lung disease, including primary cilia dyskinesia (PCD), in which cilia do not beat and patients have to rely exclusively on coughing to clear mucus, chronic obstructive pulmonary disease (COPD) [17], and cystic fibrosis (CF) with PCL collapsed (Figure 1.2c) [18]. All these diseases are characterized by "dehydrated" airway surface layer, with mucus concentration several times higher than in normal mucus [19, 20], and mucus adhering to epithelial cells [21, 22].

Despite studies linking increased mucus concentration to the pathogenesis of airways disease, e.g., reduced rates of mucus clearance [23], inflammation [24], and infection [25], the absence of quantitative models makes it impossible to predict when mucus clearance fails and to develop novel therapies to treat this aspect of lung disease [3, 16]. In the first part of the thesis, we develop a model for the ASL on the molecular level to understand the physical reasons of mucus clearance. This model is based on the accurate description of the PCL structure and an understanding of the functional interactions between the PCL and the overlaying mucus layer.

In our new model, a gel-like mucus layer, with its physical properties determined by gel-forming mucins, is laying over a brush-like PCL, in which tethered mucins are grafted to cilia and epithelial cell surface. At least two physiologically important features of the brush-like PCL were identified and tested by experiments. The first one is that, in addition to the mucus barrier, the brush-like structure equips the PCL a further protective layer in preventing external objects with size much smaller than bacteria from approaching epithelial cell surface. The second one is the strong repulsion between the tethered mucins within the PCL makes the PCL an osmotically stiff gel. This osmotic stiffness stabilizes the PCL from the osmotic compression by mucus, which is critical for maintaining effective mucus clearance.

The first part of the thesis is structured as follows. Chapter 2 discusses the current understanding of the composition of ASL and physical properties of the major components in the ASL. A molecular model for the structure of ASL is proposed and discussed in chapter 3. In this chapter, after identifying the limitations of the tradi-

tional "gel-on-liquid" model of ASL, in which a mucus gel moves over a liquid like periciliary layer, we propose a novel "Gel-on-Brush" model as mentioned above supported by experiments. Following the experimental evidence we present quantitative analysis of the structure of the ASL using the knowledge of polymer physics. Chapter 4 links the predictions from the "Gel-on-Brush" model to the reasons for chronic lung diseases based on quantifying the osmotic properties of PCL, which is indirectly measured by challenging the PCL utilizing mucus/mucus simulants with known osmotic properties. At the end of this part (chapter 5), we highlight the key features of our new "Gel-on-Brush" model, summarize the physical understanding of chronic lung disease, and propose directions for the development of novel treatments of the lung diseases.

CHAPTER 2
COMPOSITION OF AIRWAY SURFACE LAYER

The airway surface layer consists of two parts: the mucus layer and the periciliary layer. Each of them corresponds to an emerging broad and active research area with lots open questions and readers are referred to the cited references for more discussions. The purpose of this chapter is to outline the properties of the major components of airway surface layer that are necessary for understanding the work presented in the first part of this dissertation.

2.1 Mucus: properties of mucins

Mucus is a viscoelastic gel with properties of both soft elastic solids like rubber and viscous liquids like water. The main component of mucus is water, which accounts for 98% for healthy and 92% or less for CF. The rest of mucus is solids, including mucins, non-mucin proteins, lipids, DNA, actin filaments, and salts. [26, 27]

Mucins are complex glycoproteins synthesized by the goblet cells of the airway surface epithelium and the submucosal glands. They are classified according to their MUC genes, which are localized to chromosomes 1, 3, 4, 7, and 19. [28]. The mucins are responsible for the principle structure and properties of mucus and account for up to 30% of the solid content of mucus. [13, 28–30] The non-mucin proteins including secretory IgA immunoglobulins, lysozyme, and lactoferrin could serve defensive purposes. For instance, secretory IgA immunoglobulins form an immunological barrier whose importance is appreciated by the increased susceptibility of infections of lung for patients with deficiency in IgA. [31] Lysozyme and lactoferrin are bactericides. [32, 33] The lipids in mucus could be secreted by the goblet cells of the airway surface epithelium

and the submucosal glands [34] and produced through cytochemistry [35]. The content of lipids may affect the adhesive properties of mucus. [36] The DNA and actin filaments are from cellular debris including bacteria, luminal leukocytes, and epithelial cells. [3] The salts account for 0.9% of the total mass of the mucus.
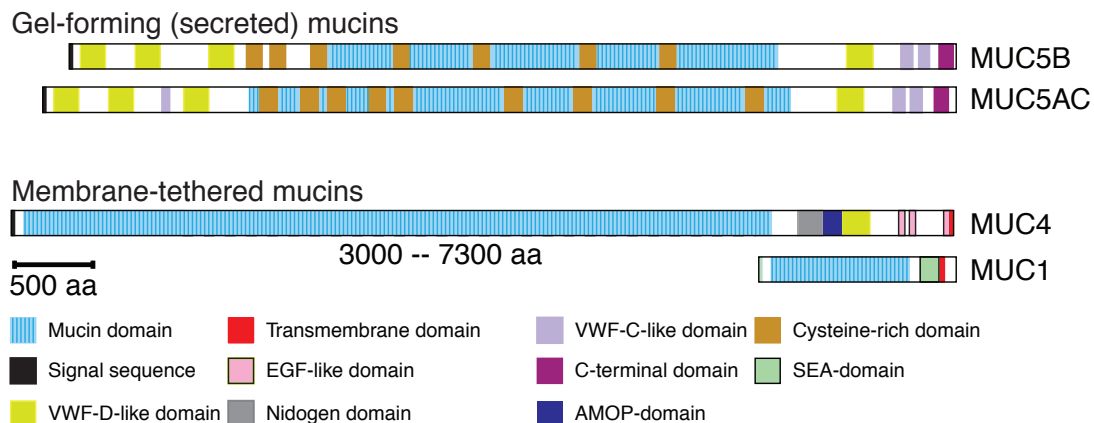
Figure 2.1: The major structural domains of some airway mucins. Gel-forming (secreted) mucins: MUC5AC and MUC5B; membrane-tethered mucins: MUC1 and MUC4. vWF-D and C-like domains are present in the von Willebrand factor glycoprotein, which is a large, disulfide-linked, polymeric glycoprotein that is produced in endothelial cells and is essential for blood clotting[37]; SEA (sea urchinsperm protein, enterokinase, and agrin) domain: a structural motif found in highly O-glycosylated membrane proteins that is cleaved and then reassociates via noncovalent bonds to which numerous carbohydrate chains (O-glycans) are covalently attached via the linkage sugars[30]; AMOP: adhesion associated extracellular domain; EGF: epidermal growth factor-like domains; nidogen-like domain: an extracellular domain in nidogen, a sulfated glycoprotein which binds to collagen IV and is tightly associated with laminin [38]; PTS: proline, threonine, serine-rich domains. aa denotes amino acid. (Models primarily adapted and modified from refs. [28, 30, 39, 40].)

All mucin molecules have at least one large mucin domain (Figure 2.1). The mucin domain is characterized by its large polypeptide backbone (with molecular weights ranging from 0.5×10^6 Da to 20×10^6 Da [41, 42]), which contains regions rich in serine and threonine residues (see insert of Figure 2.2). Numerous sugar chains are covalently linked to the hydroxyl groups of the serine and threonine residues via the linkage sugar N-acetylgalactosamine (GalNAc). Those carbohydrate chains, also referred to as oligosaccharides or named O-glycans, have the number of sugar residues varying between 1 and 20 per chain. [43, 44] As a consequence, the heavily O-glycosylated

mucin domain is negatively charged, due to the presence of sialic acid residues (N- or O-substituted derivatives) and to the frequent present of sulfate easter residues attached to carbohydrate chains, and about 70% of the dry weight of mucins are carbohydrates. [13]
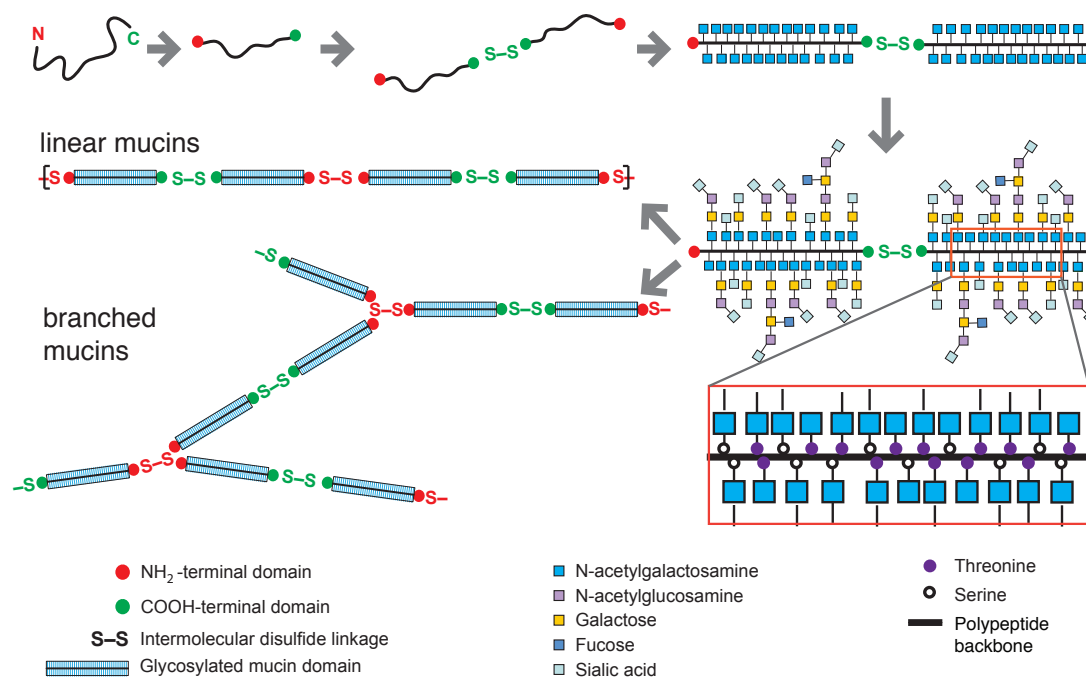
Figure 2.2: Cartoons illustrating the assembly and polymerization procedures of mucins. The translated mucin polypeptide undergoes N-glycosylation and intramolecular disulfide bond formation; A dimer is formed via intermolecular disulfide linkage; N-acetylgalactosamine (GalNAc) is added to serine and threonine residues, which are located primarily in the mucin domains; These glycan chains are further elaborated by adding sugar residues; The mucin dimers polymerize via intermolecular disulfide linkage; Linear and branched mucins could be produced. (Models primarily adapted and modified from [28, 30].)

A mucin domain consists of many macromonomers. A macromonomer contains several globular regions separated by a highly charged dense molecular brush with side chains (cross-section) of ~ 5 nm (see inset in Figure 2.2). A pair of macromonomers forms a dimer by a disulfide link between their COOH terminal domains (red circles in Figure 2.2). Dimers polymerize into very large mucins through disulfide bonds between NH_2 terminal domains (green circles in Figure 2.2). The resulted mucins could be linear or branched depending the polymerization mechanisms. [30]

According to their functions in airways surface layer mucins can be broadly classified into gel-forming (secreted) mucins, such as MUC5B and MUC5AC, and transmembrane mucins, such as MUC1, and MUC4 (Figure 2.1). The gel-forming mucins are the major contributors to the structure of mucus and therefore its viscoelastic properties, because they can form associations with each other and with other proteins. [45] These associations can be altered by chemical reagents such as surfactants, as well as by pH [46] and temperature, which consequently lead to the change of viscoelastic properties of mucus. Although the bulk viscoelastic properties mucus can be measured via conventional rheometer and microrheology [47] (see part II), the understanding of polymeric properties of its major components—gel-forming mucins—is far from completeness, partly due to the difficulty in isolation and purification of mucins [48] and the complexity of the mucin molecules themselves.

Typically the studies of mucins are performed after extraction and purification, using highly denaturing solvents (such as 6-M guanidinium chloride) to solubilize mucus. [41, 42, 49–53] Therefore, although we have a relatively good understanding of mucins in their denatured state, this does not necessarily represent either the native conformation or the interactions between these molecules within the mucus. The purified mucins are typically characterized by techniques such as gel permeation chromatography (GPC) [49], light scattering [49], transmission electron microscopy (TEM) [54], and atomic force microscopy (AFM) [55]. The studies of purified mucins suggest that the average molecular weight of a MUC5B mucin molecule is about 150×10^6 Da and its average radius of gyration is 150–250 nm. [56–59] It was claimed that MUC5AC has a molecular weight of $\sim 50 \times 10^6$ Da obtained from GPC characterization and a contour length on the order of 10 μm as measured by electron microscopy, whereas using light scattering one obtains the average radius of gyration in solution about ~ 140 nm. [42, 58]

In polymer physics one can relate the radius of gyration R_g of polymers to their molecular weight M by a scaling law: $R_g \approx b \, (M/M_0)^{\nu}$, in b is the Kuhn length

describing the stiffness of the polymer, M_0 is the mass of a Kuhn segment, and ν is the scaling exponent. [60] Larger values of Kuhn length correspond to stiffer polymers. The Kuhn length b for mucin molecules is estimated to be between 10 and 15 nm [61]. The scaling exponent ν was thought to be about 0.55 in dilute solutions [26] for MUC5AC, suggesting that mucin molecules are random linear coils. Recent experiments suggest the exponent $\nu \simeq 0.69$ for MUC5AC [42], whereas it is slightly smaller for MUC5B ($\nu \simeq 0.62$) [58]. Yet some other works [62] indicate the same scaling exponent $\nu \simeq 0.62$ for both MUC5AC and MUC5B. Such inconsistency among the studies on mucin molecules implies that the understanding of their physical properties is far from conclusive.

The trans-membrane mucins have a special transmembrane domain allowing them to graft to the plasma membrane. The trans-membrane mucins are found to express to the apical surface of epithelial cells. The contour length of mucins with trans-membrane domain is ~ 0.1 μm (MUC1) and ~ 1 μm (MUC4). [40] The size of trans-membrane mucins in solution is much smaller than their contour length. It was thought that MUC4 protein could extend up to ~ 300 nm. [40] However, exact values have not been reported so far to my knowledge. In this dissertation we provide experimental evidence supporting that MUC1 is primarily localized within the bottom of the PCL, with a likelihood grafting to epithelial cells, microvilli and cilia, and MUC4 is distributed throughout the whole space of the PCL and is primarily grafted to cilia (see chapter 3).

2.2 Periciliary layer (PCL): structure and function of cilia

The most visible objects in periciliary layer are cilia (see Figure 2.3a, b). Cilia are cylindrical structures, with a cross-sectional diameter of ~ 200 nm and length ~ 7 μm [63], extended from the apical epithelial surface of the ciliated columnar cells. Each ciliated epithelial cell supports approximately 200 cilia at a density of ~ 8 cilia/μm^2 [63], suggesting that the space between two neighboring cilia is ~ 200 nm. Short

microvilli, with length of $\sim 1\ \mu$m and diameter of ~ 100 nm [64], cover ciliated cells as well as non-ciliated columnar cells that separate ciliated epithelial cells from each other. [3] The movement of the cilia is characterized by a beating frequency ~ 15 Hz under normal conditions, but varies with temperature [65, 66], pH and salt concentrations [67], with the alteration $3 - 5$ Hz. The motion of each cilium is coordinated with others to generate metachronal waves [68], which is thought to be important for propelling the mucus layer with a steady transport rate $\sim 60\ \mu$m/s [18]. The beating cilia in the periciliary layer of respiratory airways belong to the class of so-called motile cilia (the other class of cilia is termed non-motile and will not be discussed here). The research of cilia itself is a rapidly growing and exciting field and readers are referred to reviews [62, 69–74] and the references therein for detail discussions of the structure and function of cilia as well as their relation to various diseases.).
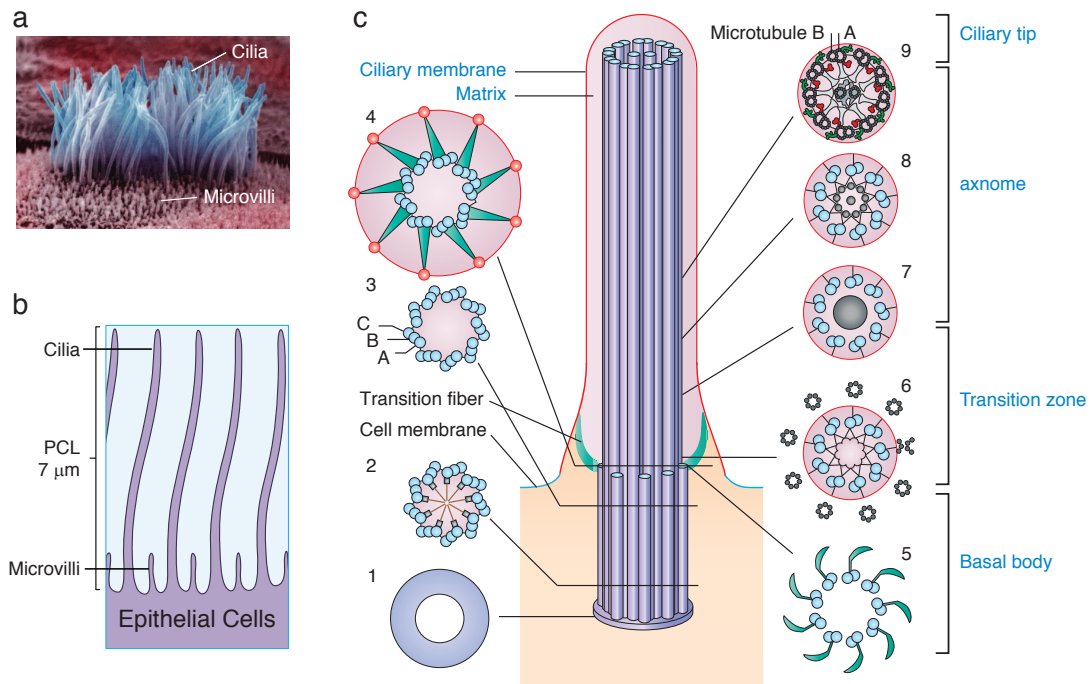
Figure 2.3: Composition of periciliary layer and structure of cilia. a, Scanning electron micrographs (SEMs) of respiratory cilia (long cylindrical objects) and microvilli (small protrusions) [75]; b, Cartoon illustrating the composition of periciliary layer based on its SEMs (a); c, Six sub-compartments of a cilium (modified based on models from refs. [62, 69, 73]).

A cilium can be structurally divided into six sub-compartments that include the cil-

iary membrane, axoneme, the matrix between ciliary membrane and axoneme, ciliary tip, transition zone, and basal body (see Figure 2.3c). The ciliary membrane is continuous with but distinct from the cell membrane. [76] It contains many receptors and channels that are thought to equip the cilium sensory function. [71]

Underlying the ciliary membrane is a cylindrical array of nine doublet microtubules called axoneme (see Figure 2.4), which provides the structural support for the cilium function. Each doublet is composed of one complete microtubule A made of 13 protofilaments and the other partially complete microtubule B made of 11 protofilaments. These two microtubules share part of their walls with each other, "glued" together via tubulin [77] and possibly additional protein factors such as tektin [78].

The cilia beating is powered by dynein motors [79–81] with the "fuel" supplied through hydrolysis of adenosine triphosphate (ATP). The dynein motors are anchored to microtubule A of each doublet with their motor heads contacting the microtubule B in the neighboring doublet. They are assembled into large complexes called dynein arms, which are arranged along the doublet with a precise periodicity (24 nm periodic spacing for outer dynein arm (green) and 96 nm spacing for inner dynein arms (red); see part 9 in Figure 2.3c and Figure 2.4 for detail illustration), generating force to slide one doublet against another. The sliding of doublets would not generate cilia bending without the help of nexin, which is a flexible protein linking the nine outer doublets (see Figure 2.4). The nexin is thought to prevent microtubules in the outer layer of the axoneme from movement with respect to each other and thus it converts doublet sliding into axoneme bending [82–85].

In addition to the nine outer doublets, the axoneme also contains a central pair of singlet microtubules, which is surrounded by a fibrous sheath. The central pair is connected with the nine outer doublets via a protein complexes called radial spokes. The radial spokes are believed to influence the exact cilia bending pattern via linking the position of central pair to the rhythmic activation of dynein arms. [86]

12
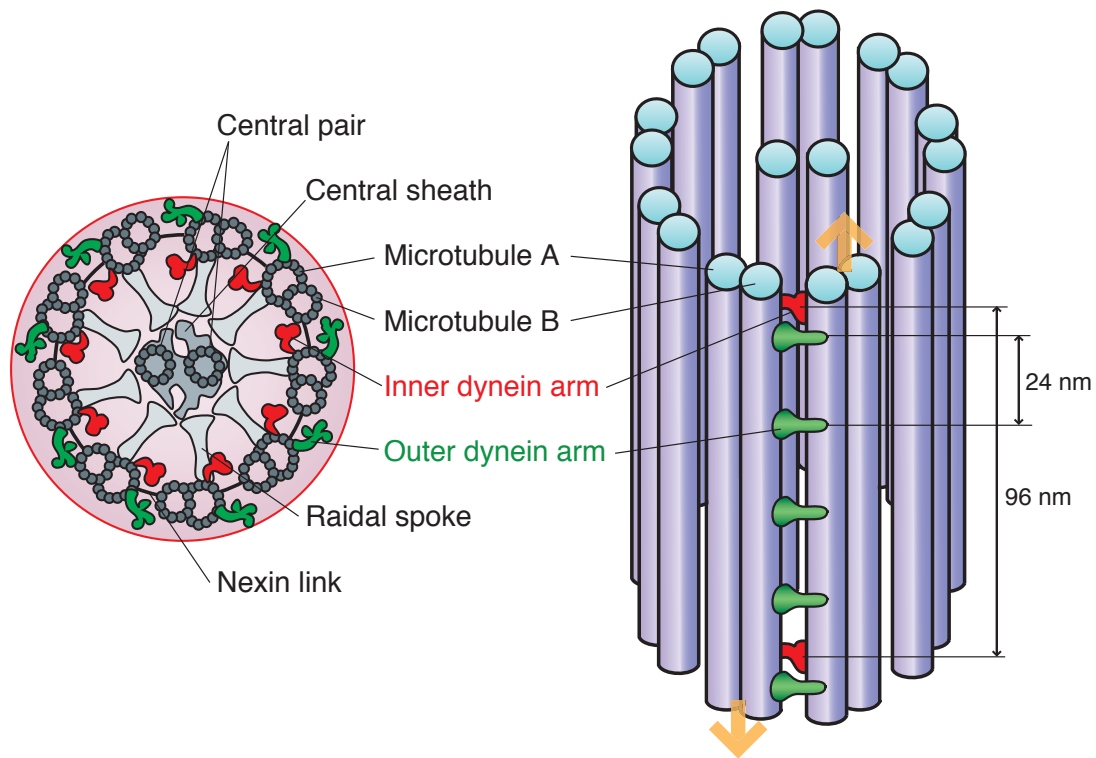
Figure 2.4: Ultrastructure of the axoneme of a cilium as a complementary illustration of part 9 in Figure 2.3.

Between the ciliary membrane and the axoneme is a fluid-like matrix. This matrix contains the intraflagellar transport machinery [62, 87–89], which is necessary to assemble and maintain the structure of cilium, employing the anterograde (kinesin) and retrograde (dynein) motors to transport axonemal subunits from the cell body to the tip of the cilium and return them to the cell body, respectively.

The kinesin motor can change to dynein motor (vice versa) and it is believed that the switch between the kinesin and dynein motors is located at the ciliary tip [73], whose detailed structure and function remain unknown. In addition to providing a switch between the kinesin and dynein motors, it is also thought that the tip of cilium might contain a structure that anchors the central pair of the axoneme to the ciliary membrane and harbors the ends of microtubule A in the axoneme. [90, 91]

At the other end of the axoneme is the basal body [69] (parts 1–4 in Figure 2.3c). The basal body is a specialized centriole and serves as the foundation upon which the

cilium is constructed. A cilium grows from the distal end of the basal body, with the doublet microtubules in the axoneme directly nucleated by the microtubules found in the basal body. Unlike the doublet microtubules in axoneme, the basal body contains a short cylindrical array of nine triplet microtubules (part 3 in Figure 2.3c). Each triplet is composed of one complete microtubule A, and two partially complete microtubules B and C sharing their walls with adjacent microtubules. The nine triplet microtubules are connected into a pinwheel like structure (part 4 in Figure 2.3c) at the distal of the basal body, change to a structure lacking appendages at the middle of the basal body (part 3 in Figure 2.3c), transform to a cartwheel structure (part 2 in Figure 2.3c) before embedding into a ring-like amorphous disc [92] at the extreme proximal end of the basal body (part 1 in Figure 2.3c), which is thought to play a role in the early stage of the duplication of basalbodies [93].

The junction between the axoneme and the centriole-derived part of the basal body is called the transition zone [94] (parts 5–8 in Figure 2.3c), which converts the triplet microtubular structure of the basal body into the axonemal doublet structure. Although the structure of the transition zone is not well characterized [95], several general features of the transition zone have been speculated. The transition zone has a characteristic structure known as transition fibers (see green sickle-like structure in Figure 2.3c), which are believed to demarcate the cytoplasmic and cilium compartments [62]. The boundary between the two compartments (transition fibers) is believed to be the docking sites for intraflagellar transport machinery. [96] It is also thought that the transition fibers could connect each microtubule doublet to the ciliary membrane, shown by parts 4 and 5 in Figure 2.3c. The distal part of transition zone contains stellate fiber arrays (small gray circles in parts 6 and 8 in Figure 2.3c) and an amorphous disk structure (the large gray circle in part 7 in Figure 2.3c), which may be the source from which two central singlet microtubules in the axoneme are formed. [69, 73, 97]

In brief, cilia are a class of sophisticated biological machinery with lots of unknown yet interesting questions regarding their ultrastructure and function of their sub-

compartments. However, some important functionalities of motile cilia have been identified and widely accepted. For instance, one of the main functions of the airway cilia is to provide driving force for the mucus clearance. In this dissertation we aim to understand the relation between the hydration state of the periciliary layer, within which the airway cilia are localized and beating, and the effectiveness of mucus clearance.

CHAPTER 3
STRUCTURE OF AIRWAY SURFACE LAYER

In chapter 2 we have briefly reviewed the compositions of the two major components, mucus and periciliary layers, of the human airway surface. In this chapter we focus on the structure of the airway surface layer, especially the periciliary layer.

We first present experimental evidence that suggests the limitations of traditional "Gel-on-Liquid" model considering the periciliary layer as a low viscosity liquid layer, then propose a novel "Gel-on-Brush" model considering the periciliary layer as a brush-like layer with bio-macromolecules tethered to cilia and epithelial cells. The biophysical properties, such as mesh size, of the proposed brush-like periciliary layer is quantified using a "dual-labeling" technique. The mesh size distribution within the periciliary layer is calculated using basic concepts and methods of polymer physics. The important features of this brush-like periciliary layer are highlighted at the end of this chapter.

3.1 Traditional "Gel-on-Liquid" model of the airway surface layer is qualitatively incorrect

Based on a variety of visualization approaches (e.g., Figure 1.2a) and the presumed requirement for a low viscosity liquid layer to facilitate ciliary beating, the mucociliary clearance system has been traditionally represented by a "Gel-on-Liquid" model [98][99–101] (Figure 3.1a), in which the "gel-like" mucus layer is propelled by cilia beating in a "watery" periciliary, i.e. "sol", layer [102]. However, the current "Gel-on-Liquid" model does not adequately explain why there are two layers, i.e. why the major macromolecules within mucus, the gel-forming mucins [28–30, 56, 59, 103] MUC5AC and MUC5B with hydrodynamic diameters ranging from 150 to 200 nm [42, 53], do

not penetrate into the 200 nm space between cilia in the PCL. In fact, this 200 nm interciliary space appears to be impenetrable to objects significantly smaller than mucins. For example, fluorescent beads with diameter of 40 nm are excluded from the PCL whereas only much smaller probes (green fluorescently-labeled albumin, with a hydrodynamic diameter of 6 nm [104]) penetrate the PCL (Figure 1.2b, c). It has been proposed that formation of a distinct mucus layer simply reflects the thixotropic actions of beating cilia [98, 105]. However, the observation that 40 nm particles are also excluded from the PCL when cilia beating was arrested, argues against a thixotropic mechanism of the formation of a distinct mucus layer (Figure 1.2d, e). Collectively, these data demonstrate that the "Gel-on-Liquid" model of the airway surface layer is qualitatively incorrect.

3.2 Novel "Gel-on-Brush" model of the airway surface layer

We propose a novel "Gel-on-Brush" model of ASL postulating that the PCL contains membrane-spanning mucins and large mucopolysaccharides that are tethered to cilia, microvilli, and epithelial surfaces (Figure 3.2a) [40]. We postulate that these tethered glycoproteins form an extracellular brush with a sufficiently high concentration to establish a mesh that prevents both MUC5AC and MUC5B mucins from the mucus layer and inhaled particles depositing on the airway surface from penetrating the PCL and reaching the cell surface. Further, we predict that the relatively high concentration of mucins in this extracellular brush produces inter-molecular repulsions within this layer, which stabilizes the PCL against compression by an osmotically active mucus layer. Key features of this new model were tested by: 1) identifying tethered macromolecules in the PCL; 2) measuring the mesh size of the PCL; and 3) measuring important biophysical properties of this layer, e.g., its osmotic modulus, and comparing them with the corresponding properties of the overlying mucus layer.
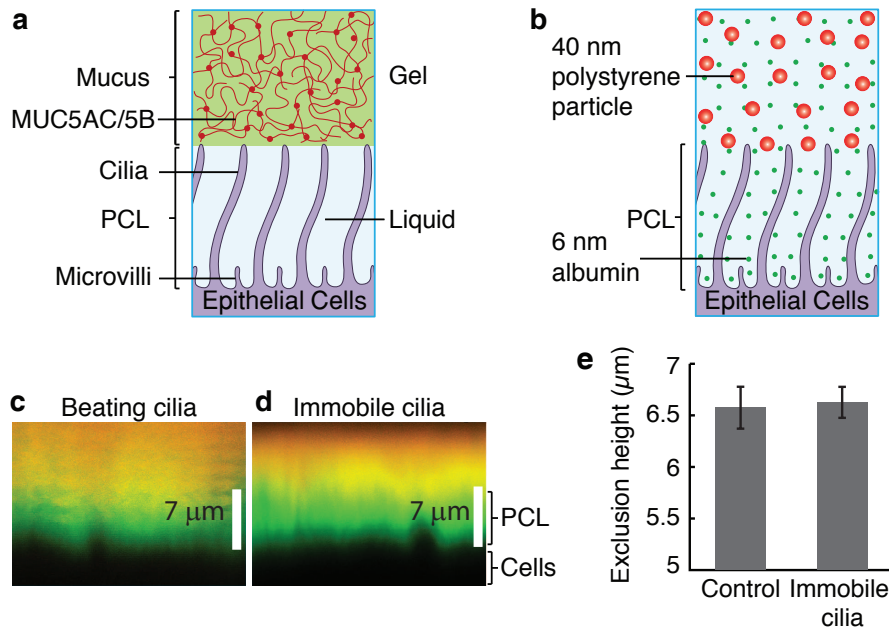
Figure 3.1: The periciliary layer is not a simple liquid layer. a, Schematic representation of the traditional Gel-on-Liquid model showing a mucus layer (comprised of gel-forming mucins, MUC5AC and MUC5B) and the PCL being a liquid-filled domain. b, Schematic illustration showing penetration of small ($d \approx 6$ nm[104]) fluorescently-labeled albumin (green) into the PCL, whereas 40 nm polystyrene particles (red) are completely excluded from the PCL. c, d, Representative XZ confocal images of well-differentiated HBE cultures with normally beating cilia (c) and paralyzed, i.e., immobile, cilia (d) (pre-treated for 10 minutes with 1% isoflurane to produce reversible ciliastasis[106]). Here, the exclusion zone (green region) was accessible to the green albumin, but not the larger particles, while the yellow region was accessible to both. Note: the wavy streaks in image d are an artifact of beating cilia during image acquisition. Scale bars = 7 μm. e, Summary plot showing the exclusion thickness of 40 nm particles for cell cultures with beating and non-beating (immobile) cilia.

3.2.1 Evidence for a macromolecular mesh in the PCL

Utilizing rapid freezing techniques coupled with electron microscopy, an electron-dense meshwork with apparent mesh sizes on the order of $\sim$ 20–40 nm was observed in the PCL region of human bronchial epithelial (HBE) cell cultures (Figure 3.2b, c). Unlike the overlying mucus layer, this PCL mesh could not be extracted by vigorous washings expected to remove adherent secreted mucins. We, therefore, hypothesized that the large macromolecules, such as membrane-spanning mucins (MUC1, MUC4, MUC16, and MUC20 [40, 107]) and tethered mucopolysaccharides (e.g., heparin sul-
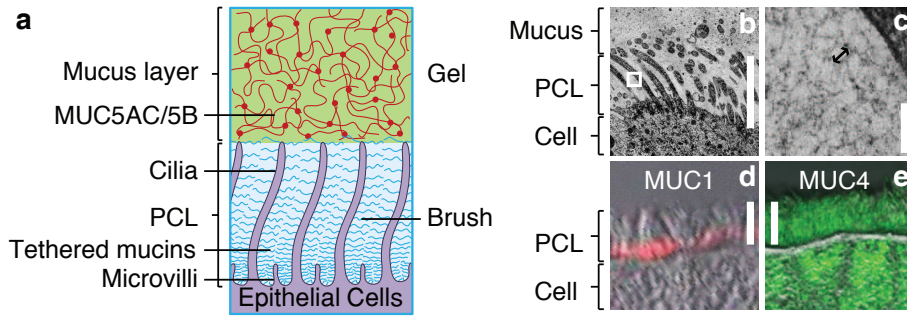
Figure 3.2: Gel-on-Brush model of the PCL. a, Schematic representation of the Gel-on-Brush hypothesis of the periciliary layer: tethered macromolecules, such as membrane-bound mucins, form a brush-like structure of the PCL. b, c, Morphological evidence for the Gel-on-Brush model is revealed by rapid freeze imaging of HBE cultures exhibiting extensive mesh-like structure with mesh (depicted by the arrow in c) on the order of $20 - 40$ nm in the PCL. d, e, Immunological evidence showing the presence of tethered mucins on freshly excised human airway tissue: MUC1 (red) is located at the bottom of the PCL (d) and MUC4 spans the whole PCL (green, e). Scale bars in b, d, and e $= 7$ μm, bar in $c = 100$ nm, double-head arrow in $c = 30$ nm. White box in b denotes area of magnification.

fate [108]), occupy the interciliary space of the PCL. Indeed, immunohistochemistry studies of freshly excised human airways identified several of these membrane-bound macromolecules, including mucins MUC1 (Figure 3.2d) and MUC4 (Figure 3.2e) and heparan sulfate (not shown), attached to cilia, microvilli, and the cell surface of conducting airway surfaces.

3.2.2   Quantification of the mesh size in the PCL

Mesh size is a parameter that describes important physical properties of polymer solutions, gels, and brushes, including their permeability to particles/macromolecules and their osmotic pressure. In polymer physics, the mesh size, called the correlation length ξ, is defined as the average distance between nearest segments of neighboring macromolecules [60]. Images of the PCL generated from the rapid fixation/EM approach (Figure 3.2b, c) may not provide reliable values of mesh size due to fixation and staining artifacts. Therefore, a technique was developed to quantify the PCL mesh size in living HBE cultures.
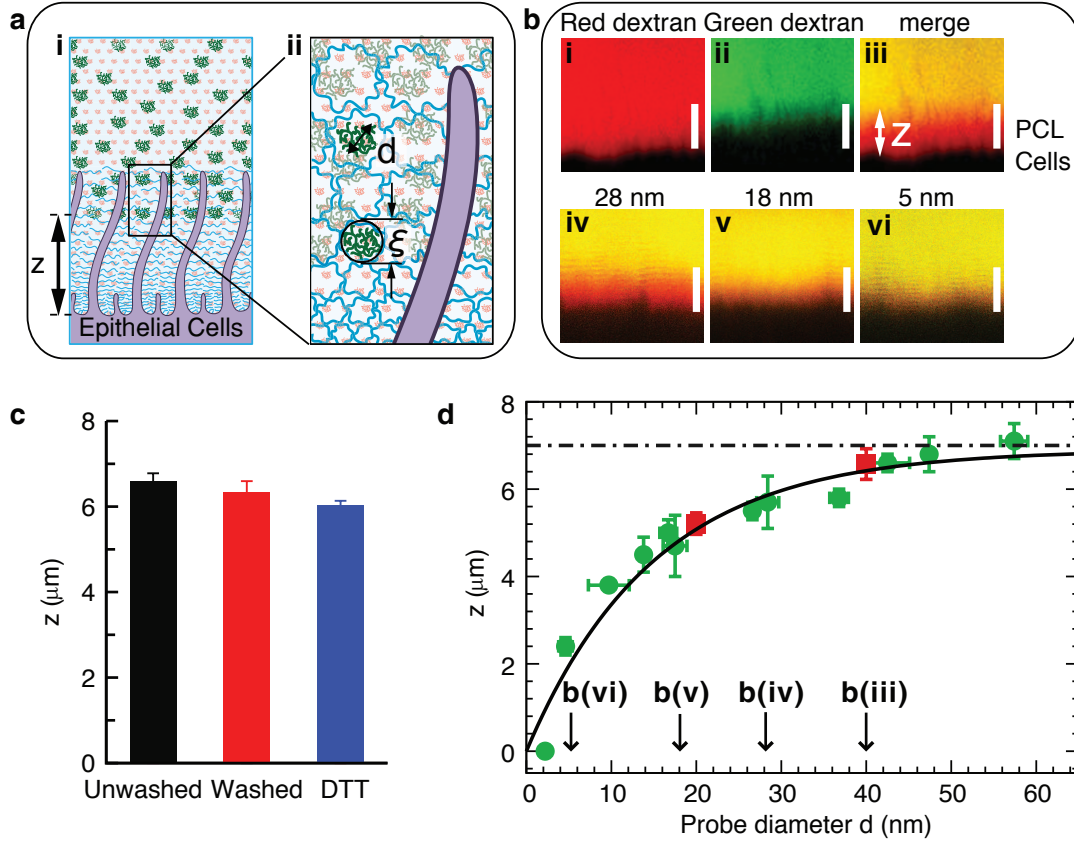
Figure 3.3: Size exclusion gradient in the PCL. a, (i), Schematic illustration of the two-dye technique used to probe the mesh size distribution within the PCL. Insert (ii), Probe molecules are expected to penetrate part of the PCL down to a distance z from the cell surface at which the PCL mesh size ξ is on the order of molecular diameter d. b, Representative XZ-confocal images of: (i), small ($d \approx 2$ nm) dextran fluorescently labeled with Texas Red exploring the whole PCL; (ii), green dextran with hydrodynamic diameter $d \approx 40$ nm, labeled by FITC; (iii), merged image showing the exclusion thickness z defined as the height of the red region bounded by the cell layer (black due to lack of staining) and the yellow (green + red) layer; (iv-vi), exclusion of dextran molecules with decreasing sizes. Scale bars = 7 μm. c, Exclusion for dilute solution of polystyrene beads with diameter $d = 40$ nm added to unwashed cultures, washed 3 times with PBS, washed (15 min) with 10 mM Dithiothreitol (DTT), to completely remove all mucus and adsorbed macromolecules from the cell surface[19]. d, Summary plot showing the dependence of exclusion thickness z on the size of dextran molecules (green circles). The exclusion of fluorescently labeled 20 and 40 nm polystyrene particles (red squares) are added for comparison. Solid curve is the best fit to the data by an empirical equation: $z(d) \approx 7\mu\text{m}[1 - \exp(d/15\text{nm})]$, and dash-dotted line at 7 μm represents the height of the outstretched cilia.

This technique is based on the partitioning concept: if probes of size d enter the PCL layer from dilute solutions [60], they are repelled by crowded tethered macromolecules within the PCL and have to pay a free energy penetration price, $F \approx k_B T (d/\xi)^\gamma$ (where

$\gamma = 2$ for polymers and $\gamma = 2$ for particles, k_B is Boltzmann constant and T is absolute temperature). Note that scaling prefactor on the order of unity have been omitted from this and following equations. The partition coefficient $P(d)$ of probes of size d, defined as the ratio of concentration of the probes in the PCL to their concentration in the dilute solution outside the PCL, is the Boltzmann weight corresponding to this free energy penalty:

$$P(d) = \exp\left(-F/k_B T\right) \approx \exp\left(-\left[d/\xi\left(z\right)\right]^{\gamma}\right) \tag{3.1}$$

Function $\xi\left(z\right)$ in this expression describes variations of mesh sizes in the PCL with distance z from the cell surface. Since an exponential is a rapidly varying function, this expression can be approximated by a step function [109], with a simple interpretation that probe molecules or particles penetrate the PCL from dilute solutions down to the depth $z\left(d\right)$ at which the probe size d is equal to the mesh size ξ (Figure 3.3a). Within this step function approximation, the depth profile of mesh sizes $z\left(\xi\right)$ is identical to the exclusion profile $z\left(d\right)$. More rigorous analysis accounting for both the exponential form of the partition coefficient and the polydispersity of probe molecules led only to a small correction in the depth profile of mesh sizes $z\left(d\right)$ (see 3.3).
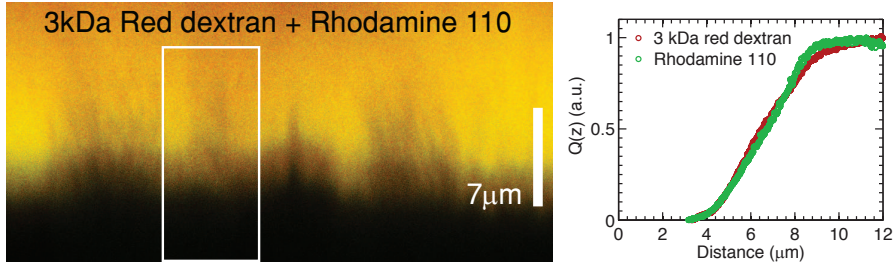
Figure 3.4: 3 kDa Texas Red dextran molecules penetrate into the PCL and reach the cell surface. Representative XZ-confocal images for HBE cells added with dilute mixture solution of unfractionated Texas Red dextran with average molecular weight 3 kDa and Rhodamine 110. Rhodamine 110 is a fluorescently green molecule of very small size (hydrodynamic diameter ~ 1.6 nm[110]). The overlap between the penetration for the 3 kDa red dextran and that for green Rhodamine 110 into the PCL, shown by the yellow zone, suggests that the 3 kDa red dextran can also reach the cell surface. This is further demonstrated by the overlap of the normalized intensity profiles for both the red dextran and green Rhodamine molecules.

The PCL exclusion profile $z\left(d\right)$ was measured by two-color fluorescent imaging of

two probes of well-defined sizes: 1) "large" green fluorescent dextran molecules of hydrodynamic diameter d and 2) "small" red fluorescent dextran molecules. A mixture of these red and green molecules was applied in dilute solutions to HBE cultures washed free of the overlying mucus layer (Figure 3.3b). The small ($d \approx 2$ nm) Texas red fluorescently labeled dextrans completely penetrated the PCL and reached the cell surface (Figure 3.3$b(i)$), as evidenced by the complete overlap of the fluorescence profile with that of a sub-nanometer dye, Rhodamine 110 (see Figure 3.4). In contrast, fractionated large green fluorescein isothiocyanate (FITC)-labeled dextran molecules with $d \approx 40$ nm, were excluded from the PCL (Figure 3.3$b(ii)$). The exclusion zone $z(d)$ (red region in Figure 3.3$b\,(iii)$), defined as the part of the PCL accessible to small dextrans but not to large ones, had a height $z \approx 6.5$ μm, close to the height of outstretched cilia. The yellow region above the exclusion zone represents the region accessible to both large (green) and small (red) dextrans. The 6.5 μm exclusion zone is in agreement with the results using the 40 nm fluorescent beads (Figure 3.1b-d). Importantly, this exclusion persisted after extensive washing of the cell surface in the absence or presence of a reducing agent (10 mM Dithiothreitol; DTT), sufficient to remove adsorbed macromolecules, including the gel-forming mucins [19] (Figure 3.33c). Thus, these findings confirmed the main hypothesis of our "Gel-on-Brush" model that the PCL is occupied by macromolecules that are strongly tethered to cell surface. Furthermore, these tethered macromolecules are at sufficiently high concentrations to produce a 'tight' mesh with a maximum size ξ of 40 nm, that prevents the 40 nm dextran and beads (Figure 3.1b; Figure 3.3$b(ii)$) from penetrating the PCL.

By systematically changing the size d of the green probes and measuring their depth of penetration into the PCL, variations of the exclusion thickness $z(d)$ for probes of varying size d were observed (see Figures 3.3$b\,(iv\text{-}vi)$ and 3.5). This variation is consistent with a PCL macromolecular mesh that becomes "tighter" towards the cell surface (Figure 3.3d). This PCL gradient mesh likely functions as a permeability barrier to prevent the cell surface from small infectious agents (e.g., Respiratory Syncytial Virus (RSV), with diameter $d \approx 120\text{-}300$ nm [111]; Influenza A, with $d \approx 80\text{-}120$ nm [111];

$\langle d \rangle_w$ (nm)	z_{PCL} (µm)
47.4±0.5	6.8±0.4
42.4±2.6	6.6±0.2
26.6±0.5	5.5±0.2
16.7±1.0	5.0±0.3
9.7±2.4	3.8±0.1
4.6±0.8	2.4±0.2
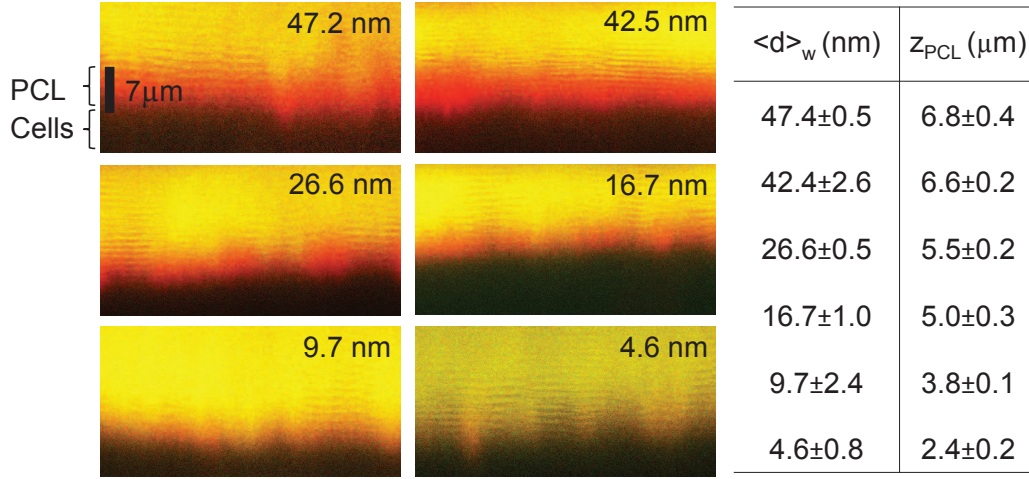
Figure 3.5: Representative confocal images showing the exclusion thickness z_{PCL} of probe molecules of different sizes in the PCL. The table shows the exact numbers of weight average hydrodynamic diameter $\langle d \rangle_w$ (see 3.3 and Table B.1 in Appendix B) and the corresponding exclusion thicknesses z_{PCL}.

Adeno-associated Virus (AAV), with $d \approx$ 20-30 nm [112]), and as an osmotically-active lubricating gel mucus.

3.3   Theoretical analysis of PCL permeability

The mesh size of PCL in living HBE cultures was determined from the measurements of the penetration depth into the PCL by fractionated fluorescently-labeled probe molecules (e.g. dextrans) of well-defined sizes following the addition of dilute solution of these probe molecules to the luminal side of HBE cultures. The results are reported as the dependence of penetration depth (distance from the epithelial cell surface) on the weight average hydrodynamic diameter of probe molecules. The penetration depth was measured as the average thickness of the red zone in the confocal images (see Figure 3.3*b*).

Note that each fraction of probe molecules obtained by size exclusion chromatography is not perfectly monodisperse. The reported size corresponds to the weight average hydrodynamic diameter of each fraction, which is shown in Tables B.1 and B.2 in Ap-

pendix B. To rationalize this protocol we compare the results obtained by using the weight average hydrodynamic diameter with the analysis that takes into account the actual distribution of dextran sizes (the "full profile analysis"). Below we demonstrate that the results obtained from these two methods are in reasonable agreement with each other within the error of our measurements.

3.3.1 Profile analysis
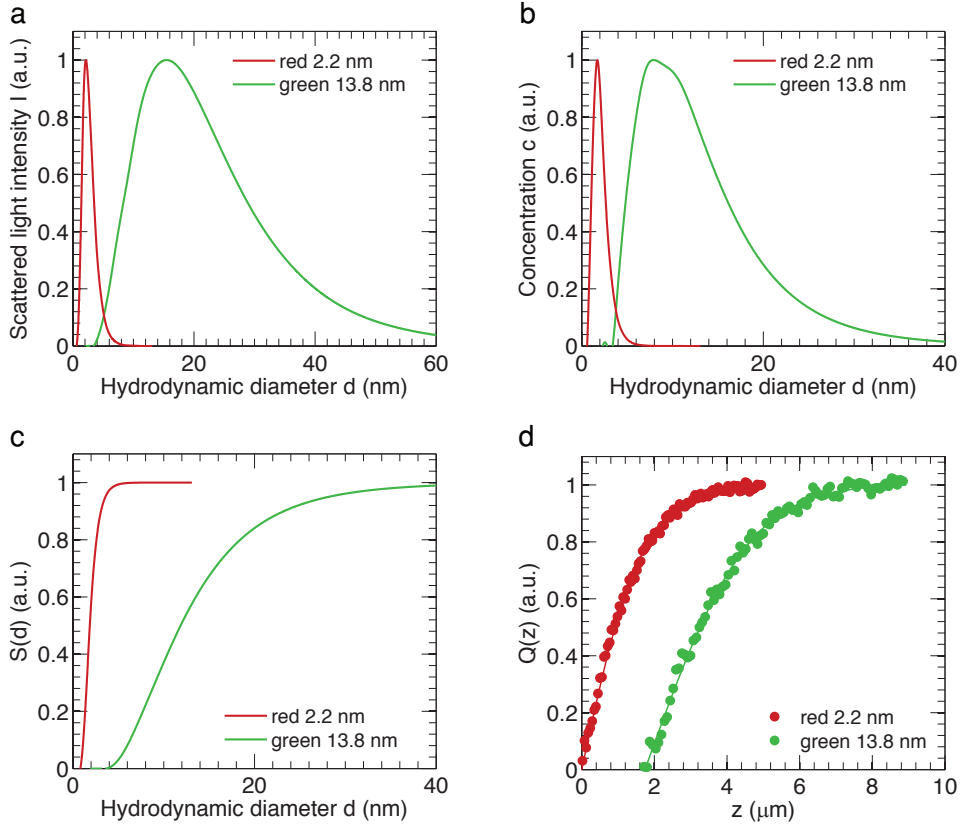
Figure 3.6: Protocol of "profile analysis" for penetration of molecules into PCL. a, Typical intensity-size distribution curves of red dextran molecules (3 kDa Texas Red dextran; weight average hydrodynamic diameter $\langle d \rangle_w = 2.2$ nm; red line) and a fraction of green dextran molecules (fraction 36 of 2 MDa stock dextran (see Appendix B; $\langle d \rangle_w = 13.8$ nm; green line). b, Normalized concentration-size distribution curves converted from the intensity-size distribution curves in (a) using relation eq. B.16 for 2.2 nm red dextran (red line) and 13.8 nm green dextran (green line). c, Predicted normalized concentration distribution $S(d)$ of red (red line) and green probe molecules (green line) smaller than d using "step function" approximation. d, Normalized measured fluorescent intensity (concentration) of red and green probe molecules within the PCL versus their distance z from the cell surface.

The basic assumption of "full profile analysis" is that probe molecules can freely penetrate into the PCL down to the distance z from epithelial cell surface, at which the mesh size $\xi(z)$ in the PCL is on the order of the diameter d of probe molecules. If we denote the exclusion thickness z for probe molecules with hydrodynamic diameter d, the shortest distance of these molecules from the cell surface, by z_d, then we conclude that the mesh size at this distance: $\xi(z_d) \approx d$. This assumption approximates distribution profile of probe molecules with size d in the PCL by a step function: molecules with size d are evenly distributed in the region with mesh size larger than d, corresponding to the distance from the cell surface further than z_d; whereas they are excluded from the region with the distance from the cell surface closer than z_d, where the mesh size ξ is smaller than d.

Each fraction of dextran molecules was characterized by dynamic light scattering (DLS) and a distribution of the scattered light intensity versus the logarithmic of hydrodynamic diameter ($\log d$) was obtained. Dividing the intensity value by the corresponding molecular size d one obtains the intensity distribution on linear molecular size scale[1]: $I(d)$ vs. d, shown in Figure 3.6a. Note that the scattered light intensity is proportional to the product of concentration c and mass M of polymers: $I \sim cM$. Therefore, one can convert the intensity-size distribution $I(d)$ to the concentration-size distribution $c(d)$ via

$$c(d) \sim I(d)/M \sim I(d)/d^{1/\nu} \tag{3.2}$$

because the mass M of polymers is proportional to the power of polymer size d: $M \sim d^{1/\nu}$ (see Appendix B), where ν is the Flory exponent in a good solvent. For flexible linear polymers $\nu \simeq 3/5$ [60] and for randomly branched polymers $\nu \simeq 1/2$ [113, 114]. Dextran is a linear molecule at low molecular weights and a branched molecule at high molecular weights. In our analysis $\nu \simeq 0.5$ was used for dextran fractions with

---

[1]Considering the invariance of the mass of molecules at different representations (linear-log and linear-linear coordinate systems), the scattered light intensity $I_{\log}$ for molecules with size in the interval $\Delta(\log d)$ within linear-log coordinates is the same as the intensity I_{linear} in the interval Δd within linear-linear coordinates. Therefore, the transformation from linear-logarithmic to linear-linear scale can be obtained by considering Jacobian transformation: $I_{\log}\Delta(\log d) = I_{\text{linear}}\Delta d$, which gives $I(d) \equiv I_{\text{linear}}(d) \propto I_{\log}/d$. For more in detail please refer to appendix B.

molecular weight higher than 10 kDa [115] and $\nu \simeq 3/5$ was used for 3 kDa Texas Red dextran.

A typical normalized concentration-size distribution $c(d)$ of a fraction of probe molecules is shown by the green solid line in Figure 3.6b. From this distribution one can 1) estimate the weight average hydrodynamic diameter as $\langle d \rangle_w \equiv \sum_i c_i d_i / \sum_i c_i$, in which c_i is the concentration for polymers with hydrodynamic diameter d_i; and 2) calculate the normalized concentration distribution $S(d)$ of molecules within this fraction that are smaller than d:

$$S(d) = \frac{\int_{d_{\min}}^{d} c(d)\,\mathrm{d}d}{\int_{d_{\min}}^{d_{\max}} c(d)\,\mathrm{d}d} \tag{3.3}$$

shown by the solid green line in Figure 3.6c. This normalized concentration $S(d)$ corresponds to the weight fraction of molecules that are able to penetrate mesh of size $\xi \simeq d$ and is therefore proportional to the fluorescent intensity of this fraction of probe molecules in the PCL.

We measured the fluorescent intensity (concentration) of probe molecules in the PCL as a function of distance from the cell surface. The normalized fluorescent intensity at distance z from the cell surface is denoted by $Q(z)$ and shown by the green plot in Figure 3.6d. The cell surface is determined by the lower bound of the penetration of small (weight average hydrodynamic diameter $\langle d \rangle_w \sim 2$ nm, see Appendix B) red dextran molecules (see extrapolation of the red curve to $Q(z=0) = 0$ in Figure 3.6d). As shown by Figure 3.4, 3 kDa Texas Red dextran molecules penetrate into the PCL down to the same distance as rhodamine-110, which has sub-nanometer size and thus able to reach the cell surface.

Our step function approximation implies that for the same values of the normalized distributions $S(d)$ and $Q(z)$, the hydrodynamic diameter d of probe molecules is related to the distance z from the cell surface at which the penetration of these molecules is stopped. This analysis allows one to obtain a profile $z(d)$ describing the dependence of exclusion thickness z on molecular size d for any solution of probe molecules with

known size distribution.
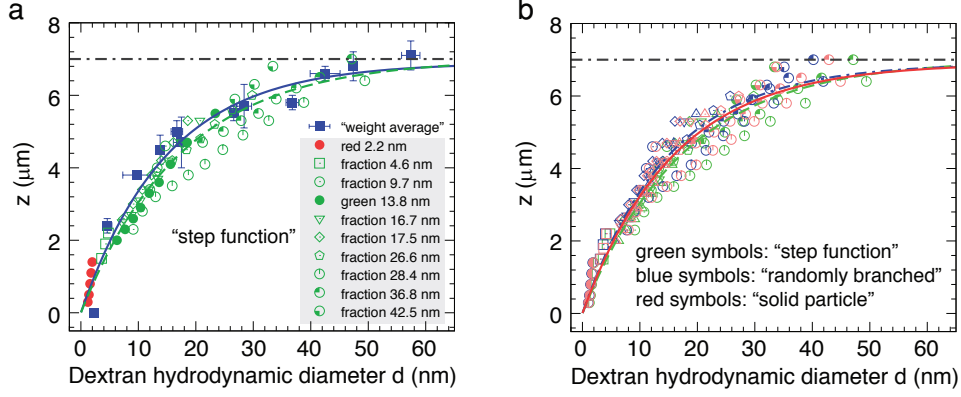
Figure 3.7: Results of PCL permeability obtained from "profile analysis". a, Dependence of distance z from the cell surface on the hydrodynamic diameter d of dextran molecules: blue solid squares—results obtained using the weight average hydrodynamic diameter of dextran fractions, solid line—best fit of these data $z(d) \approx 6.9\mu\text{m}[1 - \exp(-d/15.0\text{nm})]$; green symbols—results based on "full profile analysis" using "step function" approximation, dashed line—best fit of these data $z(d) \approx 7.0\mu\text{m}[1 - \exp(-d/17.5\text{nm})]$. Note that the red solid circles are results for 3 kDa Texas Red dextran. b, Comparison between the results from the "full profile analysis" using "step function" approximation (green symbols, green dashed line—best fit of these data $z(d) \approx 7.0\mu\text{m}[1 - \exp(-d/17.5\text{nm})]$), "randomly branched" approximation assuming that dextran is a randomly branched polymer with $\gamma = 2$ in eq. 3.5 (blue symbols, blue dash-dotted line—best fit of these data $z(d) \approx 6.9\mu\text{m}[1 - \exp(-d/15.0\text{nm})]$), and "solid particle" approximation assuming that dextran molecules are solid particles with $\gamma = 3$ in eq. 3.5 (red symbols, red solid line—best fit of these data $z(d) \approx 6.9\mu\text{m}[1 - \exp(-d/15.8\text{nm})]$). Black dash-dotted lines in (a) and (b) correspond to the 7 μm length of extended cilia.

The results on the exclusion profile $z(d)$ of probe molecules obtained by the above "step function profile analysis" of nine different fractions of green probe molecules are shown by green symbols in Figure 3.7a. These results can be described by a phenomenological equation

$$z(d) \approx z_0 \left[1 - \exp\left(-d/\bar{\xi}\right)\right], \quad \text{for } 0 < z < z_0 \tag{3.4}$$

in which $z_0 = 7.0 \pm 0.5$ μm is the maximum height of the PCL and the characteristic PCL mesh size is $\bar{\xi} = 17.5 \pm 2.4$ nm (see the dashed line in Figure 3.7a). This equation describes the penetration profile of probe molecules with different sizes into the PCL. The penetration profile obtained using the weight average molecular size as reported

27

value is shown by solid squares in Figure 3.7a and the best fit to this profile is presented by the solid line (eq. 3.4) with $z_0 = 6.9 \pm 0.8\ \mu$m and $\bar{\xi} = 15.0 \pm 3.7$ nm. These results indicate that the penetration profile obtained using the weight average molecular size is in agreement with that using "step function profile analysis" within the error of our measurements.

In the above we assumed that probe molecules of a particular size d in each fraction follow a "step function" distribution in the PCL. In fact probe molecules with size d can penetrate into the PCL to a distance z from the cell surface smaller than z_d, at which the mesh size $\xi\ (z < z_d)$ is smaller than diameter d, but they have to pay free energy penalty on the order of $k_B T\ (d/\xi\ (z))^\gamma$ [116]. Here the exponent γ depends on the type of the probes and solvent quality[2]. For a solid probe particle $\gamma = 3$, for a linear flexible polymer $\gamma = 5/3$ in a good solvent and $\gamma = 2$ in a theta solvent [60], and for a randomly branched polymer $\gamma = 2$ in a good solvent [113] and $\gamma = 16/7$ in a theta solvent [114]. Therefore, the distribution $P(z)$ of probe molecules with size d in the PCL at distance z smaller than z_d becomes [116]

$$P(z) = \text{const} \times \exp\left[-\left(d/\xi\left(z\right)\right)^\gamma\right], \quad \text{for } z < z_d \tag{3.5}$$

The results obtained from "profile analysis" by considering dextran as a randomly branched polymer in a good solvent ($\gamma = 2$) [115] are shown by the blue symbols in Figure 3.7b. The best fit of eq. 3.4 to these data is shown by the blue dash-dotted line with $z_0 = 6.9 \pm 0.4\ \mu$m and $\bar{\xi} = 15.0 \pm 2.0$ nm, which is in good agreement with the results of analysis using the "step function" approximation, shown by the green symbols and the green dashed line in Figure 3.7b. Furthermore, considering dextran as a solid particle ($\gamma = 3$) leads to almost identical results ($z_0 = 6.9 \pm 0.4\ \mu$m and

---

[2]The exponent γ in eq. 3.5 for different types of probes can be estimated by the following way. Consider a probe of size d penetrating into a semidilute polymer solution (brush) with mesh size (correlation length) ξ. The free energy penalty for the probe penetration is about $k_B T$ per correlation blob. The number of correlation blobs involved in the length scale d is proportional to the power of the ratio of the probe size to the correlation length: $n \simeq (d/\xi)^{d_f}$, in which d_f is the fractal dimension of the probe in dilute solutions. Therefore, the free energy penalty is about $k_B T\ (d/\xi)^{d_f}$, indicating that exponent γ is equivalent to the fractal dimension d_f. The dimensionality for a solid particle is 3; for a flexible linear polymer it is $5/3$ in a good solvent and 2 in a theta solvent [60]; for a randomly branched polymer it is 2 in a good solvent [113] and $16/7$ in a theta solvent [114].

$\bar{\xi} = 15.8 \pm 2.1$ nm; red symbols and red solid line in Figure 3.7b). The fitting parameters z_0 and $\bar{\xi}$ of eq. 3.4 to the results from different types of analysis are listed in Table 3.1. As clear from Table 3.1, all methods of profile analysis agree with each other within experimental error bars.

| | | Full profile analysis | | |
	Weight average	Step function	Randomly branched	Solid particle
z_0 (μm)	6.9 ± 0.8	7.0 ± 0.5	6.9 ± 0.4	6.9 ± 0.4
ξ (nm)	15.0 ± 3.7	17.5 ± 2.4	15.0 ± 2.0	15.8 ± 2.1

Table 3.1: List of fitting parameters z_0 and $\bar{\xi}$ of eq. 3.4 to results from different analysis.

3.3.2 Mesh size distribution in the PCL

As illustrated in Figure 3.8a, the PCL is modeled as an array of cylindrical brushes, in which each brush consists of a cylindrical core (cilium) and grafted polymers (tethered macromolecules), shown in Figure 3.8b. A single cilium brush in an unperturbed state is shown in Figure 3.8c, in which R_{cilium} is the radius of the cylinder (cilium) and the thickness L_0 is defined as the average distance from the center of the cylinder to the free ends of grafted macromolecules. The mesh size (correlation length) $\xi(r)$ in an unperturbed cylindrical brush at distance r from the center of the cylinder is related to the grafting density σ of the macromolecules to the surface of the cilia as [117]

$$\xi(r) \approx \sigma^{-1/2} \left(\frac{r}{R_{\text{cilium}}} \right)^{1/2}, \quad \text{for } r > R_{\text{cilium}} \tag{3.6}$$

which is shown by Figure 3.8c and the dashed line in Figure 3.8e. The volume fraction profile of tethered polymers is

$$\phi(r) \approx \left[\frac{\xi(r)}{b} \right]^{(1-3\nu)/\nu}, \quad \text{for } r > R_{\text{cilium}} \tag{3.7}$$

where ν is Flory exponent depending on solvent quality (for a theta solvent $\nu = 1/2$ and for a good/athermal solvent $\nu = 3/5$) [60] and b corresponds to the Kuhn length of polymers. Here $\nu = 3/5$ is used as the physiological solutions are good solvent for

macromolecules like mucins. The volume fraction profile (eq. 3.7) can be rewritten in terms of the distance r from the center of the cylinder

$$\phi(r) \approx (\sigma b R_{\text{cilium}})^{2/3} \left(\frac{r}{b}\right)^{-2/3}, \quad \text{for } r > R_{\text{cilium}}, \text{good/athermal solvent} \quad (3.8)$$

Lateral distribution of mesh sizes in the PCL is almost uniform
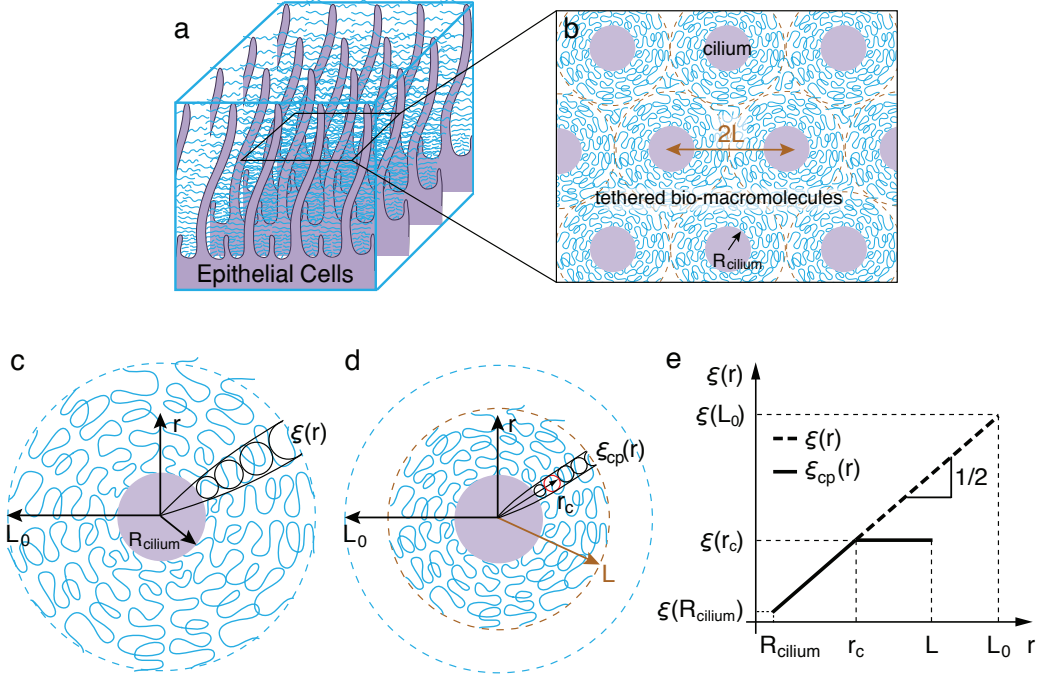
Figure 3.8: Cylindrical brush model of periciliary layer (PCL). a, PCL is modeled as an array of cylindrical brushes; b, Lateral cross-section view of the PCL as an array of cylindrical brushes, in which bio-macromolecules are tethered to the cylindrical cilia. The radius of a cilium is R_{cilium} and the distance between the centers of two neighboring cilia is $2L$. c, An unperturbed single cilium brush with thickness L_0 expected to be larger than L. d, The brush is compressed laterally from its unperturbed thickness L_0 to L due to the limited space between neighboring cilia. e, Mesh size profile for an unperturbed cilium brush (dashed line) and a laterally compressed cilium brush (solid line). Logarithmic scales.

The mesh size of a single cylindrical brush in its unperturbed state increases as a power law of distance r from the center of the cylinder (eq. 3.6 and dashed line in Figure 3.8e) due to the steric repulsion between grafted macromolecules. Such non-uniform lateral distribution of mesh sizes could lead to a non-uniform lateral distribution of probe molecules and hence their fluorescent intensity. It will be shown below that the

compression of cylindrical brushes (Figure 3.8c) due to the confinement by the neighboring cilia leads to an almost uniform lateral distribution of mesh sizes and therefore probe molecules.

The thickness of a cylindrical brush decreases under compression from its unperturbed thickness L_0 to a smaller value L, as shown in Figure 3.8c&d. The volume occupied by the grafted polymers is reduced and thus the lateral polymer concentration increases (mesh size decreases). The increase of the lateral polymer concentration, however, only occurs at distance r larger than certain crossover value r_c, shown in Figure 3.8d and solid line in Figure 3.8e. In the region with distance r smaller than r_c the concentration profile is almost unperturbed following the same power law as eq. 3.8. The lateral concentration (mesh size) profile at distance r larger than r_c is uniform with the value on the order of $\phi(r_c)$ (eq. 3.8) corresponding to the unperturbed concentration of polymers at distance r_c. The crossover distance r_c is determined by the thickness L of the cylindrical brush under compression

$$\int_{r_c}^{L_0} \phi(r) \, 2\pi r dr = \phi(r_c) \int_{r_c}^{L} 2\pi r dr \tag{3.9}$$

From the expression of $\phi(r)$ (eq. 3.8) one obtains the relation between the compressed brush thickness L and the crossover distance r_c

$$L^2 = \frac{1}{2} r_c^{2/3} \left(3L_0^{4/3} - r_c^{4/3} \right) \tag{3.10}$$

The compression ratio defined as the ratio between the volumes occupied by the tethered polymers after and before compression

$$\Lambda \equiv \frac{L^2 - R_{\text{cilium}}^2}{L_0^2 - R_{\text{cilium}}^2} \tag{3.11}$$

can be rewritten as

$$\begin{aligned}
\Lambda &= \frac{1}{1 - (R_{\text{cilium}}/L_0)^2} \left[\frac{3}{2} \left(\frac{r_c}{L_0} \right)^{2/3} \right. \\
&\quad \left. -\frac{1}{2} \left(\frac{r_c}{L_0} \right)^2 - \left(\frac{R_{\text{cilium}}}{L_0} \right)^2 \right]
\end{aligned} \tag{3.12}$$

The fraction of the volume occupied by the tethered polymers in which the mesh size has uniform lateral distribution is

$$\Gamma \equiv \frac{L^2 - r_c^2}{L^2 - R_{\text{cilium}}^2} \qquad (3.13)$$

Using eqs. 3.10, 3.12, and 3.13 one can estimate the lateral distribution of mesh sizes under compression. The radius of a cilium is $R_{\text{cilium}} \approx 50$ nm. The distance between centers of two neighboring cilia is about 300 nm, corresponding to the compression thickness $L \approx 150$ nm. The major component of tethered polymers is MUC4, with a contour length $l_{\text{contour}} \approx 1$ μm [118]. Therefore, the average end-to-end distance R of an isolated MUC4 is $R \approx b\,(l_{\text{contour}}/b)^{3/5} \approx 150$ nm, assuming that the Kuhn length of mucin molecules is $b \approx 10$ nm [61][3]. The polymers (e.g., MUC4) in a cylindrical brush are extended, implying that the unperturbed brush thickness L_0 defined as the sum of cilium radius and the size of a stretched polymer is larger than $R_{\text{cilium}} + R \approx 200$ nm. Even for $L_0 = 200$ nm the compression ratio defined in eq. 3.11 is $\Lambda = 0.53$, at which the crossover distance $r_c = 50$ nm is comparable to the cilium radius R_{cilium}. This indicates that almost 100% ($\Gamma \approx 1$) of the volume occupied by the grafted polymers has uniform lateral distribution of mesh sizes and therefore there is no lateral concentration profile in this compressed cylindrical brush. Larger values of $L_0 > 200$nm result in stronger compression and thus uniform lateral distribution of mesh sizes, leading to almost uniform lateral distribution of fluorescent intensity of probe molecules.

Gradient mesh size profile in the PCL

The data from PCL-permeability experiments (solid circles in Figure 3.7a) suggests that probe molecules penetrate into the PCL further as their size decreases. Assuming that probe molecules penetrate into the PCL down to distance z from the cell surface

---

[3]It was claimed that the Kuhn length of mucin molecules ranges from 10 to 15 nm. Consider the case for $b = 15$ nm the size R of an isolated MUC4 is $R \approx b\,(l_{\text{contour}}/b)^{3/5} \approx 180$nm.

at which the mesh size $\xi(z)$ is on the order of probe diameter d, such dependence of penetration depth on the size of probe molecules provides an indirect measurement of mesh size profile in the PCL: $\xi(z) \approx d(z)$. The determined penetration profile $d(z)$ for probe molecules of different sizes is shown by the solid line in Figure 3.7a (see eq. 3.4). The mesh size profile $\xi(z)$ in the PCL can be approximated by a logarithmic dependence on the distance z from the cell surface:

$$\xi(z) = d(z) \approx \bar{\xi} \log\left(\frac{z_0}{z_0 - z}\right), \quad \text{for } 0 < z < z_0 \tag{3.14}$$

in which the characteristic mesh size of the PCL $\bar{\xi} \approx 16$ nm. Such decay of the mesh size towards the cell surface indicates that the tethered macromolecules form a gradient protective layer that prevents external objects from reaching the cell surface. Similarly from the mesh size profile (eq. 3.14) one can estimate the concentration profile of the grafted macromolecules in the PCL.

$$\phi(z) \approx b^{(3\nu-1)/v} \xi(z)^{(1-3\nu)/v} \approx \left(\frac{b}{\bar{\xi}}\right)^{4/3} \left[\log\left(\frac{z_0}{z_0 - z}\right)\right]^{-4/3}, \quad \text{for } z_{\min} < z < z_0 \tag{3.15}$$

where $z_{\min}$ is the minimum distance from the cell surface at which the mesh size $\xi(z_{\min})$ of the PCL is comparable to the Kuhn length b of mucins. Considering $b \simeq 10$ nm the value of $z_{\min}$ is about 3 μm. The above expression (eq. 3.15) for the concentration of the grafted macromolecules is not valid because it predicts that in the region of the PCL with distance from the cell surface smaller than $z_{\min}$ the mesh size is smaller than the Kuhn length of mucin molecules. In order to estimate the concentration profile one has to consider the detailed shape of a mucin Kuhn segment, which has length of ~ 10 nm and diameter on the order of 5 nm due to the carbohydrate side chains (see chapter 2).

3.4 Summary: brush-like PCL serves as a gradient protective barrier

In this chapter we have demonstrated the existence of bio-macromolecules within the PCL. The bio-macromolecules are physically localized within the PCL by attaching to cilia as well as the epithelial surface. It is expected that such tethered macromolecules form a brush-like structure. Several key features of the brush-like PCL have been identified by using the combination of experimental and theoretical approaches. Here we would like to emphasize:

(i) The mesh size of the PCL is 10–20 nm.

(ii) The mesh size of the PCL decreases towards to the epithelial cell surface, suggesting that the grafting density of the tethered bio-macromolecules increases towards the cell surface.

(iii) In addition to the mucus barrier, the brush-like PCL can serve as a gradient protective layer in preventing external objects that can sneak through the mucus "filter" attempting to approach the epithelial surface.

CHAPTER 4

OSMOTIC INTERACTION BETWEEN MUCUS LAYER AND PERICILIARY LAYER

The "Gel-on-Brush" model predicts that the densely tethered macromolecules within the PCL generate biophysical forces that regulate hydration of both the PCL and the overlying mucus layer. Flexible mutually interpenetrating polymers, such as the tethered mucins, in the PCL repel each other and thus generate osmotic pressures within the PCL. The rate of osmotic pressure change with polymer concentration (c) defines the osmotic modulus K,

$$K = c\frac{\partial \pi}{\partial c} \tag{4.1}$$

a parameter that quantifies the hydration (water-drawing) power of the system. The higher the osmotic modulus, the higher the hydration (water-drawing) power. It is expected that the PCL is hydrated, and therefore, maintaining effective mucus clearance, as long as its osmotic modulus is larger than that of mucus/mucus simulants. To test this hypothesis we first quantified the osmotic modulus of mucus/mucus simulants (see 4.1) and then applied mucus/mucus simulants to challenge the PCL (see 4.2).

4.1 Osmotic modulus of mucus and mucus simulants

4.1.1 Experiments

Endogenous (native) mucus accumulation

Endogenous (native) mucus refers to the mucus accumulated on well differentiated HBE cell cultures without any perturbation other than adding physiological buffer

(PBS). HBE cells from donated lungs are harvested by enzymatic digestion as previously described [119]. Disaggregated human bronchial epithelial (HBE) cells are seeded on $12\,\mathrm{mm}$ diameter Transwell Clear supports (Corning Costar, Cambridge, MA) at a density of 2.5×10^5 cells/cm^2 in a well-defined airway cell media [119]. Cultures are maintained at an air-liquid interface until fully differentiated (~ 4 weeks). Mucus accumulated on the full differentiated cell cultures was washed away using PBS. These thoroughly washed well differentiated HBE cell cultures were placed back for incubation to allow mucus to accumulate.
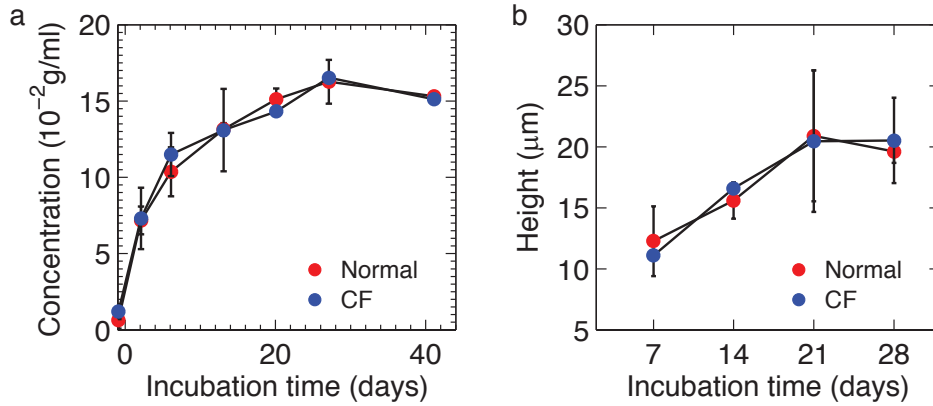
Figure 4.1: Dependence of mucus concentration (a) and height (volume) (b) on incubation time.

We first characterized the dependence of mucus concentration as well as the mucus thickness (volume) on the incubation time. The mucus concentration (see 4.1.1) was found to increase rapidly from almost 0 to ~ 0.06 g/ml (7% solids) within the first week and then approach a steady value ($\sim 14\%$ solids) after 3–4 weeks. Note that the concentration of mucus has almost the same dependence on incubation time for both normal and CF cases. A possible reason could be that the concentration of mucus on cell cultures is controlled by water evaporation. The kinetics of water evaporation is determined by the humidity of incubator (typically 95%), surface area of cell cultures in contact with air, and the amount of solutes (solid content) in the mucus. The mucin secretion rate is determined by the number of mucin-secreting cells, which are expected to be the same for both normal and CF cell cultures as long as the cultures are not

subjected external actuation such as inflammation and bacterial infection [120, 121]. This condition is fulfilled for cell cultures grown in sterilized incubator, and therefore, the amount of solutes (solid content) in the mucus is expected to be the same for both normal and CF cells.
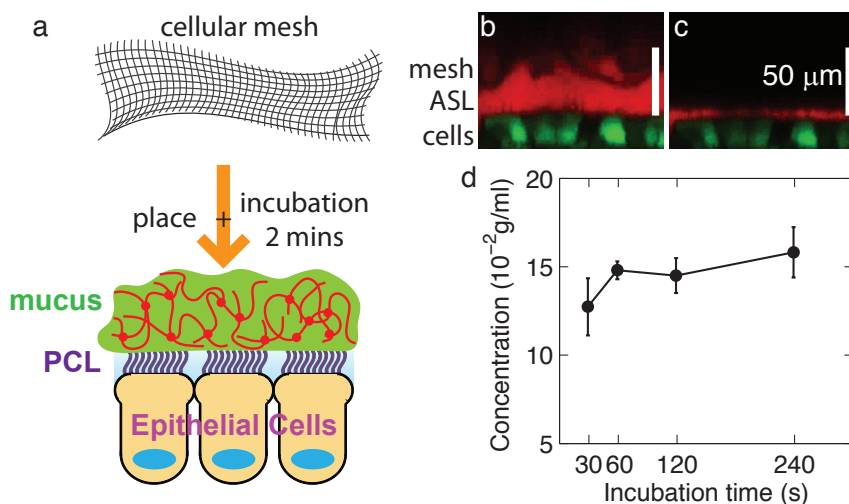
Figure 4.2: Mesh technique for measuring concentration of native mucus. a, Schematic illustration for the mesh technique. b, c, Representative XZ confocal images showing (b) the placement of the mesh within the mucus layer (labeled with 3 kDa Texas Red dextran) and (c) the complete removal of the overlying mucus layer from the PCL. d, Concentration of native mucus measured by the mesh technique as a function of incubation time after placing mesh.

Measurements of native mucus concentration

The challenge for measuring the concentration of native mucus is that it is difficult to grab the on-cell mucus layer as its amount is very small, typically with thickness of tens of micrometers (volume ~ 10 μl). To overcome this difficulty we developed a "mesh technique" to measure the concentration of native mucus (see Figure 4.2). In this technique a flexible cellular mesh was placed on top of mucus accumulated on parallel cultures, incubated for about 2 minutes and then peeled off (Figure 4.2a). It was shown that the cellular mesh can bind to the mucus strongly enough to allow peeling almost all the mucus off (see Figure 4.2b, c). Furthermore, 2 minutes was found to be the

appropriate time that allows the mesh to tightly bind to the mucus (see Figure 4.2d). Dry-to-wet ratio experiments [23] were performed to measure the wet and dry weights of the peeled-off mesh with mucus. The obtained concentration defined as the ratio of total mass of solids in mucus to the mass of mucus, including the salt contribution ($\sim 1\%$), is conventionally called %solids. By subtracting salt concentration 0.9% from this value one can convert %solids to the concentration in terms of g/ml, corresponding to the mass of solids excluding salts per unit volume of mucus, as the density of mucus is ~ 1 g/ml. For instance, 2% solids is equivalent to 0.01 g/ml.

Native mucus with various concentrations was obtained either by selecting different incubation periods or by diluting (adding different amount of phosphate buffered saline (PBS) to the mucus with high concentration).

Osmotic pressure measurement

In these studies, we employed a custom-designed direct-membrane osmometer [122] equipped with a salt and small protein permeable osmotic membrane to measure the osmotic pressure of various mucus simulants (dextran and agarose) as well as of endogenous mucus. As shown in Figure 4.3, this device consists of a fluid chamber connected to a sensitive pressure transducer (Omega Engineering, Stamford, CT) affixed to the bottom of the chamber. A 25 mm diameter polyethersulfone membrane (Millipore Inc., Bedford, MA) separated the test chamber from the reference chamber filled with phosphate buffered saline (PBS). The osmometer was calibrated with commercial osmotic pressure standards (Wescor Inc., Logan, UT).

An osmotic membrane with 10 kDa molecular weight cutoff (MWCO), which has pore diameter about 2.8 nm extrapolated from the data in ref. [123], was used for measuring the osmotic pressure of mucus simulants. In each measurement, 0.2 ml of the mucus simulant was placed into the fluid chamber, allowing it to come into contact with the pressure transducer. The steady-state osmotic pressure of a mucus simulant
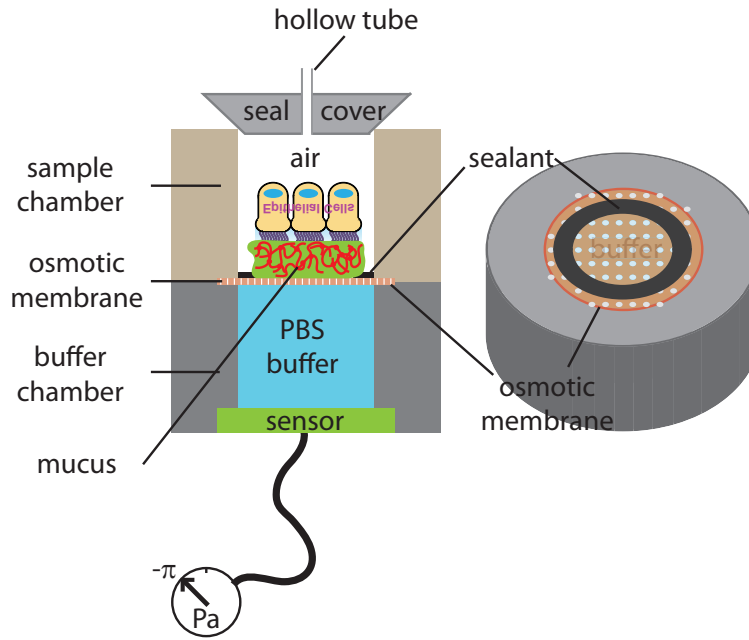
Figure 4.3: Customized osmometer for measuring osmotic pressure of mucus simulants and native mucus. Left: Schematic illustration of the osmometer. The osmometer has the buffer chamber (filled with PBS) and the sample chamber separated by an osmotic membrane with known molecular weight cut off (MWCO). The buffer chamber is connected to an osmotic sensor. The seal cover with a hollow tube is used to reduce the evaporation of the sample while keeping the sample chamber in contact with air. Right: 3D illustration showing that the edge of osmotic membrane is covered by a vacuum sealant to reduce the effective area of osmotic membrane to make sure it is fully covered by the native mucus.

with a given concentration was recorded.

The above system was modified to measure the osmotic pressure of endogenous mucus accumulated on the surface of HBE cultures, using the approach for measuring oncotic pressures of excised tissue samples [124]. Here, mucus was allowed to accumulate on the surface of the HBE epithelium for up to 4 weeks. The culture-insert membrane (Transwell-Clear; Corning Costar, Cambridge, MA) was carefully excised with a scalpel and placed directly onto a 100 kDa MWCO (pore diameter ~ 11 nm measured by solute transport methods [123]) osmotic membrane (see Figure 4.3). To investigate the change in the osmotic pressure with mucus concentration, parallel cultures were exposed to various amounts of exogenous fluid ($5 - 40$ μl of PBS) approximately 1 hour before the osmotic pressure measurements.

In all experiments, the osmotic moduli of mucus simulants (dextran and agarose) and endogenous mucus were calculated from the concentration dependence of osmotic pressure using equations presented in section 4.1.2.

4.1.2 Results and discussion: osmotic pressure and modulus of mucus and mucus simulants

The osmotic modulus K of a solution defined as $K = c\,(\partial \pi / \partial c)$ (eq. 4.1) describes the rate at which its osmotic pressure π changes with concentration c. Typically osmotic pressure of polymer solutions in a good solvent [60] can be described by the crossover phenomenological equation [60]

$$\pi = \frac{N_{Av}k_B T}{M_n} c \left(1 + (c/c^*)^{\alpha-1}\right) \tag{4.2}$$

where N_{Av} is the Avogadro number, k_B is the Boltzmann constant, T is the absolute temperature, M_n corresponds to the number average molar mass of polymer, and c^* is the polymer overlap concentration. Therefore, the osmotic modulus K defined by eq. 4.1 is

$$K = \frac{N_{Av}k_B T}{M_n} c \left(1 + \alpha\,(c/c^*)^{\alpha-1}\right) \tag{4.3}$$

Dextran

We have measured the osmotic pressure π of dextran solutions at concentrations ranging from dilute to semidilute regime, in which dextran molecules are overlapping with each other [60]. The dependence of dextran osmotic pressure on solution concentration was fitted by eq. 4.2 (see thin solid red line in Figure 4.4):

$$\pi_{dex} = 1.2 \times 10^4 \frac{\mathrm{Pa}}{\mathrm{g/ml}} c \left(1 + \left(\frac{c}{0.025 \mathrm{g/ml}}\right)^{1.25}\right) \tag{4.4}$$
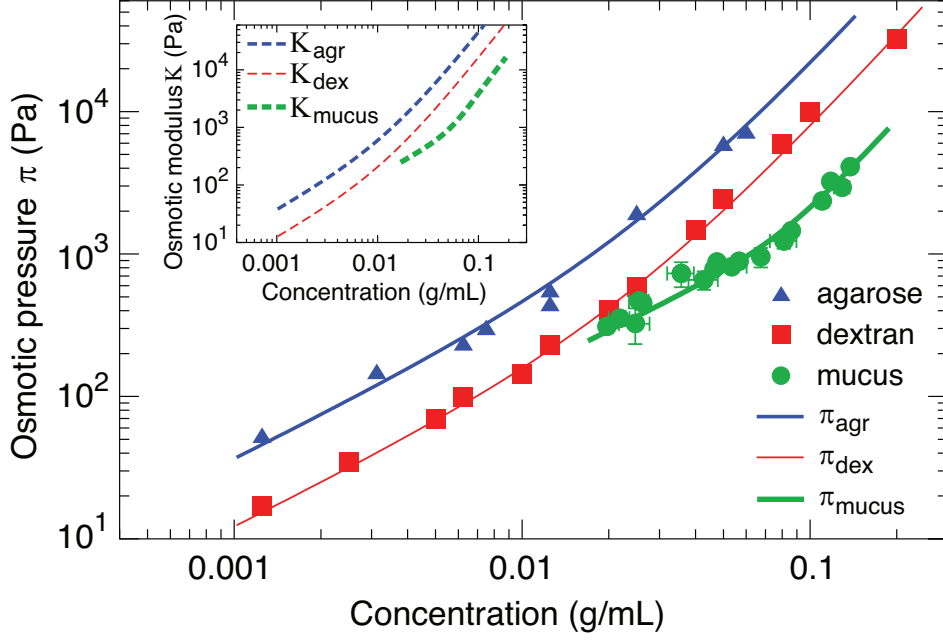
Figure 4.4: Osmotic pressure and modulus of mucus simulants and native mucus. Red squares: osmotic pressure of dextran solutions in PBS at room temperature; thin solid red line corresponds to dependence of osmotic pressure on solution concentration predicted by eq. 4.4. Blue triangles: osmotic pressure of agarose solutions in PBS; medium solid blue line is the best fit of the concentration dependence of agarose solution osmotic pressure (eq. 4.8). Green circles: osmotic pressure of native mucus; thick solid green line—best fit of mucus osmotic pressure (eq. 4.10). Insert: thin dashed red line—calculated osmotic modulus of dextran solutions (eq. 4.7); medium dashed blue line—calculated osmotic modulus of agarose solution (eq. 4.9); thick dashed green line—calculated mucus osmotic modulus (eq. 4.11). Note that the concentrations of mucus are all within the physiological range.

The value of exponent $\alpha = 2.25$ is in perfect agreement with previous study [114]. Equation 4.4 corresponds to the number average molar mass of dextran $M_n = 2 \times 10^5$ g/mole and the overlap concentration $c^* = 0.025$ g/ml. The average molecular size $\langle R_g^3 \rangle_n^{1/3}$ of polymers can be estimated from the number average molar mass and overlap concentration

$$c^* = \frac{M}{N_{Av}V} \simeq \frac{\sum_i n_i M_i}{N_{Av} \sum_i n_i (R_g)_i^3} = \frac{M_n}{N_{Av} \langle R_g^3 \rangle_n} \qquad (4.5)$$

where M is the total molar mass of polymers in pervaded volume V, n_i is the number fraction of polymers with molar mass M_i, and $(R_g)_i$ is the corresponding radius of gyration. Therefore, the average molecular size of dextran molecules is

$$\langle R_g^3 \rangle_n^{1/3} \simeq \frac{M_n}{c^* N_{Av}} \simeq 24 \text{ nm} \qquad (4.6)$$

This average size of dextran molecules is consistent with the average molecular size obtained from both size exclusion chromatography and dynamic light scattering characterizations (see appendix B). From eq. 4.4 one can obtain the osmotic modulus K (eqs. 4.1 and 4.3) of dextran solutions (see thin dashed red line in the insert of Figure 4.4):

$$K_{dex} = 1.2 \times 10^4 \frac{\text{Pa}}{\text{g/ml}} c \left(1 + 2.25 \left(\frac{c}{0.025 \text{g/ml}} \right)^{1.25} \right) \tag{4.7}$$

This equation was used to estimate the osmotic modulus of dextran solutions in the PCL compression and collapse experiments.

Agarose

The concentration dependence of osmotic pressure of agarose in PBS solution was measured at $37\ °\text{C}$ to keep low-melting point agarose from gelling (blue triangles in Figure 4.4). Fitting these data to eq. 4.2 we obtained the expression for concentration dependence of the agarose osmotic pressure (see the medium solid blue line in Figure 4.4)

$$\pi_{agr} = 3.6 \times 10^4 \frac{\text{Pa}}{\text{g/ml}} c \left(1 + \left(\frac{c}{0.027 \text{g/ml}} \right)^{1.25} \right) \tag{4.8}$$

The linear (van't Hoff) term of agarose osmotic pressure is consistent with the number average molar mass of 7×10^4 g/mole and the overlap concentration leads to molecular size $\langle R_g^3 \rangle_n^{1/3} \simeq 16$ nm. This value is consistent with the average molecular size obtained from dynamic light scattering characterization (see appendix B). The osmotic modulus of agarose solution is calculated using eqs. 4.1 and 4.8

$$K_{agr} = 3.6 \times 10^4 \frac{\text{Pa}}{\text{g/ml}} \times c \left(1 + 2.25 \left(\frac{c}{0.027 \text{g/ml}} \right)^{1.25} \right) \tag{4.9}$$

and plotted by the medium dashed blue line in the insert of Figure 4.4. Equation 4.9 was used to estimate the osmotic modulus of agarose solution.

Native mucus

The osmotic modulus of mucus was determined from the concentration dependence of mucus osmotic pressure. We observed two regimes of the concentration dependence of mucus osmotic pressure. Within the low concentration regime (from ~ 0.02 g/ml to ~ 0.06 g/ml), the osmotic pressure of mucus has a linear dependence on concentration $\pi \sim c$. In the high concentration regime (from ~ 0.08 g/ml to ~ 0.14 g/ml), the osmotic pressure increases as a higher power of concentration $\pi \sim c^{\beta}$, where $\beta = 2.21 \pm 0.17$. Since there is a sharp crossover between these two dependencies, we used a modified crossover expression

$$\pi_{muc} = kc \left[1 + \left(\frac{c}{c^*} \right)^{(\beta-1)m} \right]^{1/m} \tag{4.10}$$

to fit the data over the whole concentration range, with crossover exponent $m = 3$, coefficient $k = (1.45 \pm 0.29) \times 10^4 \ \text{Pa}/(\text{g/ml})$ and crossover concentration $c^* = 0.081 \pm 0.019$ g/ml. The fit of the mucus osmotic pressure to eq. 4.10 is shown in Figure 4.4 (thick solid green line). Note that the crossover concentration $c^* = 0.081 \pm 0.019$ g/ml is much larger than the overlap concentration of mucins, which is on the order of 10^{-3} g/ml taking into account that the size of gel-forming mucins is about 200 nm and their molecular weight is about 50 MDa (see chapter 2). This linear-concentration-dependence of native mucus osmotic pressure above overlap concentration might be due to the interactions between mucins and other protein molecules in mucus.

Osmotic modulus (defined by eq. 4.1) of native mucus is calculated using eq. 4.10

$$\begin{aligned} K_{muc} &= 1.45 \times 10^4 \frac{\text{Pa}}{\text{g/ml}} \times c \left[1 + \left(\frac{c}{0.081\text{g/ml}} \right)^{3.63} \right]^{1/3} \\ &\times \left[1 + \frac{1.21 \times \left(\frac{c}{0.081\text{g/ml}} \right)^{3.63}}{1 + \left(\frac{c}{0.081\text{g/ml}} \right)^{3.63}} \right] \end{aligned} \tag{4.11}$$

and is depicted by the thick dashed green line in the insert in Figure 4.4. This expression of the osmotic modulus of mucus was used to construct the plot of the dependence of PCL and cilia heights on mucus osmotic modulus.

4.2 Height of PCL/cilia under osmotic compression

We measured the osmotic pressure and calculated the osmotic modulus of the mucus layer on HBE cultures with concentrations spanning normal to "abnormally" high values (see Figure 4.4). The osmotic modulus (K) of the mucus layer strongly increased with mucus concentration, from 200 Pa at normal mucus concentrations [23] (roughly 0.01 g/ml, which is equivalent to 2% solids) to $3,000$–$8,000$ Pa for severely dehydrated (concentrated) mucus in ranges reported in CF patients (> 0.07 g/ml i.e. $> 8\%$ solids [23, 125]).

4.2.1 Height of periciliary layer

We measured the PCL osmotic modulus by exposing washed HBE cultures to solutions containing very large ($d > 50$ nm) PCL-impenetrable polymers of varying concentrations and, hence, osmotic moduli (Figure 4.5). Similar to the PCL penetration experiments (Figure 3.3), measurements of PCL osmotic moduli were performed utilizing a two-fluorescent-probe technique. However, unlike the PCL penetration experiments, only the concentration of the large green dextrans, and hence the osmotic modulus of the test solution, was varied.

Solutions containing large dextrans with osmotic moduli smaller/comparable to the modulus of normal mucus ($K \approx 200$ Pa) did not affect the height of the PCL (Figure 4.5$a(i, ii), b$). Only when K of the dextran solution exceeded 300 Pa, did the PCL begin to compress, as evidenced by the decrease in the exclusion height. Therefore, 300 Pa represents the osmotic modulus of a fully-hydrated (healthy) PCL (K_0) (Figure 4.5b, grey zone). Exposure to a higher concentration of dextran with a $K \approx 4,000$ Pa resulted in a significant collapse of the PCL (Figure 4.5$a(iii), b$).

Note, the probe penetration experiments described above (Figure 3.3) identified a gradient of mesh sizes in the PCL, strongly suggesting that the grafting density of
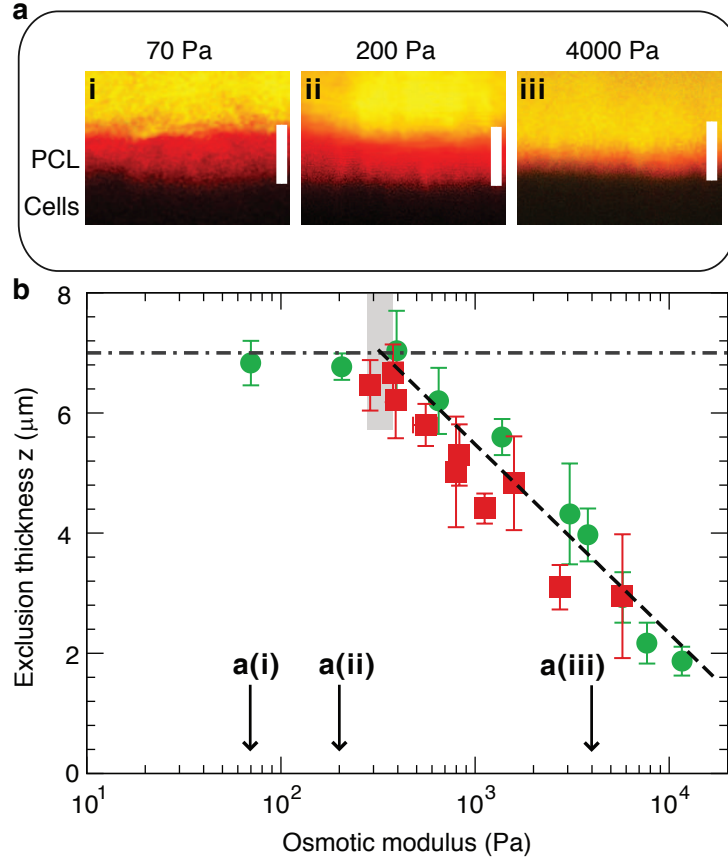
Figure 4.5: Osmotic compression of the PCL-brush by mucus and mucus simulants. a, Representative XZ-confocal images showing progressive compression of the PCL brush by large dextran molecules ($d > 50$ nm) of increasing osmotic moduli ((i) $\sim$ 70 Pa, (ii) $\sim$ 200 Pa, (iii) $\sim$ 4,000 Pa). Scale bars = 7 μm. b, Summary data of the exclusion thickness (z) of the large dextran molecules and endogenous mucus versus their osmotic moduli. Dashed black line represents the best linear fit to the dependence of PCL height on the logarithm of osmotic modulus of mucus/mucus simulants for $z < 6$ μm: $z \approx 7\mu m - 3.15\mu m \log(K/340\text{Pa})$. The highlighted region represents the osmotic modulus of a fully-hydrated (healthy) PCL, $K_0 \approx 300 \pm 60$ Pa, above which noticeable decrease of the PCL height was observed.

macromolecules tethered to cilia increases towards the cell surface. Based on this observation, we predicted that the repulsion between these macromolecules, and therefore, the osmotic modulus of the PCL would also increase towards the cell surface. Indeed, the exclusion zone for the probes was observed to decrease systematically as a function of the osmotic modulus K of the mucus simulants (green circles, Figure 4.5b). These findings were validated by the experiments in which the PCL was compressed by endogenous mucus at various concentrations (and osmotic moduli) (red squares in
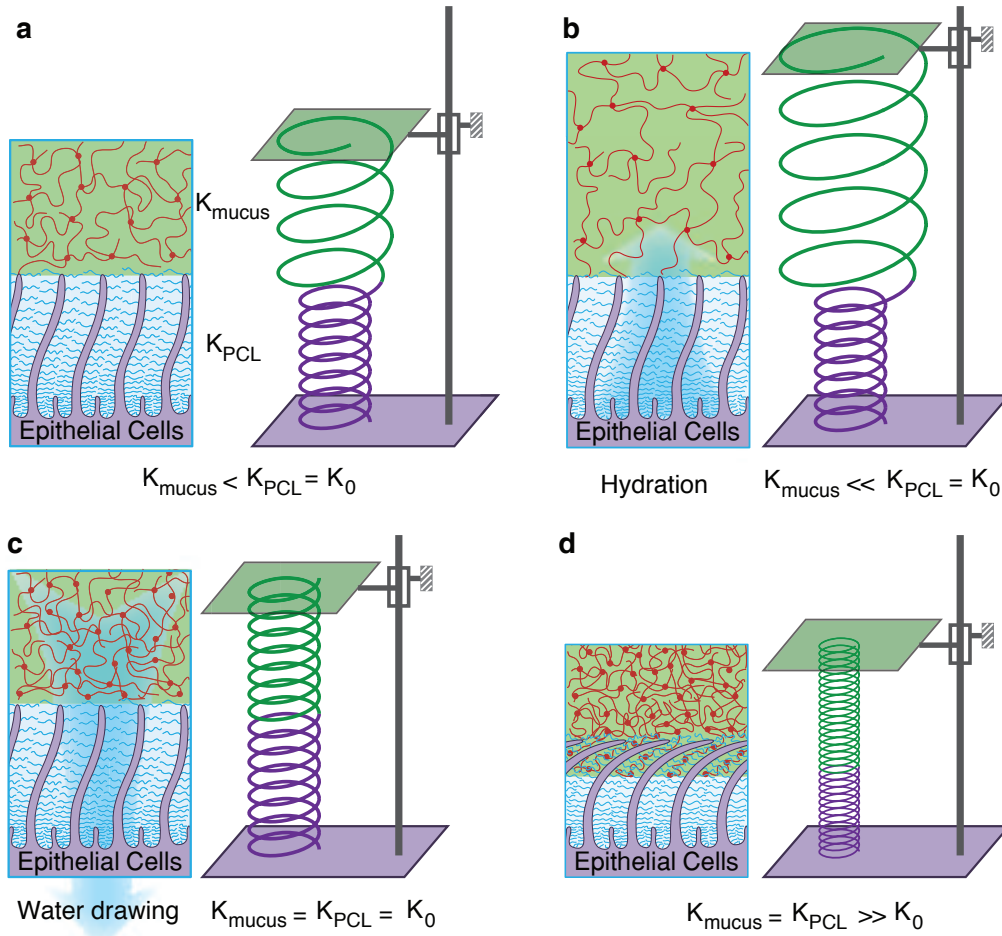
Figure 4.6: Schematic illustration showing the effects of the relative water-drawing powers of the mucus gel and the PCL. a, Normal state: the osmotic modulus of normal mucus (K_{mucus}) is smaller than that of the PCL ($K_{PCL} = K_0$). The two moduli are depicted by the diameters of the springs (K_{PCL} – purple and K_{mucus} – green) and the volume of water in the system is depicted by the fixed distance between two plates. b, water added to the healthy airway surface preferentially enters and thus dilutes the mucus layer, leaving the PCL unchanged. The resulting osmotic modulus of the mucus layer is much smaller than that of the PCL. b, Increased hydration: water added to the healthy airway surface (distance between plates increased) with $K_{mucus} < K_0$ preferentially enters and thus dilutes the mucus layer, leaving the PCL unchanged. The resulting osmotic modulus of the mucus layer is much smaller than that of the PCL ($K_{mucus} << K_0$). This state is depicted by larger length and diameter of the green spring with no change in the purple spring. c, d, Dehydrated state (plates close to each other): as water is removed it first preferentially leaves the mucus gel due to its lower osmotic modulus (c). Further dehydration leads to removal of water from both the mucus gel and the PCL. The moduli of both layers are increased and equal, represented by smaller diameters of shortened springs (d). This state corresponds to diseased airways (COPD, CF).

Figure 4.5*b*). Note that mucus with high concentrations, mimicking those found in immobile airway secretions from diseased lungs such as CF (i.e., > 0.07 g/ml [23, 125] with $> 3,000$ Pa), removed sufficient water from the PCL to cause its collapse (Figure 4.5*a*(*iii*), *b*).

These data suggest that the "Gel-on-Brush" model accurately describes the forces that govern hydration of airway surfaces. The model predicts that water distributes between the two airway surface layers, i.e., the mucus layer and PCL, according to their relative osmotic moduli (Figure 4.6). The layer with a lower osmotic modulus changes its concentration more readily than the layer with the higher osmotic modulus. This relationship is analogous to the deformation of a pair of springs connected in series (Figure 4.6*a*). Upon deformation of the pair, the softer spring (with lower modulus) deforms more than the stiffer one. Because the PCL is a "constrained" (tethered) system, its concentration saturates upon hydration and, therefore, it has a "minimal" osmotic modulus (K_0) when the PCL is fully hydrated. In contrast, since the mucus layer is under no such constraint, its osmotic modulus can become very small upon extensive hydration. As a result, liquid added to the hydrated/healthy airway surface preferentially enters the mucus layer, leaving the PCL unchanged (Figure 4.6*b*). Conversely, when the airway surface is dehydrated, liquid is drawn first from the mucus layer, increasing its concentration and, therefore, osmotic modulus. As the osmotic modulus of mucus layer exceeds K_0 of the PCL, water is extracted from both layers, increasing their concentrations and osmotic moduli resulting in compression of the PCL (Figure 4.6*c*, *d*). Thus, the "Gel-on-Brush" model posits that 1) for health, the osmotic modulus (of the PCL must be larger than that of the mucus layer (Figure 4.6*a*) to ensure the required hydration and lubricating properties of the PCL, for normal mucus layer transport; and 2) in disease, strong dehydration of the airway surface produces a mucus layer osmotic modulus (K_{mucus}) that significantly exceeds modulus of the healthy PCL, collapsing the PCL and slowing/abolishing mucus transport (Figure 4.6*d*).

4.2.2 Height of cilia

There are contrasting scenarios for PCL collapse upon osmotic compression that have important implications for cilia beating dynamics and mechanisms of mucus adhesion to the airway surface. For example, one possibility is that the tethered mucin brush is compressed against "extended" cilia upon exposure to dehydrated mucus or mucus simulants with high osmotic moduli, allowing penetration of mucus into the interciliary spaces (Figure 4.7a). This scenario is expected if cilia are elastically stiffer than the surrounding brush of tethered macromolecules and dehydrated mucus. An alternative possibility is that the cilia are compressed towards the epithelial surface (Figure 4.7b).

To distinguish between these two possibilities, bright-field microscopy of HBE cultures mounted in profile was utilized to directly measure the maximal height of the cilia during the exposure to solutions of varying osmotic moduli. Large dextran ($d > 50$ nm) or agarose ($d \approx 44$ nm) solutions with osmotic moduli < 800 Pa had negligible effects on the height of the cilia (Figure 4.7c and points to the left of the highlighted zone in Figure 4.7e). However, cilia height decreased significantly with increasing solution osmotic moduli (Figure 4.7d and points to the right of the highlighted zone in Figure 4.7e). The value of 800 Pa represents the minimum osmotic modulus required to deform the cilia (K_{cc}). With exposure to solutions with $K > K_{cc}$, the cilia still beat within this restricted space, but not at their full heights. These data, coupled with dye measurements of K_0 (see Figure 4.5), suggest that with moderate increases in osmotic modulus of the overlaying polymer layer, e.g., between $K_0 = 300$ Pa and $K_{cc} = 800$ Pa, there was compression of the brush towards the cilia. Polymer solutions with higher osmotic moduli caused cilia to collapse. Experiments with HBE mucus (red squares, Figure 4.7e) revealed that mucus with osmotic modulus $K = 5,700$ Pa, similar to that observed in CF, also produced complete ciliary collapse. Based on these data, it is apparent that airway cilia do not exhibit sufficient stiffness to resist osmotic collapse during severe airway surface dehydration.

48
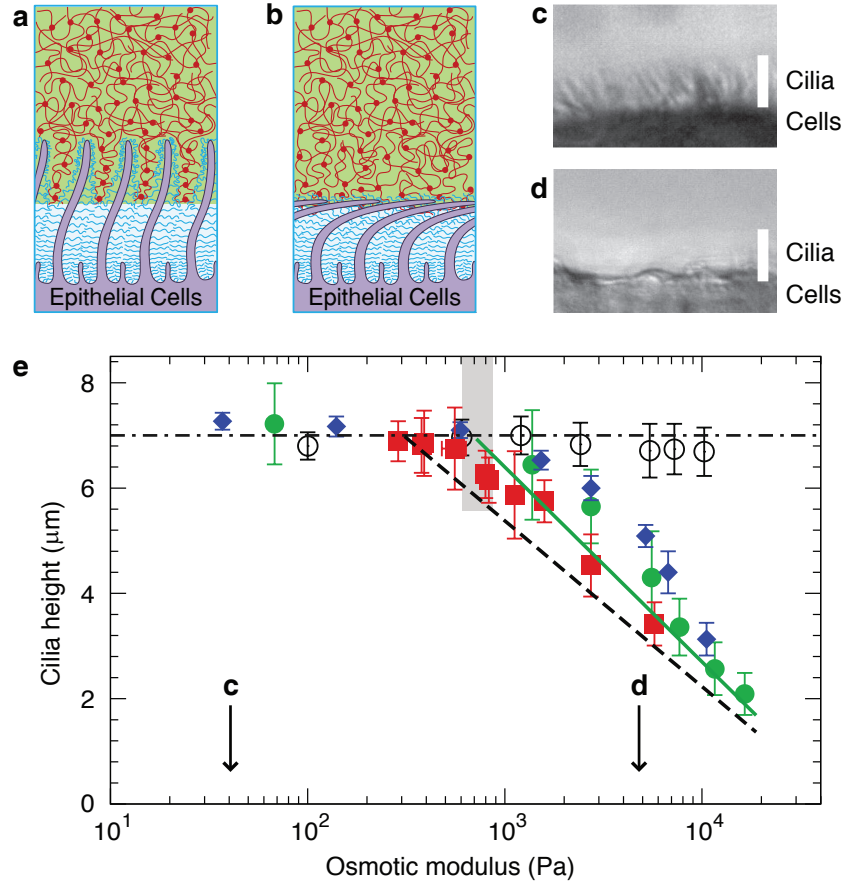
Figure 4.7: Collapse of cilia by mucus and mucus simulants. a, b, Possible scenarios for the compression of the PCL brush by mucus or mucus stimulants with high osmotic modulus (concentration): a, tethered macromolecules are compressed towards the cilia surface without significant deformation of the cilia; b, in addition to the compressed tethered macromolecules, the cilia are also deformed by solutions with high osmotic modulus; c, d, Representative bright-field microscopy images showing the effects of low (c; ~ 300 Pa) and high (d; $\sim 5,000$ Pa) osmotic moduli on cilia height from HBE cultures (viewed in profile). White bars denote the length of fully extended cilia (7 μm). e, Summary plot of the cilia height versus the osmotic moduli of the overlying mucus/mucus simulants, using large, PCL-impermeable dextran ($d > 50$ nm; green solid circles), low melting point agarose ($d \approx 44$ nm; blue solid diamonds), endogenous mucus (red solid squares), and small PCL permeable dextran ($d \approx 2$ nm; black empty circles). Solid green line represents the best linear fit to the dependence of cilia height on the logarithm of osmotic modulus of mucus/mucus stimulants for $K > 1,000$ Pa: $z \approx 7\mu\text{m} - 3.33\mu\text{mlog}\,(K/807\text{Pa})$. Dependence of the exclusion zone $z(K)$ on osmotic modulus of mucus/mucus simulants (Figure 4.5b) is shown for comparison by the dashed black line. Highlighted zone represents the crossover osmotic modulus, $K_{cc} \approx 800 \pm 120$ Pa, above which noticeable decrease of the cilia height was observed.

Note that the interface between the mucus layer and the PCL brush is semipermeable. Thus only the large macromolecules that cannot penetrate the mesh of the

opposing layer, and not the freely permanent salts and small globular proteins, generate the "partial" osmotic pressures/moduli that govern water distribution between the two layers. To test this prediction, HBE cultures were exposed to luminal solutions containing small dextrans ($d \approx 2$ nm) with varying concentrations, and thus, 'total' osmotic moduli. These small dextrans freely enter into the PCL, and hence, are predicted not to produce osmotic compression of PCL brush. Indeed, no changes in the cilia height were observed, even for solutions of small dextrans producing osmotic moduli exceeding $15,000$ Pa (empty circles, Figure 4.7e). Based on these findings, we conclude that it is the large macromolecules in the mucus layer (e.g. secreted mucins which cannot penetrate the PCL) that are the 'partially' osmotically active molecules with respect to the PCL-brush.

4.3 Summary: Brush-like structure stabilizes the periciliary layer for maintaining effective mucus clearance

In this chapter we have demonstrated that in addition to the function of protective layer, the brush-like structure also stabilizes the periciliary layer (PCL) from the osmotic compression of mucus. This osmotic PCL cushion is created by the strong repulsion between overlapping tethered bio-macromolecules in it. It is expected that the PCL is stable (un-collapsed) as long as its osmotic modulus is larger than that of mucus, which is required for maintaining effective mucus clearance. Several important features have been identified:

(i) The PCL has a minimum osmotic modulus with the value $K_0 \simeq 300$ Pa, which is due to the tethered bio-macromolecules that are physically localized within the PCL.

(ii) The osmotic modulus of healthy mucus is smaller than the minimum value K_0 of PCL osmotic modulus. Under this condition the effective mucus clearance is sustained.

(iii) The osmotic modulus of diseased mucus is larger than the minimum value K_0 of osmotic modulus of PCL. Under this diseased condition the mucus clearance slows down (for COPD ~ 1000 Pa) and eventually fails (for CF ~ 3000 Pa).

CHAPTER 5
CONCLUSIONS AND REMARKS: PART I

The "Gel-on-Brush" model represents a fundamentally new description of the structure of airway surface layers. The brush-like periciliary layer enables itself a gradient barrier with permeability (mesh size) decreasing towards cell surface. This gradient permeability is of great biological importance as it suggests that inhaled harmful particulates sneaking through the mucus barrier could be prevented by the PCL from reaching the epithelial surface.

The "Gel-on-Brush" model for the first time provides a consistent biophysical explanation of mucus clearance. This model predicts that the normal mucus layer, with a partial osmotic modulus (~ 200 Pa) lower than the minimal modulus of the periciliary layer ($K_0 \sim 300$ Pa), acts as a reservoir for water in healthy airways, swelling or shrinking in response to depletion or repletion of water on airway surfaces [23].

The "Gel-on-Brush" model also predicts that when the partial osmotic modulus of the mucus layer exceeds the minimal modulus of the periciliary layer (K_0), mucus transport slows and eventually stops, quantitatively explaining the failure of mucus clearance observed in disease, e.g., cystic fibrosis [18]. The resulting immobile mucus forms a nidus for inflammation and bacterial infections [126, 127], leading to chronic lung disease associated with cystic fibrosis and chronic obstructive pulmonary disease (COPD). The increase in the partial osmotic modulus of the mucus layer can reflect either a decrease in the amount of solvent (water), e.g., in cystic fibrosis [18], or an increase in mass of secreted mucins, e.g., in chronic obstructive pulmonary disease (COPD) [17]. Therefore, the "Gel-on-Brush" model has the capacity to unify the pathogenesis of human airways diseases that have in common mucus stasis, inflammation, and infection. [128] Thus, the "Gel-on-Brush" model will yield novel therapeutic

strategies to treat these common human lung diseases that may include therapies designed to restore normal osmotic moduli of mucus layer by hydrating airway surfaces or reducing mucin secretion rates.

Part II

Mobility of Probe Particles in Complex

Fluids

CHAPTER 6
INTRODUCTION

In the beginning of part I we have described the mucociliary clearance system (see chapter 1), in which the main function of mucus is to trap any inhaled particles and thus protects the lung from infection. However, this function also poses a problem for drug delivery, which requires cargos carrying pharmaceutical agents to overcome the mucus barrier. It has been found that motion of non-sticky cargos (nanoparticles) in mucus significantly slows down as their size increases above length scales corresponding to the characteristic structure of mucus [25, 47, 129]. This phenomenon suggests that the motion of a probe particle in complex fluids might reflect their local structure and possibly dynamics.

A class of technology called microrheology based on this idea has emerged within past two decades. The physical basis of microrheology relies on the generalized Stokes-Einstein relation [130–132], from which one can relate the time dependence of the mean-square displacement (MSD) of probe objects, typically spherical particles, to viscoelastic properties of surrounding environments. This technique has been manifested to be versatile and powerful in probing local dynamics of complex fluids [132, 133], including polymer solutions and melts [134–140], bio-macromolecular solutions [141–151], cells [152–158], and colloid suspensions [159].

In addition to the ability to probe bulk rheological properties, microrheology can also probe local inhomogeneities of matrix materials since such inhomogeneities directly determine the behavior of the particle motion. The particle motion could be monitored by using diffusing wave spectroscopy [160], dynamic light scattering [159], laser deflection particle tracking [161], fluorescence correlation spectroscopy [162], or atomic force microscopy [163–165]. Depending on the driving force exerted on probe

particles, microrheology can be broadly classified as active or passive. Probe particles in active microrheology [166] are driven by external forces, typically of magnetic [167] or optical origin [145]; while in the case of passive microrheology probe particles are undergoing thermal motion. The velocity of probe particles in active microrheology is required to be slow enough to be considered within the linear regime if one wants to study the linear viscoelastic properties of probed environments. Compared to active microrheology, therefore, an advantage of passive microrheology is that the requirement of slow velocity of probe particles is always satisfied.

Experimentally it is convenient to link the viscoelastic properties and local inhomogeneities of complex fluids to the MSD of probe particles. The theoretical understanding of particle diffusion in complex fluids, however, is far from being complete and satisfactory. Even for relatively simple systems, such as polymer liquids (solutions and melts) and solids (gels and networks), the diffusion of probe particles in them is not fully understood, though considerable theoretical effort [168–184] (see ref. [185] for a summary) has been devoted. These theoretical works can be divided into two broad classes according to the physical concepts applied. The first class of theories is based on the hydrodynamic interactions between particles and polymers. [168, 173] In dilute polymer solutions chains with size smaller than the particle size are considered as "spheres" with size equal to their hydrodynamic radii. [173] Particles diffusing in dilute polymer solutions experience the hydrodynamic interaction with these effective hard spheres. Semidilute polymer solutions are modeled as a hydrodynamic medium in which polymers are treated as a background of fixed friction centers of monomer beads. [168] The hydrodynamic drag between moving spherical probe particles and fixed monomer beads is assumed to be screened at length scale of solution correlation length [186]. The effects of depletion of polymers near the surface of spherical particles on particle diffusion are considered in refs. [170–172]. All of these theories [168–172] do not take into account the relaxation of polymer matrix and predict an exponential dependence of terminal particle diffusion coefficient (at long time scales) on different powers of particle size and solution concentration (see section 7.2.2 for the discussion).

By contrast we argue that the particle mobility is determined by the dynamics of polymers and terminal particle diffusion coefficient scales as a power law of the particle size and solution concentration.

The second class of theories is based on the concept of "obstruction effect" [174–180], in which the polymer solutions are treated as a "porous" system with "pore size" characterized by the distribution of distances from an arbitrary point in the system to the nearest polymer. This distribution is obtained from a geometric consideration for a suspension of random rigid fibers [174]. The diffusion coefficient of particles is assumed to be linearly proportional to the fraction of "pores" in the polymer solutions with size larger than that of probe particles. This linear assumption fails, however, when polymers overlap at high concentration as the probe particles cannot diffuse through "pores" with size smaller than the particle size. In addition, flexible polymers are very different from rigid fibers as the polymers are coil-like. Therefore, the concentration dependence of "pore" size in coil-like polymer solutions is different from that in solution of rigid fibers. Furthermore, polymers are mobile and therefore particles with size larger than the spacing between "obstacles" (correlation length of polymer solutions) are not permanently hindered by such "obstacles". The mobility of such particles is determined by the polymer dynamics.

In this part of the thesis we present a theoretical description of the thermal motion (related to passive microrheology) of spherical probe particles in polymer liquids (solutions and melts) and solids (gels and networks). We assume that there is no adsorption of polymers onto probe particles and no interaction between probe particles. In chapter 7 we discuss the motion of particles in polymer liquids. The motion of particles in polymer solids (gels and networks) is investigated in chapter 8, in which a novel hopping mechanism is introduced to describe the motion of particles with size larger than the network mesh size. In chapter 9 we extend our results of particles in polymer liquids and solids to reversible polymer liquids in which the crosslinks are temporary and thus can reorganize. Conclusions and remarks are presented in chapter 10.

CHAPTER 7

MOBILITY OF PARTICLES IN POLYMER LIQUIDS

Mobility of particles in polymer liquids depends on the relative particle size with respect to two important length scales. The first one is the correlation length ξ, defined as the average distance from a monomer on one chain to the nearest monomer on another chain. [60] This length is on the order of polymer size at the overlap concentration (ϕ^*) and decreases as a power of concentration (volume fraction) ϕ (thick line in Figure 7.1):

$$\xi\left(\phi\right) \simeq b\phi^{-v/(3v-1)} \tag{7.1}$$

where b is the length of the Kuhn segment and v is the Flory exponent that depends on the solvent quality. The correlation length in a theta solvent (with $v = 1/2$) decreases with concentration as $\xi \simeq b\phi^{-1}$, while in an athermal solvent ($v = 0.588$) the correlation length decreases as $\xi \simeq b\phi^{-0.76}$. The second important length scale is the entanglement length (tube diameter) a [60, 187, 188], which is typically a factor of 5 larger than the correlation length ξ and is proportional to ξ in athermal solvent (medium line in Figure 7.1)

$$
\begin{aligned}
a\left(\phi\right) & \simeq & a\left(1\right)\phi^{-v/(3v-1)} \\
& \sim & \phi^{-0.76} \sim \xi, \quad \text{for athermal (or good) solvent}
\end{aligned} \tag{7.2}
$$

but has a different concentration dependence in a theta solvent [60]

$$a \simeq a\left(1\right)\phi^{-2/3}, \quad \text{for theta solvent} \tag{7.3}$$

Here $a\left(1\right)$ is the tube diameter in polymer melt with a typical value $a\left(1\right) \simeq 5$ nm. The size of a polymer chain of N Kuhn segments

$$R \simeq bN^{1/2}\phi^{-(2v-1)/(6v-2)}, \quad \text{for } \phi^* < \phi < \phi^{**} \tag{7.4}$$
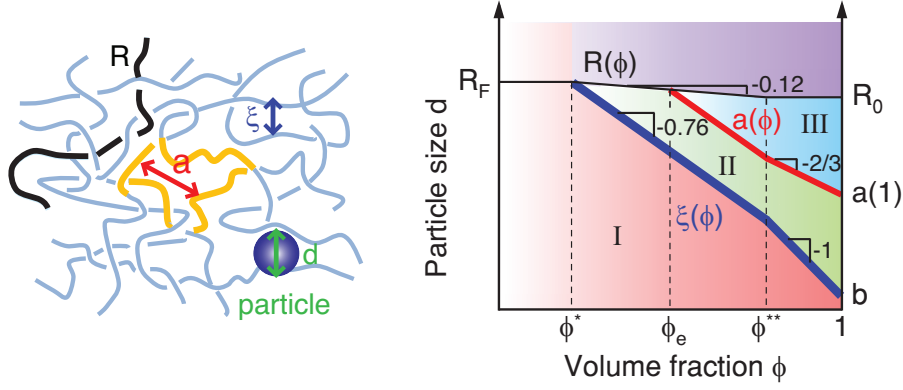
Figure 7.1: Three regimes for mobility of probe particles with size d in polymer solution with volume fraction ϕ shown in the (ϕ, d) parameter space: regime I for small particles ($b < d < \xi$), regime II for intermediate particles ($\xi < d < a$), and regime III for large particles ($d > a$). Solid lines represent the crossover boundaries between different regimes. Thick and intermediate lines correspond to the dependencies of correlation length ξ and tube diameter a in good solvent on volume fraction ϕ, while thin (top) line describes concentration dependence of polymer size $R(\phi)$. R_F is the chain size in dilute polymer solution in a good solvent and R_0 corresponds to the chain size in a polymer melt. Dashed lines represent crossovers between regimes of polymer solution at different concentrations: (1) the dilute solution regime with $0 < \phi < \phi^*$, where ϕ^* is polymer overlap concentration; (2) the semidilute unentangled solution regime with $\phi^* < \phi < \phi_e$, where ϕ_e is the concentration at which polymers start to entangle with each other; (3) the semidilute entangled solution regime with $\phi_e < \phi < \phi^{**}$; (4) the concentrated entangled solution regime with $\phi^{**} < \phi < 1$ [60]. Logarithmic scales.

is independent of volume fraction ϕ for theta solvent ($v = 1/2$) and has a very weak concentration dependence in athermal (or good) solvent ($v = 0.588$) (see thin line in Figure 7.1): $R \simeq bN^{1/2}\phi^{-0.12}$. Here ϕ^{**} is the crossover concentration between semidilute solution regime with partially swollen chains and the concentrated solution regime with ideal chain statistics. [60]

The scaling theory for mobility of probe particles of different shapes in polymer melt has been developed by Brochard-Wyart and de Gennes [189]. We extend the ideas of ref. [189], in which only the terminal diffusion coefficient (at long time scales) of probe particles in polymer melt is discussed, to describe the mobility of spherical particles in polymer liquids over a wide range of concentration and time scales. In section 7.1 we present our prediction for the mean-square displacement of probe particles of various sizes in polymer liquids at different time scales. We show that there are three

regimes depending on the particle size: 1) mobility of small particles ($d < \xi$) is not much affected by the surrounding polymers, 2) motion of intermediate size particles ($\xi < d < a$) is coupled to segmental motion of the polymers, and 3) large particles ($d > a$) are affected by entanglements. The contribution of hopping diffusion to the mobility of large particles ($d > a$) trapped in entanglement cages is not taken into account for the case of polymer liquids and will be elaborated in section 8.5 in chapter 8. Section 7.2 deals with the dependencies of terminal particle diffusion coefficient on solution concentration, particle size, and polymer molecular weight and these predictions are compared with existing experimental and simulation data as well as prior theoretical models. Concluding remarks and future research directions of investigations are discussed in section 7.3.

7.1   Mean-square displacement

7.1.1   Small particles

If the diameter d of a probe particle is smaller than the solution correlation length ξ (see regime I in Figure 7.1), the motion of the particle is not much affected by polymers and is very similar to particle diffusion in a pure solvent. Mean-square displacement of particles (see dash-dotted line in Figure 7.2) in this regime is

$$\left\langle \Delta r^2 \left(t\right) \right\rangle \simeq D_s t, \quad \text{for } t > \tau_0 \tag{7.5}$$

Here τ_0 is the monomer relaxation time

$$\tau_0 \simeq \eta_s b^3 / \left(k_B T\right) \tag{7.6}$$

in which k_B is Boltzmann constant and T is absolute temperature. The particle diffusion coefficient is determined by solvent viscosity η_s and is reciprocally proportional to the particle diameter d (Stokes-Einstein relation)

$$D_s \simeq k_B T / \left(\eta_s d\right) \tag{7.7}$$

Particle diffusion coefficient decreases by a factor on the order of two with respect to its value D_s in pure solvent as the solution concentration crosses from regime I to regime II, in which the solution correlation length ξ becomes smaller than the particle size d. Here and below we drop all numerical coefficients and keep our analysis at the scaling level.
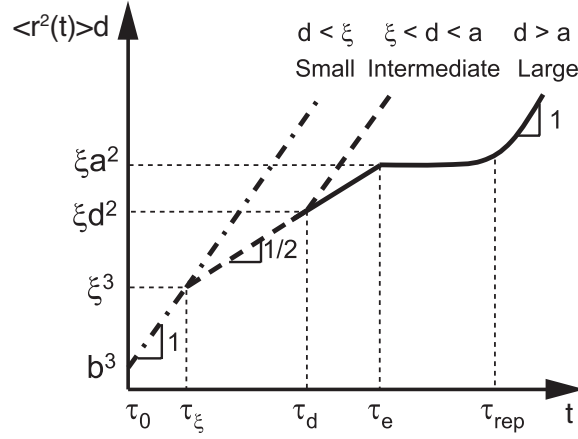
Figure 7.2: Time dependence of the product of mean-square displacement $\langle \Delta r^2(t) \rangle$ and the particle size d for small particles ($b < d < \xi$, dash-dotted line), intermediate size particles ($\xi < d < a$, dashed line), and large particles ($d > a$, solid line) in polymer solutions ($\xi \simeq b$ in polymer melts). Here τ_0 is the relaxation time of a monomer (eq. 7.6), τ_ξ (eq. 7.8) is the relaxation time of a correlation blob, τ_d (eq. 7.12) is the relaxation time of a polymer segment with size comparable to particle size d, τ_e (eq. 7.15) is the relaxation time of an entanglement strand, and $\tau_{\rm rep}$ (eq. 7.18) is the relaxation (reptation) time of a whole polymer chain. Logarithmic scales.

7.1.2 Intermediate size particles

Motion of particles of size larger than the correlation length ξ (in polymer melt $\xi \simeq b$) but smaller than the tube diameter a (see regime II in Figure 7.1) is not affected by chain entanglements, but is affected by polymer dynamics. There are three regimes for the mean-square displacement of these intermediate size particles at different time scales. At short time scales the motion of such particles is diffusive (see eq. 7.5 and left part of the dashed line in Figure 7.2) as particles "feel" local solution viscosity

comparable to that of solvent. This diffusive regime continues up to the time scale

$$\tau_\xi \simeq \eta_s \xi^3/(k_B T) \simeq \tau_0 \left(\xi/b\right)^3 \tag{7.8}$$

which corresponds to the relaxation time of a correlation blob with size ξ. At time t longer than τ_ξ the motion of intermediate size particles is sub-diffusive as it is coupled to the fluctuation modes of the polymer solution. The polymer mode with relaxation time t involves the motion of a section of the chain containing $(t/\tau_\xi)^{1/2}$ correlation blobs (see Chapter 8 in ref. [60]). The effective viscosity "felt" by particles at time scale t is the viscosity of a solution with polymers of size equal to the chain section size $\xi(t/\tau_\xi)^{1/4}$. This effective viscosity is higher than the solvent viscosity by the factor on the order of the number of correlation blobs in the corresponding chain section

$$\eta_{\mathrm{eff}}(t) \simeq \eta_s(t/\tau_\xi)^{1/2}, \quad \text{for } \tau_\xi < t < \tau_d \tag{7.9}$$

The effective diffusion coefficient of these particles decreases with time as

$$D_{\mathrm{eff}}(t) \simeq k_B T/\left(\eta_{\mathrm{eff}}\left(t\right) d\right) \simeq D_s(t/\tau_\xi)^{-1/2}, \quad \text{for } \tau_\xi < t < \tau_d \tag{7.10}$$

and the mean-square displacement of the particle is proportional to the square root of time

$$\left\langle \Delta r^2\left(t\right)\right\rangle \simeq D_{\mathrm{eff}}(t)t \simeq D_s\left(\tau_\xi t\right)^{1/2}, \quad \text{for } \tau_\xi < t < \tau_d \tag{7.11}$$

This sub-diffusive regime (see the middle part of the dashed line in Figure 7.2) continues until the time scale τ_d at which the size of chain sections controlling viscosity is comparable with the particle size $\xi(\tau_d/\tau_\xi)^{1/4} \simeq d$.

$$\tau_d \simeq \tau_\xi(d/\xi)^4 \tag{7.12}$$

At longer times ($t > \tau_d$) the motion of intermediate size particles is diffusive ($\left\langle r^2\left(t\right)\right\rangle \simeq D_t t$) with a terminal diffusion coefficient (see the right part of the dashed line in Figure 7.2)

$$D_t \simeq \frac{k_B T}{\eta_{\mathrm{eff}}\left(\tau_d\right) d} \simeq \frac{k_B T \xi^2}{\eta_s d^3}, \quad \text{for } t > \tau_d \tag{7.13}$$

where we used equations 7.9 and 7.12 for η_{eff} and τ_d. Note that the mean-square displacement of particles at the onset of this terminal Brownian diffusion (at time τ_d) is ξd

(dashed line in Figure 7.2), and the diffusion coefficient is proportional to the square of the correlation length and inversely proportional to the cube of the particle size (see eq. 7.13). The reason for this extra factor of $(\xi/d)^2$ in the diffusion coefficient (eq. 7.13) is that the effective viscosity "felt" by the particles at long times is proportional to the number of correlation blobs in a chain section with size on the order of particle diameter,

$$\eta_{\text{eff}} \simeq \eta_s (d/\xi)^2, \quad \text{for } t > \tau_d \tag{7.14}$$

The correlation length in polymer melts is on the order of monomer size ($\xi \simeq b$) and equation 7.14 becomes $\eta_{\text{eff}} \simeq \eta_s (d/b)^2$ [189]. Note that none of the above results depends on the polymer molecular weight as long as the tube diameter a and/or polymer size R is larger than the particle size d.

7.1.3 Large particles

Particles larger than the size of entanglement mesh ($d > a$, where a is entanglement tube diameter [60, 187, 188]) are trapped by the entanglements. The arrest of particle motion occurs on time scale on the order of the relaxation time of an entanglement strand:

$$\tau_e \simeq \tau_\xi (a/\xi)^4 \simeq \tau_0 (\xi/b)^3 (a/\xi)^4 \tag{7.15}$$

At short time scales $t < \tau_e$ the motion of large particles follows the same time dependence as that of intermediate ones for the first two regimes (see section 7.1.2). The mean-square displacement of these large particles at time scale τ_e

$$\left\langle \Delta r^2 \left(\tau_e \right) \right\rangle \simeq a^2 \xi / d \tag{7.16}$$

depends on all three important length scales: the tube diameter a, the correlation length ξ, and the particle size d. The plateau modulus of the semidilute solution can be obtained from this mean-square displacement (eq. 9.37 in ref. [60])

$$G_e \simeq k_B T / \left(\left\langle \Delta r^2 \left(\tau_e \right) \right\rangle d \right) \simeq k_B T / \left(a^2 \xi \right) \tag{7.17}$$

Note that if we consider the polymer solution as a "melt" of correlation blobs, the volume occupied by an entanglement strand is $\xi^3 (a/\xi)^2 \simeq a^2\xi$, and eq. 7.17 is consistent with plateau modulus corresponding to thermal energy $k_B T$ per entanglement strand. We stress out that the relation (eq. 7.17) between solution plateau modulus and the plateau mean-square displacement of a probe particle (eq. 7.16) is identical (up to numerical factors on the order of unity) to the one obtained via the generalized Stokes-Einstein relation that equates the long time limit of the mean-square displacement of a particle with the zero-frequency shear modulus in an elastic solid [131]. This self-consistency between a polymer-dynamics-based scaling model and the fluctuation-dissipation theorem, that makes no assumptions about microscopic dynamics, further validates the approach relating the particle mean-square displacement to rheology.

The motion of large particles at time scales longer than τ_e can proceed by two mechanisms. The first one is the reptation of surrounding polymers leading to the release of topological constraints at the reptation time τ_{rep}, which is proportional to the cube of the number of entanglements (N/N_e) per chain

$$\tau_{\text{rep}} \simeq \tau_e (N/N_e)^3 \tag{7.18}$$

Here N_e is the number of monomers per entanglement strand. Tube length fluctuations [60] lead to even stronger dependence of reptation time on the degree of polymerization: $\tau_{\text{rep}} \sim N^{3.4}$. The second mechanism that could lead to the motion of particles is due to fluctuations of local entanglement mesh that will allow particles to pass through entanglement gates and thus hop between neighboring entanglement cages. The contribution of hopping process will be important for diffusion of particles not significantly larger ($d \gtrsim a$) than the tube diameter of entangled polymer solutions. This hopping mechanism will be discussed in chapter 8. Below we focus on the motion of large particles due to chain reptation.

At time scales shorter than τ_{rep} large particles ($d > a$) are trapped by entanglements

and their mean-square displacement is on the order of $a^2\xi/d$ (eq. 7.16)

$$\left\langle \Delta r^2\left(t\right) \right\rangle \simeq a^2\xi/d, \quad \text{for } \tau_e < t < \tau_{\text{rep}} \tag{7.19}$$

The motion of particles resulting from chain reptation at longer times ($t > \tau_{\text{rep}}$) is Brownian with diffusion coefficient determined by the bulk solution viscosity η

$$\left\langle \Delta r^2\left(t\right) \right\rangle_{\text{rep}} \simeq \frac{k_B T}{\eta d}t, \quad \text{for } t > \tau_{\text{rep}} \tag{7.20}$$

where the viscosity $\eta \simeq G_e \tau_{\text{rep}}$ increases as high powers of the degree of polymerization N and solution concentration [60]. Eq. 7.20 can also be rewritten as

$$\left\langle \Delta r^2\left(t\right) \right\rangle_{\text{rep}} \simeq \left(\xi a^2/d\right) t/\tau_{\text{rep}}, \quad \text{for } t > \tau_{\text{rep}} \tag{7.21}$$

Diffusion coefficient of large probe particles due to chain reptation is

$$D_{\text{rep}} \simeq k_B T/\left(\eta d\right) \simeq \xi a^2/\left(d\tau_{\text{rep}}\right), \quad \text{for } d > a \tag{7.22}$$

7.1.4 Microrheology
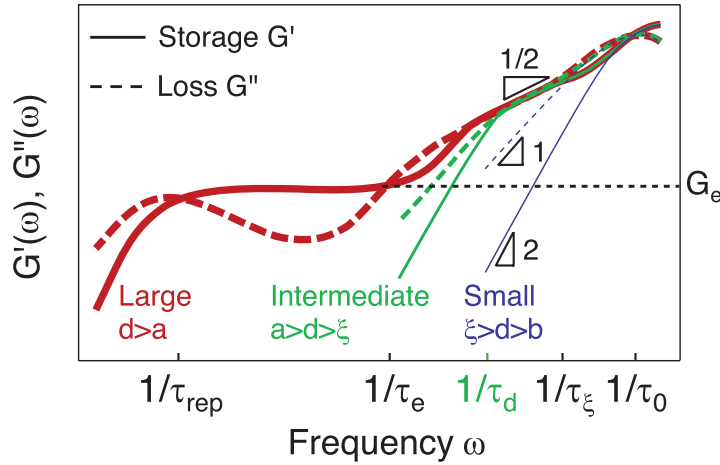
Figure 7.3: Viscoelastic properties of polymer liquids predicted from time-dependent mean-square displacements of small particles ($d < \xi$, black thin line), intermediate size particles ($\xi < d < a$, green medium lines), and large particles ($d > a$, red thick lines). Solid lines correspond to storage moduli G' and dashed lines represent loss moduli G'' as functions of frequency ω. Logarithmic scales.

The viscoelastic properties of polymer liquids can be determined from the time de-pendence of the mean-square displacements of probe particles within a wide frequency

range by using generalized Stokes-Einstein relation (GSE) [130, 131]. The GSE relates the viscoelastic spectrum $\tilde{G}(s)$ of polymer liquids to the Laplace transform $\langle \Delta \tilde{r}^2(s) \rangle$ of mean-square displacement $\langle \Delta r^2(t) \rangle$:

$$\tilde{G}(s) = \frac{2k_B T}{\pi d s \langle \Delta \tilde{r}^2(s) \rangle} \tag{7.23}$$

where s is the Laplace frequency. According to the Kramers–Kronig relations, storage modulus $G'(\omega)$ and loss modulus $G''(\omega)$ correspond to the real and imaginary parts of complex modulus $G^*(\omega)$, which is determined by substituting $i\omega$ for the Laplace frequency s in eq. 7.23 .

Figure 7.3 shows the viscoelastic properties of polymer liquids predicted from time-dependent mean-square displacements of particles with different sizes. Small particles ($d < \xi$) probe solvent-like viscosity within entire frequency range (see thin line in Figure 7.3). Intermediate size particles ($\xi < d < a$) also experience solvent-like viscosity at high frequencies ($1/\tau_\xi < \omega < 1/\tau_0$). However, at frequencies lower than $1/\tau_\xi$ they probe segmental dynamics of polymer liquids (see medium lines in Figure 7.3). Particles with size larger than the tube diameter ($d > a$) are expected to probe full dynamics of the polymer liquids (thick lines in Figure 7.3). Similar to intermediate size particles, large particles probe solvent-like viscosity at high frequencies ($1/\tau_\xi < \omega < 1/\tau_0$) and probe the segmental dynamics of polymer liquids at frequencies $1/\tau_e < \omega < 1/\tau_\xi$. At intermediate frequencies ($1/\tau_{\mathrm{rep}} < \omega < 1/\tau_e$) the large particles are trapped by entanglements and probe the entanglement plateau modulus (see eq. 7.17). At very low frequencies ($\omega < 1/\tau_{\mathrm{rep}}$) large particles experience bulk viscosity. It is important to point out that the probe particles in microrheology must be non-sticky, so that they do not form strong physical or chemical bonds with surrounding materials.
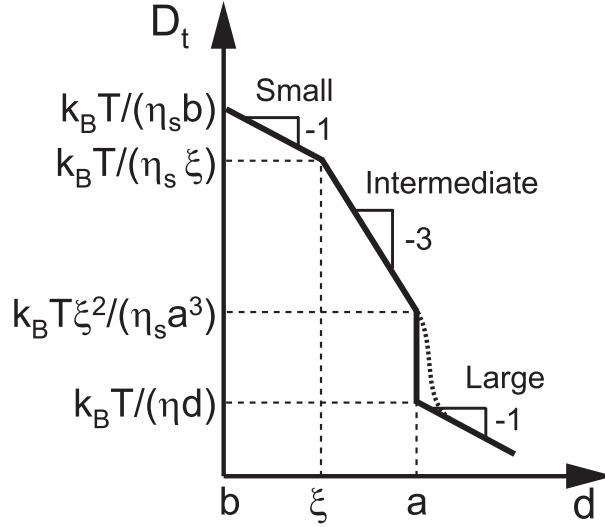
Figure 7.4: Dependence of terminal particle diffusion coefficient D_t on particle size d in entangled polymer solutions. Dotted line corresponds to the crossover taking into account the contribution of hopping process to the particle mobility. Logarithmic scales.

7.2 Particle diffusion coefficient

7.2.1 Dependence on particle size

In section 7.1 we have discussed the time dependence of mean-square displacements of probe particles of different sizes in polymer liquids with fixed volume fraction (concentration). The mobility of particles in polymer liquids is investigated for three main cases depending on the size of probe particles: small particles ($d < \xi$) (regime I in Figure 7.1 and section 7.1.1), intermediate particles ($\xi < d < a$) (regime II in Figure 7.1 and section 7.1.2), and large particles ($d > a$) (regime III in Figure 7.1 and section 7.1.3). In Figure 7.4 we sketch the dependence of terminal diffusion coefficient D_t on particle size d. For small probe particles with size d smaller than the solution correlation length ξ the diffusion coefficient D_t follows the classical Stokes-Einstein relation (see eq. 7.7) and is mainly determined by the solvent viscosity η_s, as shown by the first section of the curve in Figure 7.4. Terminal diffusion coefficient D_t of intermediate size particles ($\xi < d < a$) has a much stronger dependence on particle size (see eq. 7.13) because they "feel" effective viscosity that increases as square of the particle size

67

(eq. 7.14), as shown by the second section of the curve in Figure 7.4. As long as the particle size is smaller than the tube diameter the terminal particle diffusion coefficient is independent of polymer molecular weight. The diffusion coefficient of particles with size larger than the tube diameter ($d > a$) (regime III in Figure 7.1 and section 7.1.3) is determined by chain reptation process and particles "feel" full solution viscosity η (see eq. 7.22). Note that our scaling calculation suggests a sharp drop of the terminal diffusion coefficient of particles with size on the order of the tube diameter ($d \simeq a$) by a large factor $(N/N_e)^3$, as shown in Figure 7.4. This sharp crossover is broadened (see the dotted line in Figure 7.4) by the contribution to particle mobility from the hopping diffusion process. [190]

As mentioned in section 7.1.3, the mobility of particles with size d larger than the tube diameter a is due to both chain reptation and hopping processes. To hop from one entanglement cage to a neighboring one the particle has to overcome an entropic energy barrier that increases with the ratio of particle size d to the tube diameter a. Thus, the waiting time required for the hopping process increases exponentially with this ratio d/a. This waiting time, however, can still be shorter than the relaxation of time of the whole polymer system as long as the particle size is not significantly larger than the tube diameter. Therefore, the motion of particles with size slightly larger than the tube diameter will be dominated by the hopping process with diffusion coefficient decreasing exponentially with the ratio of particle size to the tube diameter as $D \sim \exp(-d/a)$ (see chapter 8), shown by the dotted line in Figure 7.4; whereas diffusion of very large particles ($d \gg a$) is primarily controlled by the chain reptation process.

It is important to point out that the hopping-controlled diffusion does not probe the macroscopic viscosity of the polymer solutions. In fact this process is possible even in entangled polymer networks with infinite zero-shear-rate viscosity. The sharp crossover with exponentially strong decrease of the diffusion coefficient of particles with size d increasing above the tube diameter a is qualitatively different from the smooth crossover of the diffusion coefficient of linear probe chains from below to above

the entangled molecular weight [191]. As the size of the linear probe polymers crosses from below to above the tube diameter, the molecular weight dependence of the diffusion coefficient smoothly crosses from $D \sim 1/N$ to $D \sim 1/N^{2.3}$, which is unlike the exponentially sharp decrease expected for particles (see Figure 7.4). In order to understand the reason for this qualitative difference between linear chains and particle probes, consider the limiting case with very long matrix chains of entangled polymer solutions. The linear probe chains of size larger than the tube diameter can reptate out of their original tubes and diffuse without encountering any significant entropic energy barrier. [1] However, particles with size several times larger than the tube diameter $(d > a)$ is exponentially slowed down by the free energy barrier and these particles are effectively trapped by entanglement cages.

The diffusion coefficient of intermediate size particles is predicted to be inversely proportional to the cube of particle size: $D_t(d) \sim d^{-3}$ (see eq. 7.13). This prediction of our model and also earlier ref. [189] has been verified by the molecular dynamics (MD) simulations of diffusion of particles with different sizes in unentangled polymer melts. [193]

7.2.2 Dependence on solution concentration

Experimentally it is often easier to systematically vary polymer concentration rather than the particle size. Terminal diffusion coefficient of particles of a given size d depends on the relative value of this size d with respect to two concentration-dependent length scales: the correlation length $\xi(\phi)$ (thick line in Figure 7.1) and the tube diameter $a(\phi)$ (medium line in Figure 7.1).

Mobility of probe particles with the intermediate size d larger than the monomer size b but smaller than the tube diameter $a(1)$ of a polymer melt crosses over from regime I to regime II (see Figure 7.1) as solution concentration ϕ increases. The

---

[1]For very large probe chains $(N > N_e^3)$ there is a prediction of an entropic free energy barrier. [192]
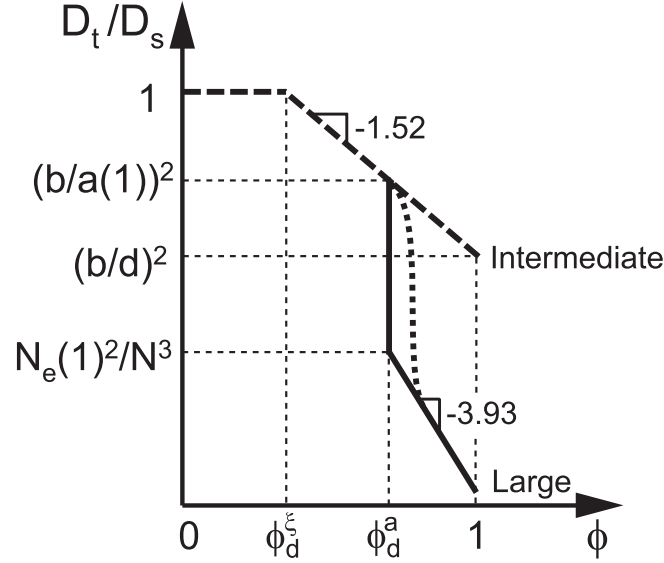
Figure 7.5: Concentration dependence of terminal diffusion coefficient D_t of particles in entangled athermal polymer solutions normalized by their diffusion coefficient $D_s = k_B T/(\eta_s d)$ in pure solvent (see eq. 7.7). Dashed line is for intermediate size particles ($b < d < a\,(1)$) and solid line is for large particles ($d > a\,(1)$). The crossover concentrations ϕ_d^ξ and ϕ_d^a, at which the correlation length ξ and the tube diameter a are on the order of particle size d, are defined in eqs. 7.24 and 7.26 respectively. Dotted line corresponds to the crossover taking into account the contribution of hopping process to the particle mobility (see discussion in section 7.2.1 and chapter 8). Logarithmic scales.

crossover solution concentration between these two regimes is

$$\phi_d^\xi \simeq (d/b)^{-(3v-1)/v} \qquad (7.24)$$

at which the correlation length $\xi(\phi_d^\xi)$ is on the order of particle diameter d. In a theta solvent ($v = 1/2$) the crossover volume fraction is $\phi_d^\xi \simeq (d/b)^{-1}$ and in an athermal solvent ($v = 0.588$) it is $\phi_d^\xi \simeq (d/b)^{-1.32}$. Below this volume fraction (for $\phi < \phi_d^\xi$) the diffusion coefficient of particles is determined by the solvent viscosity η_s and is almost concentration independent (see eq. 7.7). At volume fractions above ϕ_d^ξ particles "feel" segmental motions of polymers (see eq. 7.10) and particle diffusion coefficient

$$D_t\,(\phi) \simeq \frac{k_B T \xi^2}{\eta_s d^3} \simeq \frac{k_B T b^2}{\eta_s d^3}\phi^{-2v/(3v-1)}, \quad \text{for } \phi_d^\xi < \phi < 1 \text{ and } b < d < a\,(1) \quad (7.25)$$

decreases with solution volume fraction as power -2 for theta solvent and -1.52 for athermal solvent (see dashed line in Figure 7.5).

If the particle size d is larger than the tube diameter $a\,(1)$ in the melt, in addition

to the two regimes expected for particles smaller than $a(1)$ (see dashed line in Figure 7.5), there is an additional regime in which particle diffusion coefficient is determined by chain reptation. This regime begins at a solution concentration ϕ_d^a, at which the tube diameter a (see eq. 7.2) is on the order of the particle size d: $a\left(\phi_d^a\right) \simeq d$. In a theta solvent $a \simeq a\left(1\right)\phi^{-2/3}$ (see eq. 7.3) and in an athermal solvent $a \simeq a\left(1\right)\phi^{-0.76}$ (see eq. 7.2), therefore the corresponding crossover concentrations are

$$\phi_d^a \simeq \begin{cases} \left(d/a\left(1\right)\right)^{-3/2}, & \text{theta} \\ \left(d/a\left(1\right)\right)^{-1.32}, & \text{athermal} \end{cases} \tag{7.26}$$

Large probe particles ($d > a\left(1\right)$) are expected to experience full solution viscosity above the crossover concentration ϕ_d^a. The terminal particle diffusion coefficient in this regime (see solid line in Figure 7.5) $D_t\left(\phi\right) \simeq D_{\mathrm{rep}} \simeq \xi a^2/\left(d\tau_{\mathrm{rep}}\right)$ is dominated by the contribution from the chain reptation process (see eq. 7.22). Recall the relations $\tau_e \simeq \tau_0\left(\xi/b\right)^3\left(a/\xi\right)^4$ (see eq. 7.15) and $\tau_{\mathrm{rep}} \simeq \tau_e\left(N/N_e\left(\phi\right)\right)^3$ (see eq. 7.18) and using eqs. 7.1, 7.2, 7.15, and the relation

$$N_e(\phi) \simeq N_e\left(1\right) \begin{cases} \phi^{-4/3}, & \text{theta} \\ \phi^{-1.32}, & \text{athermal} \end{cases} \tag{7.27}$$

one can simplify eq. 7.22 to obtain the concentration dependence of terminal particle diffusion coefficient:

$$D_t\left(\phi\right) \simeq \frac{k_B T}{\eta_s d}\frac{N_e\left(1\right)^2}{N^3} \begin{cases} \phi^{-14/3}, & \text{theta} \\ \phi^{-3.93}, & \text{athermal} \end{cases} \quad \text{for } \phi_d^a < \phi < 1 \text{ and } d > a\left(1\right)$$

$$\tag{7.28}$$

which is the reciprocal of the concentration dependence of solution viscosity $\eta\left(\phi\right)$ (eq. 9.45 in ref. [60]).

We test our scaling prediction on the concentration dependence of the diffusion coefficient of intermediate size particles (eq. 7.25 and Figure 7.5) using the data from ref. [136], in which the authors measured the diffusion coefficient of gold nanoparticles with diameter $d = 5$ nm in 240 kDa polystyrene/toluene (good solvent) solutions at several solution concentrations by fluctuation correlation spectroscopy. For all solution
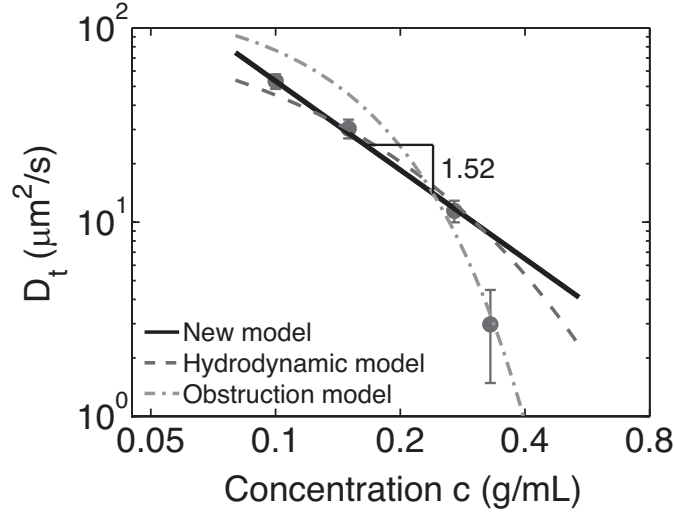
Figure 7.6: Diffusion coefficient of 5 nm gold nanoparticles in semidilute solutions of polystyrene in toluene. Solid circles are data from ref. [136] for $M_w = 240$ kDa polystyrene/toluene solutions above the overlap concentration. Lines are predictions of different models: solid line—our scaling model (eqs. 7.25 and 7.29 with $\alpha = 0.53$), dashed line—hydrodynamic model (eq. 7.31 with $k^{\mathrm{hydro}} = 0.96$), dash-dotted line— obstruction model (eq. 7.32 with $k^{\mathrm{obst}} = 0.43$).

concentrations studied in ref. [136] the size of nanoparticles is larger than the solution correlation length but smaller than the tube diameter (in an entangled polystyrene melt $a(1) \simeq 9$ nm [60]), and therefore, the data points are in the intermediate particle size regime ($\xi < d < a$). The particle diffusion coefficients (see points in Figure 7.6) at low concentrations exhibit a power law dependence on concentration: $D_t(c) \sim c^{-1.52\pm0.15}$, which is in good agreement with our scaling prediction (eq. 7.25). Note that one data point at higher concentration corresponds to lower diffusion coefficient and much larger error bar, possibly due to degradation of laser focus at such high solution concentration. For a good (athermal) solvent eq. 7.25 can be rewritten as

$$D_t(c) = \alpha D_s (c/c_d^\xi)^{-1.52} \tag{7.29}$$

where D_s is the particle diffusion coefficient in pure solvent, c_d^ξ (eq. 7.24) corresponds to the solution concentration at which the particle size d is equal to the solution correlation length ξ, and α is the scaling prefactor to be determined by fitting the scaling prediction to experimental data. The measured diffusion coefficient D_s of the 5 nm gold nanoparticles in pure solvent (toluene) is about $141 \mu\mathrm{m}^2/\mathrm{s}$ [136] and the crossover

concentration c_d^ξ is about 0.08 g/ml [2]. The coefficient $\alpha \simeq 0.53$ obtained by fitting the scaling model to the three experimental points at lower concentrations is on the order of unity confirming the consistency of the scaling estimate (eq. 7.29 and solid line in Figure 7.6).

Earlier models [168, 180] predict stronger than power law concentration dependence of diffusion coefficient. The theories based on the concept of hydrodynamic interaction (hydrodynamic models) [168] predict the exponential dependence of the particle diffusion coefficient on the ratio of particle size d and the solution correlation length ξ

$$D_t = D_s \exp\left(-k^{\text{hydro}} d/\xi\right) \tag{7.30}$$

In good solvent (eq. 7.1 with $v = 0.588$) this prediction corresponds to the stretched exponential concentration dependence of particle diffusion coefficient

$$D_t\left(c\right) = D_s \exp\left(-k^{\text{hydro}}\left(c/c_d^\xi\right)^{0.76}\right) \tag{7.31}$$

With the values of $D_s = 141 \mu\text{m}^2/\text{s}$ and $c_d^\xi = 0.08$ g/ml fixed by separate experiments one can adjust parameter k^{hydro} to fit this prediction (eq. 7.31) to experimental data. The best fit of this prediction to the three experimental points at lower concentration, shown by the dashed line in Figure 7.6, is qualitatively similar (slightly worse) than that of our scaling prediction.

Terminal particle diffusion coefficient predicted by the theories based on the "obstruction effect" (obstruction model) [180] has an even stronger dependence on the ratio of particle size d and the correlation length ξ: $D_t = D_s \exp\left(-\pi\left((d+\delta)/(\xi+\delta)\right)^2/4\right)$, where δ corresponds the effective cylindrical diameter of a polymer chain considering it as a rigid fiber. The value of δ can be estimated by $\delta \simeq v_0/b^2$, where v_0 is the Kuhn monomer volume and can be obtained from a polymer handbook. [195] Typically the

---

[2]The crossover solution concentration $c_d^\xi \simeq 0.08$ g/ml for 5 nm gold nanoparticles is estimated by expression $c_d^\xi = c^* \left(R_g/d\right)^{1.32}$ (refer to eq. 7.24), in which $c^* \simeq 0.015$ g/ml [136] and the radius of gyration R_g of a 240 kDa poly-styrene chain in toluene is approximately 19 nm as estimated by data from ref. [194]

value of $\delta \sim 0.3$ nm is negligible compared with both the particle size d and the correlation length ξ. Therefore, the prediction of the obstruction model can be rewritten as

$$D_t\left(c\right) = D_s \exp\left(-k^{\mathrm{obst}}\left(d/\xi\right)^2\right) = D_s \exp\left(-k^{\mathrm{obst}}\left(c/c_d^\xi\right)^{1.52}\right) \qquad (7.32)$$

Similar to that in hydrodynamic model the adjustable parameter k^{obst} in the obstruction model is determined by fitting this prediction to the three experimental points at lower concentrations with the fixed values of $D_s = 141\ \mu\mathrm{m}^2/\mathrm{s}$ and $c_d^\xi = 0.08$ g/ml. The best fit of the data by the obstruction model, shown by the dash-dotted line in Figure 7.6, is qualitatively similar (slightly worse) than that of both hydrodynamic and our scaling models.

In spite of the similarities of the three fits to the experimental data at lower concentrations (Figure 7.6), we claim that our model is the qualitatively correct one, as it properly takes into account coupling between polymer dynamics and particle motion, which is the very basis of microrheology. Note that both hydrodynamic and obstruction models completely ignore polymer dynamics and thus are not applicable to the case of particle diffusion in polymer melts. In section 7.2.4 below we demonstrate that our scaling model describes particle diffusion both in polymer melts and polymer solutions in a consistent way by constructing a "universal" plot.

7.2.3 Dependence on polymer size

Consider the motion of probe particles of fixed size d in polymer solutions with different degrees of polymerization N but with the same concentration ϕ. Terminal diffusion coefficient of small particles with the size smaller than the correlation length is almost independent of the polymer molecular weight (dashed line in Figure 7.7) because these particles "feel" viscosity close to that of solvent.

As illustrated by the dash-dotted line in Figure 7.7, intermediate size particles ($\xi <$
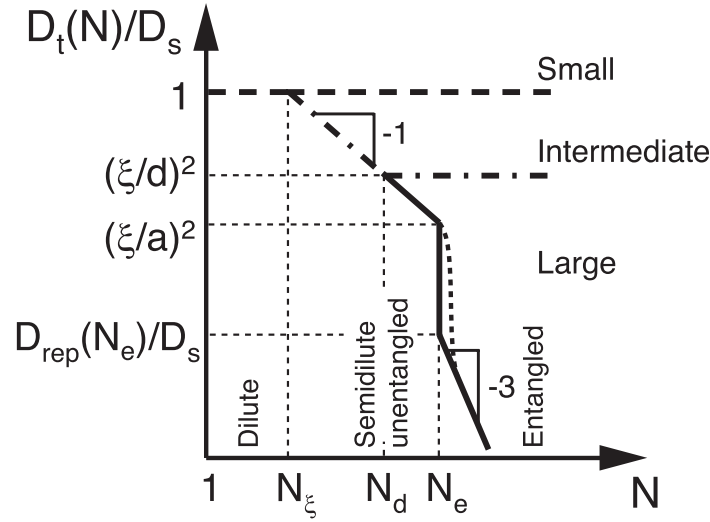
Figure 7.7: Dependence of the normalized terminal diffusion coefficient D_t/D_s of particles in solutions with fixed concentration on degree of polymerization N, where particle diffusion coefficient in pure solvent D_s is defined in eq. 7.7. Dashed line corresponds to small particles ($b < d < \xi$), dash-dotted line corresponds to intermediate size particles ($\xi < d < a$), and solid line corresponds to large particles ($d > a$). Here $N_\xi \simeq (\xi/b)^{1/\nu}$ is the number of monomers in a correlation volume (see eq. 7.33), $N_d \simeq N_\xi (d/\xi)^2$ is the number of monomers in a chain section on the order of intermediate particle size (see eq. 7.35), and N_e is the number of monomers per entanglement strand. Dotted line corresponds to the crossover taking into account the contribution of hopping process to the particle mobility (see discussion in section 7.2.1). Logarithmic scales.

$d < a$) "feel" the viscosity close to that of solvent in dilute polymer solutions with degree of polymerization lower than N_ξ

$$N_\xi \simeq (\xi/b)^{1/\nu} \simeq \begin{cases} (\xi/b)^2, & \text{theta} \\ (\xi/b)^{1.76}, & \text{athermal} \end{cases} \tag{7.33}$$

The semidilute solution viscosity η increases above the solvent viscosity η_s linearly with degree of polymerization N: $\eta \simeq \eta_s (N/N_\xi)$. Intermediate size particles that are larger than polymers "feel" bulk solution viscosity η with terminal particle diffusion coefficient inversely proportional to the degree of polymerization N

$$D_t(N) \simeq \frac{k_B T}{\eta_s d (N/N_\xi)}, \quad \text{for } N_\xi < N < N_d \tag{7.34}$$

where N_d corresponds to the degree of polymerization at which the size of polymers is comparable to the particle size d

$$N_d \simeq N_\xi (d/\xi)^2 \tag{7.35}$$

Terminal diffusion coefficient of intermediate size particles that are smaller than polymers is independent on the degree of polymerization in solutions with $N > N_d$ (see eq. 7.13)

$$D_t(N) \simeq \frac{k_B T}{\eta_s d \left(N_d/N_\xi\right)} \simeq \frac{k_B T \xi^2}{\eta_s d^3}, \quad \text{for } N > N_d \tag{7.36}$$

The diffusion coefficient of large particles ($d > a$) is predicted to have similar molecular weight dependencies as that of intermediate size particles in dilute and in unentangled semidilute (see eq. 7.34) solutions. In entangled solutions large particles "feel" bulk solution viscosity at times longer than solution relaxation time (see solid line in Figure 7.7). The terminal particle diffusion coefficient is reciprocally proportional to the solution viscosity η and decreases with increasing degree of polymerization N as

$$D_t(N) \simeq \frac{k_B T}{\eta d} \sim N^{-3}, \quad \text{for } N > N_e \tag{7.37}$$

The scaling exponent is expected to be even stronger with value of 3.4 if one takes into account tube length fluctuation [60, 188].
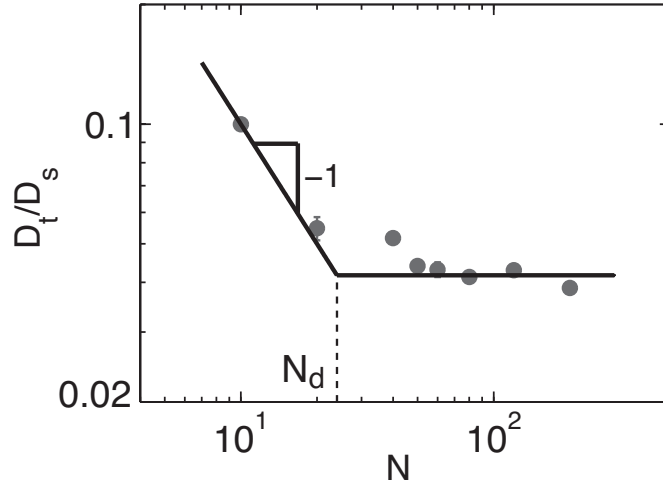
Figure 7.8: Normalized terminal particle diffusion coefficient D_t/D_s in polymer melt. Solid circles are data from ref. [193] for diffusion of a particle with diameter $d = 6\sigma$ in melts of polymers with degree of polymerization N ranging from 10 (unentangled) to 200 (entangled). Here σ corresponds to Lennard–Jones length [196]. $N_d \simeq 24$ represents the crossover degree of polymerization, below which the particle diffusion coefficient is reciprocally proportional to the degree of polymerization (see eq. 7.34) and above which it is independent of the degree of polymerization (see eq. 7.36). The root-mean-square end-to-end distance of polymer chains with degree of polymerization N_d is $R \simeq \sqrt{6} R_g \simeq 6\sigma$, which is equal to the particle size d.

We compare our predictions for dependence of intermediate particle diffusion coefficient on molecular weight with available molecular dynamics simulation and experimental data. It is predicted that the particle diffusion coefficient $D^{\mathbf{L}}$ is independent of degree of polymerization N in melts and solutions of large ($\mathbf{L}$) polymers with size R larger than particles of size d (see eq. 7.36), whereas particles are expected to "feel" bulk viscosity in melts and solutions of short polymers ($R < d$) (see eq. 7.34). The ratio between diffusion coefficient $D^{\mathbf{S}}$ of intermediate particles through the liquid of shorter ($\mathbf{S}$) polymers with size $R_{\mathbf{S}} < d$ and degree of polymerization $N_{\mathbf{S}}$ and diffusion coefficient $D^{\mathbf{L}}$ of the same particles through the liquid of large polymers of size $R_{\mathbf{L}} > d$ is $D^{\mathbf{S}}/D^{\mathbf{L}} \simeq N_d/N_{\mathbf{S}}$. Here N_d corresponds to the degree of polymerization at which the polymer size is on the order of the particle size. As shown in Figure 7.8, this prediction is verified by the simulation data from ref. [193]. Diffusion coefficient of particles in polymer melts with degree of polymerization below N_d is reciprocally proportional to the degree of polymerization (see eq. 7.34). The diffusion coefficient $D^{\mathbf{L}}$ of intermediate particles in melts with degree of polymerization N above N_d is independent of the degree of polymerization (see eq. 7.36 and horizontal line in Figure 7.8).

Authors of ref. [138] measured the diffusion of gold nanoparticles with diameter $d \simeq 5\,\mathrm{nm}$ in two monodisperse poly(n-butyl methacrylate) (PBMA) melts of molecular weight $2.5\,\mathrm{kDa}$ and $180\,\mathrm{kDa}$. The root-mean-square end-to-end distance R of $2.5\,\mathrm{kDa}$ PBMA chain is approximately $2.5\,\mathrm{nm}$ and the size of $180\,\mathrm{kDa}$ PBMA chain is about $21\,\mathrm{nm}$ as estimated based on data from refs. [138] and [197]. The $5\,\mathrm{nm}$ gold particles are expected to experience bulk viscosity in $2.5\,\mathrm{kDa}$ PBMA melt but in $180\,\mathrm{kDa}$ melt they only "feel" effective viscosity, which is predicted by our model to be the viscosity of the PBMA melt with the chain size on the order of the particle size. It was found that the diffusion coefficient of $5\,\mathrm{nm}$ gold particles in $180\,\mathrm{kDa}$ PBMA melt is about 4 times smaller than that in $2.5\,\mathrm{kDa}$ PBMA melt at the same temperature above glass transition. Therefore, the $5\,\mathrm{nm}$ particles in $180\,\mathrm{kDa}$ PBMA melt probe the viscosity of an effective polymer melt with molecular weight of $10\,\mathrm{kDa}$, which is 4 times higher

than 2.5 kDa but 18 times lower than the actual polymer molecular weight. It turns out that the size of a 10 kDa PBMA chain in melt is about 5 nm, which is on the order of the particle size and thus verifies our prediction.

7.2.4 "Universal" dependence of diffusion coefficient of intermediate size particles
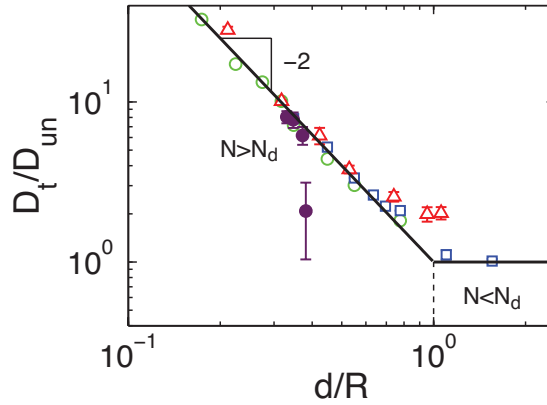
Figure 7.9: Dependence of the ratio of terminal particle diffusion coefficient D_t and "unentangled" diffusion coefficient D_{un} of intermediate size particles (defined by eq. 7.39) on the ratio of particle and polymer sizes d/R in polymer solutions and melts. Empty symbols are molecular dynamics simulation data from ref. [193] and filled circles are experimental data from ref. [136]. Solid line is the prediction of our scaling model (eq. 7.40).

All the dependencies of diffusion coefficient of intermediate size particles described above can be combined into a single "universal" plot. To do that we define viscosity η_{un},

$$\eta_{\mathrm{un}} = \begin{cases} \eta\left(N\right), & \text{for } N < N_e \\ \eta\left(N_e\right) N/N_e, & \text{for } N > N_e \end{cases} \tag{7.38}$$

which is the bulk viscosity η if polymer liquids are unentangled. If polymer liquids are entangled, η_{un} is the extrapolation of bulk viscosity from the unentangled regime, which is linearly proportional to the polymer molecular weight $\eta_{\mathrm{un}} = \eta\left(N_e\right) N/N_e$. One can define D_{un} as the naively expected particle diffusion coefficient in a polymer

liquid with viscosity η_{un} according to classical (Stokes-Einstein) prediction:

$$D_{\text{un}} \simeq \frac{k_B T}{\eta_{\text{un}} d} \qquad (7.39)$$

Dependencies of terminal particle diffusion coefficient D_t on i) particle size d (eq. 7.13), ii) solution concentration c (eq. 7.25), and iii) degree of polymerization N (eqs. 7.34 and 7.36) can be rewritten in terms of the dependence of reduced diffusion coefficient D_t/D_{un} on the ratio d/R of particle and polymer sizes:

$$\frac{D_t}{D_{\text{un}}} \simeq \begin{cases} (d/R)^{-2}, & \text{for } d < R \\ 1, & \text{for } d > R \end{cases} \qquad \text{for } \xi < d < a \qquad (7.40)$$

If the particle is larger than the polymer ($d > R$) its diffusion coefficient D_t is on the order of the classical prediction (eq. 7.40) where D_{un} is the bulk viscosity of unentangled polymer liquid. If the particle is smaller than the polymer ($d < R$), the naively expected diffusion coefficient D_{un} (eq. 7.39) with η_{un}—viscosity of unentangled polymer liquids (or "unentangled" extrapolation (eq. 7.38) for entangled polymer liquids)— underestimates the diffusion coefficient of intermediate size particles D_t by the factor $(d/R)^2$. Below we first outline how the "universal" plot of D_t/D_{un} as a function of d/R can be constructed using data from molecular dynamics simulations and experiments and then compare the resulting "universal" function with our prediction (eq. 7.40).

Authors of ref. [193] reported the terminal diffusion coefficient D_t of particles with size d ranging from σ to 9σ in an unentangled polymer melt with degree of polymerization $N = 60$, where σ is Lennard–Jones length [196]. In order to construct the "universal" plot one needs to know the unentangled viscosity η_{un} and the polymer size R. For the unentangled polymer melt with $N = 60$ the unentangled viscosity η_{un} is equal to the bulk viscosity, which is reported to be $42.5 k_B T/\left(\sigma^3 \tau_{LJ}\right)$ [198], where τ_{LJ} is Lennard–Jones time [196]. The diffusion coefficient D_{un} is calculated using relation $D_{\text{un}} = k_B T/\left(3\pi d_h \eta_{\text{un}}\right)$ [3], where $d_h = d + \sigma$ corresponds to the particle-monomer cross

---

[3]The expression $D_{\text{un}} = k_B T/\left(3\pi d_h \eta_{\text{un}}\right)$ applies for no-slip particle-polymer boundary condition. Slip particle-polymer boundary condition will lead to larger particle diffusion coefficient $D_{\text{un}} = k_B T/\left(2\pi d_h \eta_{\text{un}}\right)$.

diameter[199]. The end-to-end distance R of a linear polymer chain of degree of polymerization $N > 10$ in simulated melts is reported to be $R = 1.22\sigma N^{1/2}$. [200] Based on such information one can obtain the values of D_t/D_{un} and d_h/R and the results are presented by triangles in Figure 7.9.

Similarly one can add to the "universal" plot the simulation data for particles of sizes $d = 2\sigma$ (empty circles in Figure 7.9) and 6σ (empty squares in Figure 7.9) in melts of polymers with degree of polymerization N (from 10 to 200) ranging from unentangled to entangled regime. Within the range of $N \leq 60$ the polymers are unentangled and thus the unentangled viscosity η_{un} is equal to the bulk melt viscosity, which is determined to be linearly proportional to degree of polymerization. [198] For $N > 60$ the extrapolated value of η_{un} from the unentangled regime (eq. 7.39) is used to calculate D_{un}. The values of D_t/D_{un} and d_h/R for these particles of two different sizes are calculated following the same procedure as described above.

The diffusion coefficient of 5 nm gold nanoparticles in solutions of 240 kDa polystyrene in toluene at different concentrations is reported in ref. [136]. In order to add these data to the "universal" plot one can rewrite the unentangled extrapolation particle diffusion coefficient as $D_{\mathrm{un}} = D_s \left(\xi/R_g\right)^2$, where D_s (see eq. 7.7) corresponds to the diffusion coefficient of a probe particle in a pure solvent. Following the described procedure[4], the concentration-dependent particle diffusion coefficients are presented by solid circles in the "universal" plot (see Figure 7.9). Note that all points group together because R_g is a weak function of the solution concentration.

As shown in Figure 7.9, all the data points for diffusion of intermediate size spherical probes in polymer liquids collapse onto a "universal" curve reasonably well. Note that the experimental point at the highest concentration (the largest value of d/R) de-

---

[4]The values of correlation length ξ and polymer size $R_g\left(c\right)$ at different solution concentrations are estimated by expressions $\xi\left(c\right) \simeq R_g\left(c^*\right)\left(c/c^*\right)^{-0.76}$ and $R_g\left(c\right) \simeq R_g\left(c^*\right)\left(c/c^*\right)^{-0.12}$, respectively. Diffusion coefficient of a particle with size on the order of the correlation length ξ in polymer solution, αD_s, is used for calculating $D_{SE} = \alpha D_s\left(\xi/R_g\right)^2$, in which $D_s = 141\mu\mathrm{m}^2/\mathrm{s}$ [136] is the diffusion coefficient of the 5 nm gold nanoparticles in pure solvent and the scaling prefactor α is 0.53 as determined by experimental data (see Figure 7.6).

viates from the trend of other data points, possibly due to the error of measurements because of the degradation of laser focus at such high solution concentration. The "universal" curve suggests two regimes as predicted by our scaling model (eq. 7.40): 1) probe particles "feel" bulk viscosity if their size is larger than the polymer size, 2) particles experience local viscosity of polymer liquids, which is smaller than the unentangled viscosity η_{un} by a factor of $(d/R)^2$, if their size is smaller than the polymer size and the tube diameter.

We conclude that our predictions for the mobility of intermediate size particles in polymer liquids (melts and solutions) agree with available data, but a systematic study covering a wide range of solution concentrations, polymer molecular weight, and particle sizes is needed for more systematic tests of our theory. It should be noted that our scaling calculations of particle diffusion in polymer liquids (melts and solutions) do not take into account hopping (see chapter 8), the adsorption of polymer chains onto particles, and slippage at the particle-polymer interface [201].

7.3 Summary: particle diffusion is determined by polymer dynamics

In this chapter we have developed a scaling theory for the mobility of non-sticky spherical particles in polymer liquids (solutions and melts). There are three different cases for particle diffusion in polymer liquids depending on the relation of particle size d with respect to the correlation length ξ and the tube diameter a.

(i) Small particles. Mobility of small particles ($b < d < \xi$) is not strongly affected by polymers and their diffusion coefficient $D_s \simeq k_B T / (\eta_s d)$ is mainly determined by the solvent viscosity η_s.

(ii) Intermediate size particles. Motion of intermediate size particles ($\xi < d < a$)

is not affected by entanglements. At time scales shorter than the relaxation time τ_ξ of a correlation blob the motion of intermediate size particles is not much affected by polymers and is diffusive with diffusion coefficient mainly determined by solvent viscosity. The intermediate size particles probe modes of surrounding polymers at intermediate time scales $\tau_\xi < t < \tau_d$, where τ_d is the relaxation time of a polymer segment with size comparable to particle size d, and therefore, the particle motion is sub-diffusive with mean-square displacement $\langle \Delta r^2 \rangle \sim t^{1/2}$ (see eq. 7.11). At longer time scales ($t > \tau_d$) the motion of intermediate size particles is diffusive but with diffusion coefficient determined by the effective viscosity $\eta_{\text{eff}} \simeq \eta_s \left(d/\xi \right)^2$ (see eq. 7.14), which is the viscosity of a polymer liquid with polymer size on the order of particle size. The effective viscosity η_{eff} is independent of polymer molecular weight for $R > d$ and is only determined by the particle size and the correlation length of the polymer solution.

(iii) Large particles. Motion of particles with size larger than the entanglement length ($d > a$) at time scales shorter than the relaxation time τ_e of an entanglement strand is similar to that of intermediate size particles. At time scales longer than τ_e the large particles are trapped by entanglements and in order to move further they have to wait for the polymer liquid to relax during reptation time τ_{rep}. Terminal diffusion coefficient of very large particles ($d >> a$) is determined by bulk viscosity η of polymer liquids, which scales with degree of polymerization as $\eta \sim N^{3.4}$. Particles slightly larger than the tube diameter ($d \gtrsim a$) do not have to wait for the whole polymer liquid to relax and can diffuse by hopping between neighboring entanglement cages (see chapter 8).

The results of particle mobility in polymer liquids could be applied to test the local structure and dynamics of complex fluids such as mucus [202, 203]. At the crossovers between different scaling regimes of the size-dependent particle diffusion coefficient (see section 7.2.1), the characteristic length scales in polymer liquids, such as correlation length ξ and entanglement mesh size a, are on the order of the particle size. It should be noted that predictions described in the present work directly apply only to

non-adsorbing particles since the adsorption of polymers on particles will slow down particle motion. For instance, particles without proper protection will stick to the bio-macromolecules in the mucus and diffuse ~ 1000 times slower than non-adsorbing particles of the same size. [202] Given the time-dependent mean-square displacement of probe particles, one can describe the viscoelastic properties of probed complex environments on the length scale comparable to the particle size within a wide frequency range by using the generalized Stokes-Einstein relation. [159] The probe particles can be prepared with sizes ranging from nanometer to micron allowing one to probe the dynamics of complex fluids over this wide range of length scales.

CHAPTER 8

MOBILITY OF PARTICLES IN POLYMER SOLIDS

Polymer chains in polymer solids (gels and networks) are crosslinked via chemical bonds and thus, unlike the chains in polymer liquids, cannot relax no matter how long one waits. The motion of particles in polymer solids is similar to that in polymer liquids (see chapter 7) as long as the particle size is smaller than the network strand size. The reason for this similarity is that the motion of such particles is not much affected by the crosslinks. However, probe particles with size larger than the network mesh size are trapped by the network cages. The only way for a large particle to leave a confinement cage is by hopping—waiting for the fluctuation of an opening (loop) between two neighboring confinement cages that could be large enough to allow the particle to slip through this loop.

In this chapter we analyze the mechanism of hopping diffusion, concentrate on describing how this mechanism contributes to the motion of large particles in polymer solids (networks and gels), and then revisit the effect of hopping to the diffusion of large particles in polymer liquids (melts and solutions). We find that in unentangled polymer solids the motion of particles with size larger than the network mesh size a_x is not affected by the network crosslinks until the relaxation time τ_x of a network strand. At time scales longer than τ_x the large particles cannot move further until a certain time scale, at which the fluctuation of network cages is large enough to allow particles to slip through. This time scale increases as an exponential of a square of the particle size, resulting in the terminal diffusion coefficient of large particles in polymer solids that decreases exponentially with the square of particle size.

The hopping diffusion of large particles of size d in entangled polymer liquids and polymer solids with low density of crosslinks, at which the network mesh size a_x is

larger than the tube diameter ($a_x > d > a$), has similar mechanisms, but different dependence on particle size in comparison with that in unentangled polymer solids. The terminal particle diffusion coefficient due to hopping decreases exponentially with the increase of the particle size, which is weaker than that for the case of polymer solids, due to non-affine deformation of entanglements.

In entangled polymer liquids the motion of large particles with size larger than the tube diameter is contributed by hopping diffusion and chain reptation (see chapter 7). The terminal particle diffusion coefficient is found to be dominated by the hopping diffusion if the particles are not significantly larger than the tube diameter.

The chapter is structured as follows. In section 8.1 we first introduce the concept of hopping diffusion by considering the diffusion of large probe particles in a simple idealized "elementary" polymer network. The idea of hopping diffusion is then extended to unentangled polymer networks and gels in sections 8.2 and 8.3. Hopping diffusion of large particles in entangled polymer solids is discussed in section 8.4. In section 8.5 we revisit the hopping diffusion of large probe particles in entangled polymer liquids by extending the results for particle hopping entangled polymer solids. Discussions and concluding remarks are presented in section 8.5.

8.1   "Elementary" polymer network

Consider the motion of a probe particle of size d in a monodisperse unentangled permanently crosslinked network above glass transition temperature T_g and crystallization transition temperature T_c. Let us denote the number of Kuhn monomers between two neighboring crosslinks by N_x ($< N_e$) and the size of a network strand by a_x. In a typical network there are many network strands overlapping within the volume pervaded by a network strand (see Figure 8.1a). The overlap parameter P_x is defined as the number of network strands within the volume $a_x^3 \simeq (bN_x^{1/2})^3$ pervaded by each network strand. We model this monodisperse network by P_x overlapping "elementary" networks (see

Figure 8.1b). These P_x "elementary" networks overlap with each other (see Figure 8.1) and in the "elementary" network there is only one network strand per volume a_x^3 (similar to de Gennes' c^* gels [187]). Note that these "elementary" networks confine the probe particles in an essentially independent way but the connectivity of them is not specified.
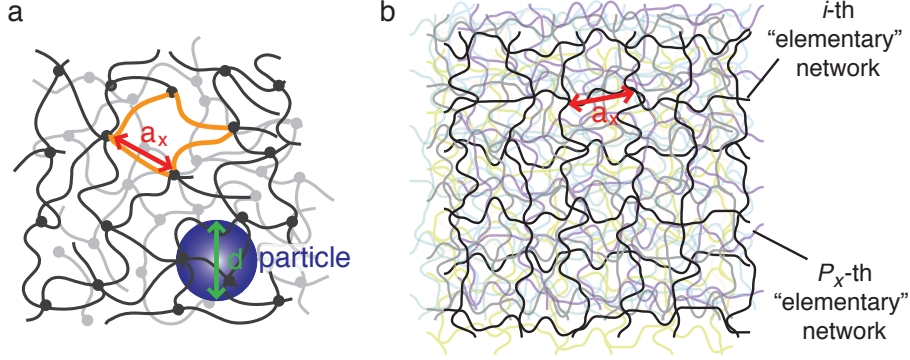
Figure 8.1: An unentangled polymer network is modeled by overlapping "elementary" networks. a) Schematic representation for the diffusion of a particle of size d in an unentangled polymer network with network strand size of a_x. The circles correspond to crosslinks. There are $P_x \simeq N_x^{1/2}$ network strands within the pervaded volume a_x^3 of a network strand. b) The unentangled polymer network is modeled by P_x overlapping "elementary" polymer networks. One of these "elementary" networks is shown by bright black lines while the remaining $P_x - 1$ "elementary" networks are shown by the dimmed color lines. The size of a single mesh (loop) defined as the number of network strands per loop is about $\ln(P_x)$ (see appendix D).

We consider the diffusion of large particles ($d > a_x$) in the idealized "elementary" network. We define the "center" of a cage in an "elementary" network as the geometric center of the probe particle at equilibrium. Initially a large probe particle ($d > a_x$) is confined by the "elementary" network with the particle fluctuating around the "center" of a cage. During a hopping event the large probe particle jumps from the initial network cage to a neighboring one with the hopping step size on the order of the cage size a_x (in fact, the cage size is about $a_x \ln(P_x)$; here and below we drop the logarithmic term to keep out calculation on the scaling level).

In order to hop from one cage to another, the large probe particle has to overcome an entropic energy barrier, which is defined as the difference between the maximum

and the initial elastic deformation energy of surrounding network strands during the hopping. To estimate the energy barrier one would consider the deformation energy of the network induced by the particle motion, and therefore, would take into account the number of network strands d^3/a_x^3 affected by the large probe particle, which is the number of network strands of the "elementary" network within the volume (d^3) occupied by the particle. During a single hopping event, however, not all of the affected network strands have to slip around the particle. In fact, only one network loop slips around the particle and the deformation energy of this network loop determines the entropic barrier that the probe particle has to overcome (see Figure 8.2).
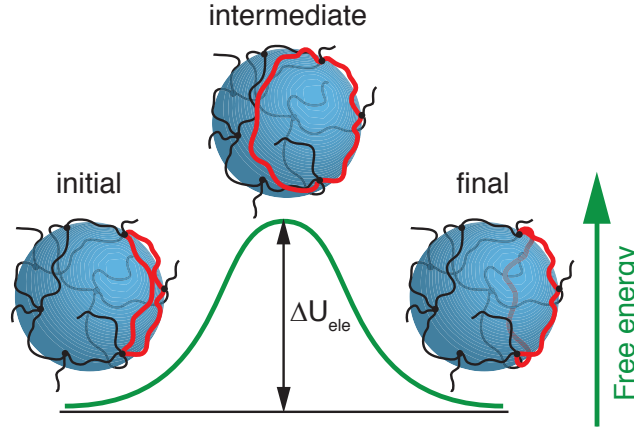
Figure 8.2: Illustration of a large probe particle hops from one network cage to another neighboring one with only one network loop (highlighted by red) slipping around the particle.

The number of network strands n_l is on the order of $\ln(P_x)$ ignoring the numerical coefficients (see appendix D). At the moment the large particle is leaving the initial cage and at the onset of entering the neighboring cage (see intermediate state in Figure 8.2), the free energy due to deformation of the network strand is expected to be maximum. In this case the network loop is stretched from peripheral length $n_l a_x$ to the order of particle size d (in fact, the peripheral length πd of the particle). Therefore, the entropic energy barrier that the particle has to overcome in order to hop from one cage to another is the product of the energy $k_B T \left[(d/n_l)^2 \big/ a_x^2 \right]$ for stretching a network strand from size

a_x to d/n_l and the number of network strands n_l within a network loop:

$$\Delta U_{\text{ele}} \simeq n_l k_B T \frac{(d/n_l)^2}{a_x^2} \tag{8.1}$$

which is on the order of

$$
\begin{aligned}
\Delta U_{\text{ele}} &\simeq k_B T \frac{d^2}{n_l a_x^2} \simeq k_B T \frac{d^2}{a_x^2 \ln (P_x)} \\
&\simeq k_B T \left(d/a_x\right)^2
\end{aligned} \tag{8.2}
$$

Here we drop the logarithmic correction due to the finite loop size since the energy barrier (eq. 8.2) is dominated by the term $\left(d/a_x\right)^2$ (see appendix D).

From this energy barrier (eq. 8.2) one can estimate the waiting time for the hopping diffusion of large probe particles in an "elementary" polymer network.

$$
\begin{aligned}
\tau_w^{\text{ele}} &\simeq \tau_x \exp \left(\Delta U_{\text{ele}}/k_B T\right) \\
&\simeq \tau_x \exp \left(d^2/a_x^2\right)
\end{aligned} \tag{8.3}
$$

in which

$$\tau_x \simeq \tau_0 N_x^2 \tag{8.4}$$

is the relaxation time of a network strand with τ_0 given by eq. 7.6. The physical meaning of τ_x can be understood from its reciprocal $1/\tau_x$, which corresponds to the frequency the particles attempt to go over the barrier.

Recall that the hopping step size for the case of "elementary" network is a_x, the mean-square displacement of a large particle hopping in an "elementary" network is

$$
\begin{aligned}
\left\langle r^2 \left(t\right)\right\rangle_{\text{hop}}^{\text{ele}} &\simeq a_x^2 \frac{t}{\tau_w^{\text{ele}}} \simeq a_x^2 \exp \left(-d^2/a_x^2\right) \frac{t}{\tau_x}, \\
\text{for } t &> \tau_w^{\text{ele}} \text{ and } d > a_x
\end{aligned} \tag{8.5}
$$

with the terminal particle diffusion coefficient

$$D_t^{\text{ele}} \simeq \frac{a_x^2}{\tau_w^{\text{ele}}} \simeq \frac{a_x^2}{\tau_x} \exp \left(-d^2/a_x^2\right) \tag{8.6}$$

Here we briefly summarize the concepts of hopping diffusion introduced by considering the motion of large particles in an "elementary" polymer network. Initially the

particle is confined within a network cage. During a single hopping event, the probe particle leaves its initial cage and enters a neighboring cage with only one network loop slipping around the particle. The hopping step size is on the order of the mesh size a_x of an "elementary" network and the free energy barrier the particle has to overcome is on the order of $k_B T \left(d/a_x \right)^2$.

8.2 Unentangled polymer network

The ideas introduced in 8.1 can be easily extended to the case of diffusion of large particles in unentangled polymer network. The difference is that in an unentangled polymer network there are P_x overlapping "elementary" networks surrounding the particle. Each of these P_x "elementary" networks exerts constraint on the particle independently and tends to localize the particle to its own "center". However, instead of being localized around the "center" of a particular "elementary" network, the particle would be at the position at which the constraints from all the "elementary" networks are balanced.

As illustrated in Figure 8.3, initially the centers (red dots) of P_x "elementary" networks are randomly distributed around the equilibrium position O of the probe particle. At equilibrium the net force exerted by the P_x "elementary" networks on the particle is zero. The restoring force applied to the particle from each "elementary" network is linearly proportional to the deviation of the particle from the "center" of the "elementary network" as the confinement potential is parabolic (see Appendix C). Therefore, we have

$$\sum_{j=1}^{P_x} \vec{r}_j = 0 \tag{8.7}$$

where $\vec{r}_j$ is the distance from the center O of the particle to the center of an "elementary" network j.

The hopping step size for a large probe particle ($d > a_x$) moving through the un-
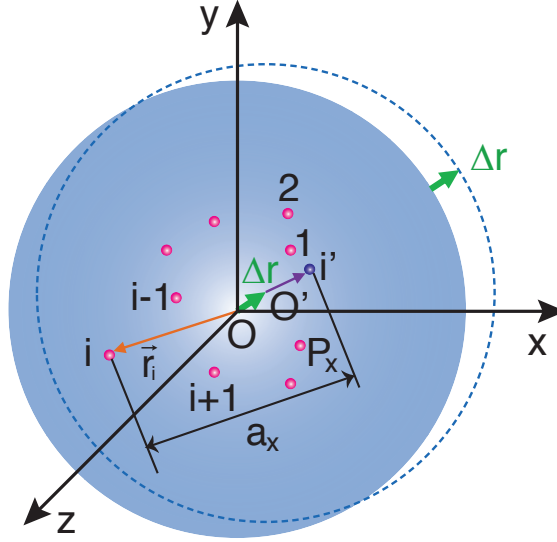
Figure 8.3: Model for estimating the step size for a large probe particle hopping between two neighboring cages in a monodisperse unentangled polymer network. The unentangled polymer network is modeled as P_x overlapping "elementary" networks with their network cage centers $1, 2, \ldots, i, \ldots P_x$ (red dots) randomly distributed around the particle. During a single hopping event the particle leaves its initial equilibrium position O and arrives another neighboring equilibrium position O' with a step size Δr. Meanwhile, the particle leaves the confinement cage of the "elementary" network i with the center that is the furthest from the particle initial equilibrium position O.

entangled network is much smaller than that for an "elementary" network. During a single hopping step the particle moves by a distance $\Delta \vec{r}$ and arrives at a new equilibrium position. As sketched in Figure 8.3, the particle most likely escapes from the cage of an "elementary" network i whose center has the maximum distance from the equilibrium position of the particle as the corresponding energy barrier is the lowest compared with that of other "elementary" networks.[1] The particle enters the neighboring cage i' whose center has a distance $\vec{r}_i + \vec{a}_x - \Delta \vec{r}$ from the center of the new particle position O'. The distance from the centers of the rest $P_x - 1$ "elementary" networks to the new equilibrium position O' of the particle is changed by $\Delta \vec{r}$ (see Figure 8.3). Since at this new equilibrium position the net force exerted on the particle by the P_x "elementary"

---

[1]Note that here we are assuming that the confinement cages are uniform, i.e., all entropic barriers for hopping diffusion are the same. In reality the barriers have distributions that make the problem more complex. For simplicity we do not take into account effect from the polydispersity of confinement cages.

networks is still zero, one obtains

$$\sum_{j=1,j\neq i}^{P_x} (\vec{r}_j - \Delta\vec{r}) + (\vec{r}_i + \vec{a}_x - \Delta\vec{r}) = 0 \qquad (8.8)$$

Using eq. 8.7 the above equation can be rewritten as $\sum_{j=1}^{P_x} \Delta\vec{r} = \vec{a}_x$, which gives the magnitude of the step size of particle hopping for a dry network

$$\Delta r \simeq a_x/P_x \simeq b \qquad (8.9)$$

which is P_x times smaller than the hopping step size in an "elementary" network.

The energy barrier for a large particle hopping between neighboring network cages in an unentangled network, however, is the same as that in an "elementary" network. This is because that only one network loop slips around the probe particle when it jumps from one cage to the neighboring one. The energy barrier for particle hopping through an unentangled polymer network is (see eq. 8.2):

$$\Delta U_{\text{net}} \simeq \Delta U_s \simeq k_B T \left(d/a_x\right)^2 \qquad (8.10)$$

From the energy barrier (eq. 8.10) one can obtain the waiting time for large particles hopping in unentangled polymer network,

$$\begin{aligned} \tau_w^{\text{net}} &\simeq \tau_x \exp\left(\Delta U_{\text{net}}/k_B T\right) \\ &\simeq \tau_x \exp\left(d^2/a_x^2\right) \end{aligned} \qquad (8.11)$$

at which the large particle makes a successful hop leaving the initial confinement cage and entering neighboring one.

The MSD for a large particle hopping in dry unentangled polymer networks is proportional to the number of steps the particle makes during a certain period of time

$$\begin{aligned} \left\langle r^2\left(t\right)\right\rangle_{\text{hop}}^{\text{net}} &\simeq b^2 \frac{t}{\tau_w^{\text{net}}} \simeq b^2 \exp\left(-d^2/a_x^2\right) \frac{t}{\tau_x}, \\ \text{for } t &> \tau_w^{\text{net}} \text{ and } d > a_x \end{aligned} \qquad (8.12)$$

and the particle diffusion coefficient due to hopping is

$$D_{\text{hop}}^{\text{net}} \simeq \left(b^2/\tau_x\right) \exp\left(-d^2/a_x^2\right) \qquad (8.13)$$

For a relatively large particle the hopping diffusion is extremely slow as the mean-square displacement of particles decreases exponentially with the increase of particle size. For instance, reduced diffusion coefficient $D_{\text{hop}}^{\text{net}} \tau_x / b^2$ of a particle with size d about two times of the mesh size ($d = 2a_x$) is on the order of 10^{-2}.

The hopping diffusion occurs on time scales longer than the waiting time τ_w^{net} (eq. 8.11). On shorter time scales the particle is fluctuating within the network cage without leaving it. Specifically, the motion of the large probe particle ($d > a_x$) is unaffected by network crosslinks at time scales shorter than the relaxation time τ_x of a network strand between two neighboring crosslinks. The motion of large probe particle is sub-diffusive with mean-square displacement proportional to the $1/2$ power of time t as it probes segmental dynamics of network strands (see eq. 7.11 and section 7.1.3):

$$\left\langle r^2 \left(t \right) \right\rangle \simeq \frac{b^3}{d} \left(\frac{t}{\tau_0} \right)^{1/2}, \quad \text{for } \tau_0 < t < \tau_x \tag{8.14}$$

in which τ_x corresponds to the relaxation time of a network strand (see eq. 8.4).

Note that at time scale τ_x, the MSD of a large probe particle due to the polymer dynamics is about $a_x^2 b/d$, which is larger than the MSD b^2 of the large probe particle at time scale τ_w^{net} due to hopping (see eq. 8.12). We would like to stress out that the particle motion is due to the superposition of the two processes: hopping between neighboring network cages (eq. 8.12) and fluctuation around the centers of network cages but without leaving them (eq. 8.14). In the following we will discuss this feature in more detail.

8.3 Unentangled polymer gel

In above (section 8.2) we have discussed the hopping diffusion of large particles in unentangled dry polymer network without solvent. By introducing solvent the dry network swells and becomes a gel, but keeping the topological structure of original dry network. A gel could also be prepared via crosslinking polymer chains in a solution.

It is expected that the properties of a gel depends on the preparation condition (see chapter 7 in ref. [60]). To keep our calculation simple we limit our consideration in the following to particle diffusion in gels at the same preparation.
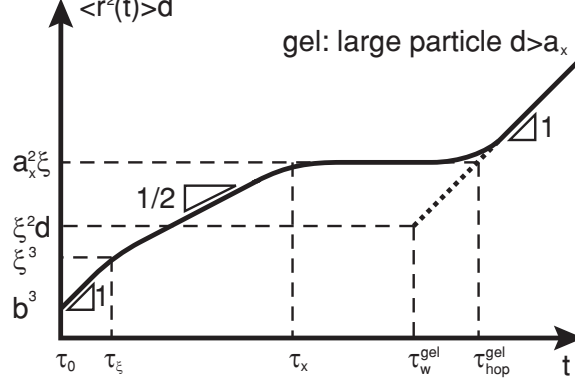
Figure 8.4: Time dependence of the product of mean-square displacement $\langle \Delta r^2(t) \rangle$ and the particle size d for large particles ($d > a_x$) in unentangled polymer gels. The motion of the large particles is not affected by network cages at short time scales: at very short time scales ($\tau_0 < t < \tau_\xi$) the particle motion is diffusive and it experiences mainly solvent viscosity; at intermediate time scales ($\tau_\xi < t < \tau_x$) the particle motion becomes sub-diffusive as the particles probe the segmental dynamics of surrounding polymer chains. At time scales longer than τ_x the large particles are trapped by network cages. They can only leave the initial confinement cages by waiting for the fluctuations of the surrounding network cages that will be large enough to allow them slip through. This hopping diffusion starts at time scale τ_w^{gel}, but becomes experimentally observable only on time scale $\tau_{\text{hop}}^{\text{gel}}$ (see eq. 8.18), at which the particle mean-square displacement due to hopping becomes comparable to the mean-square displacement due to fluctuation of the particle within a network cage at time scale τ_x. Logarithmic scales.

An unentangled polymer gel can be treated as an "effective" unentangled dry polymer network in which the "effective" monomers are correlation blobs. Therefore, the results of particle hopping in dry polymer networks can be readily applied to polymer gels with hopping step size b replaced by the correlation length ξ and other parameters replaced by concentration dependent ones:

$$\left\langle r^2(t) \right\rangle_{\text{hop}}^{\text{gel}} \simeq \xi^2 \left(t / \tau_w^{\text{gel}} \right) \simeq \xi^2 \exp\left(-d^2/a_x^2 \right) \frac{t}{\tau_x}, \qquad (8.15)$$
$$\text{for } t > \tau_w^{\text{gel}} \text{ and } d > a_x$$

Here τ_w^{gel} is the waiting time for particle hopping in an unentangled polymer gel and has the same expression as τ_w^{net} (eq. 8.11) but with a_x and τ_x replaced by the concentration

dependent ones (chapter 9 in ref. [60]):

$$a_x \simeq bN_x^{1/2}\phi^{-(2v-1)/(6v-2)}$$

$$\simeq \begin{cases} bN_x^{1/2}, & \text{theta} \\ bN_x^{1/2}\phi^{-0.12}, & \text{athermal} \end{cases} \tag{8.16}$$

$$\tau_x \simeq \tau_0 N_x^2 \phi^{(2-3v)/(3v-1)}$$

$$\simeq \tau_0 N_x^2 \begin{cases} \phi, & \text{theta} \\ \phi^{0.31}, & \text{athermal} \end{cases} \tag{8.17}$$

The contribution to the mean-square displacement of large particles due to hopping becomes important at a certain time scale $\tau_{\text{hop}}^{\text{gel}}$, at which $\langle r^2 \rangle_{\text{hop}}^{\text{gel}}$ is comparable to the plateau value $\xi a_x^2/d$ (see dotted line in Figure 8.4), which gives

$$\tau_{\text{hop}}^{\text{gel}} \simeq \tau_x \frac{a_x^2}{\xi d} \exp\left(d^2/a_x^2\right) \tag{8.18}$$

Here ξ is the correlation length (eq. 7.1). Taking into account the fact that the probe particles have already moved with a distance $\xi a_x^2/d$ at time scale τ_x, mean-square displacement of particle at time scales longer than τ_x is

$$\langle r^2(t) \rangle \simeq \left(\xi a_x^2/d\right)\left(1 + t \left/ \tau_{\text{hop}}^{\text{gel}}\right.\right),$$

$$\text{for } t > \tau_x \tag{8.19}$$

and the corresponding terminal particle diffusion coefficient is

$$D_t = D_{\text{hop}}^{\text{gel}} \simeq \left(\xi^2/\tau_x\right) \exp\left(-d^2/a_x^2\right) \tag{8.20}$$

Terminal diffusion coefficient of large probe particles ($d > a_x$) in unentangled polymer gels exhibits an exponential dependence on the square of particle (network strand) size (see eq. 8.20). The terminal diffusion coefficient is small, however, still experimentally appreciable for particles with size slightly larger than the network strand size. For instance, the terminal diffusion coefficient of a particle with size $d \simeq 30$ nm is on the order of 10^3 μm^2/s in a polymer gel with $\tau_x \simeq 10^{-9}$ ns, $\xi \simeq 5$ nm, and $a_x \simeq 20$ nm.

Recall the expressions of relaxation time τ_x (eq. 8.17), network strand size a_x (eq. 8.16), as well as the correlation length ξ (eq. 7.1), one can rewrite eq. 8.20 in terms of concentration:

$$
\begin{aligned}
D_t &\simeq \left(\xi^2/\tau_x\right) \exp\left(-d^2/a_x^2\right) \\
&\simeq \frac{b^2}{\tau_0 N_x^2} \exp\left(-\frac{d^2}{b^2 N_x}\phi^{(2v-1)/(3v-1)}\right) \phi^{(v-2)/(3v-1)} \\
&\simeq \frac{b^2}{\tau_0 N_x^2}
\begin{cases}
\exp\left(-\frac{d^2}{b^2 N_x}\right) \phi^{-3}, & \text{theta} \\
\exp\left(-\frac{d^2}{b^2 N_x}\phi^{1/4}\right) \phi^{-7/4}, & \text{athermal}
\end{cases}
\end{aligned}
\tag{8.21}
$$

The terminal particle diffusion coefficient decreases with the concentration by a simple power law $D_t \sim \phi^{-3}$ in a theta solvent, whereas it has more complicated concentration dependence in an athermal or good solvent. Note that the premise in above calculation is that the concentration is above the value that corresponds to the maximum swelling ratio of a gel.

Note that mean-square displacement of probe particles due to dynamics of surrounding network strands at time scales shorter than $\tau_{\text{hop}}^{\text{gel}}$ represents only the fluctuation of probe particles around the center of network cage but without leaving the cage. At time scales shorter than τ_x the particle motion is not yet affected the network cages. At longer time scales the particles are confined within the network cages, but still fluctuating. As depicted by the plateau in Figure 8.4 the magnitude of this deviation is about $\xi a_x^2/d$ at time scale τ_x and does not increase until time scale $\tau_{\text{hop}}^{\text{gel}}$. At time scales longer than $\tau_{\text{hop}}^{\text{gel}}$ mean-square displacement of large particles is determined by hopping diffusion.

8.4   Entangled polymer solids (networks and gels)

In entangled polymer solids there exists both permanent crosslinks and entanglements. In addition to the correlation length ξ and network strand size a_x, therefore, there is an additional important length scale–entanglement size (tube diameter) a. The

size a_x of a network strand could be either smaller or larger than the entanglement mesh size a depending on the density of crosslinks, shown in Figure 8.5. We therefore identify two cases for entangled polymer solids: 1) high density of crosslinks, in which the network strand size a_x is smaller than the entangled mesh size a. The motion of particles in entangled polymer solids is expected to show features that for both entangled polymer liquids and unentangled polymer solids; 2) low density of crosslinks, in which the network strand size a_x is larger than the entangled mesh size a.
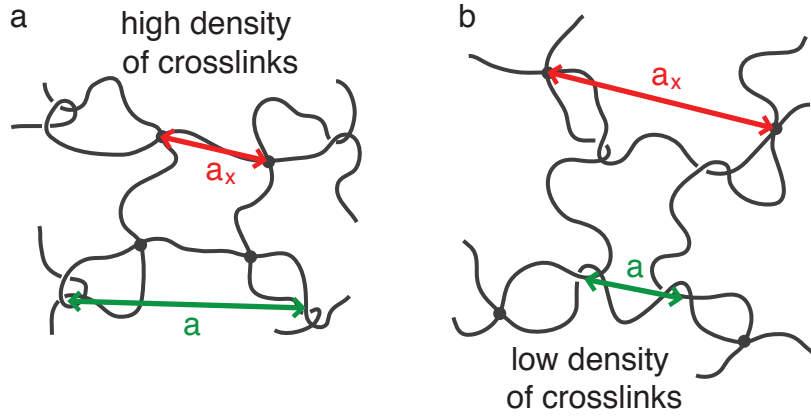
Figure 8.5: Schematic description of entangled polymer solids. a) The size a_x of a network strand is smaller than the entanglement mesh size a if the density of crosslinks is high; b) The network strand size a_x is larger than the entanglement mesh size a if the density of crosslinks is low.

8.4.1   High density of crosslinks

In entangled polymer solids with high density of crosslinks the network strand size a_x is smaller than the entanglement length ($\xi < a_x < a$). Properties of such entangled polymer networks is controlled by the permanent crosslinks, and therefore, these networks are also called unentangled networks. The mobility of particles in unentangled polymer networks has already been discussed in sections 8.2 and 8.2 and below we only briefly state the main results.

The mobility of particles with size d smaller than the network strand size a_x, i.e.,

$d < a_x < a$, is not affected by neither networks nor entanglements. Therefore, the motion of such small particles is the same as they are in polymer liquids (see sections 7.1.1 and 7.1.2).

Mobility of particles with size larger than the network mesh size a_x but smaller than the entanglement length a ($a_x < d < a$) is affected by the crosslinked networks but not the entanglements at long time scales. At time scales shorter than the relaxation time τ_x of a network strand, however, the motion of the particles is not yet affected by the crosslinked networks and is similar to intermediate size particles in polymer liquids (see section 7.1.2). At time scales longer than τ_x, particles shall "feel" the confinement from surrounding network cages and the only way they can move further is via hopping. The hopping diffusion of such large particles ($a_x < d < a$) is the same as if they are in unentangled polymer solids (see section 8.2 and 8.3) as the particle motion is not affected by the entanglements.

Very large particles with size larger than the network mesh size ($d > a > a_x$) are expected to be confined within the local cages at long time scales.

8.4.2   Low density of crosslinks

Consider entangled polymer solids with low density of permanent crosslinks, in which the entanglement mesh size a is smaller than the network mesh size a_x ($a_x > a$). Particles with size smaller than a are not affected by neither entanglements nor networks and their mean-square displacement has the same time dependence as they are in polymer liquids (see sections 7.1.1 and 7.1.2).

Motion of particles with size d larger than a but smaller than a_x ($a < d < a_x$) will be affected by entanglements but not networks at long time scales. However, at time scales shorter than the relaxation time τ_e of an entanglement strand, the particles are not yet affected by entanglements. The particle motion is sub-diffusive with mean-square

displacement proportional to the square root of time as the particles probe segmental dynamics of surrounding polymers (see eq. 7.11 and section 7.1.3). At time scales longer than τ_e the particles are confined by entanglement cages. The only way they can move further is by hopping, because the whole polymer chains cannot relax via reptation due to the existence of permanent crosslinks.

The hopping diffusion of such large particles in entangled polymer solids can be readily obtained by using the results of hopping diffusion of particles with size d larger than the network mesh size a_x in unentangled polymer solids (see section 8.2). The difference between entanglements and crosslinked network cages is that the tube diameter (size of an entanglement strand) changes when subjected to deformation. Upon deformation by a factor λ the tube diameter becomes [60, 204]

$$a' \simeq a\lambda^{1/2} \tag{8.22}$$

which represents the softening of confining potential due to the increase in the distance between entangled polymers [204]. The elongation factor λ is on the order of the ratio between the particle size and the tube diameter in undeformed state: $\lambda = d/a$. Therefore, the energy barrier for the probe particle to hop between entanglement cages is lower by a factor λ as compared to that for crosslinked network cages providing that the entanglement strand size a is the same as the network strand size a_x (see eq. 8.10)

$$\Delta U_{\text{entg}} \simeq k_B T \left(d/a' \right)^2 \simeq k_B T d/a \tag{8.23}$$

The waiting time for the particle to hop between neighboring entanglement cages is

$$\tau_w^{\text{entg}} \simeq \tau_e \exp\left(d/a \right) \tag{8.24}$$

which strongly depends on the relative size of the particle d with respect to the size of an entanglement strand a, but with a relatively weaker manner compared with that for unentangled polymer solids (see eq. 8.11). This is because of the lower deformation energy of entanglement strands (see eq. 8.23) in comparison to unentangled polymer networks and gels (see eq. 8.11). For instance, for a large particle with size d twice

of the entanglement strand (network mesh) size a (a_x) the ratio of two waiting times $\tau_w^{\text{entg}}/\tau_w^{\text{gel}} \simeq \exp\left(2 - 2^2\right) \simeq 10^{-1}$. In eq. 8.24 τ_e corresponds to the relaxation time of an entanglement strand in polymer liquids.

$$\tau_e \simeq \tau_0\,(\xi/b)^3\,(a/\xi)^4 \simeq \tau_0\frac{a^4}{\xi b^3} \tag{8.25}$$
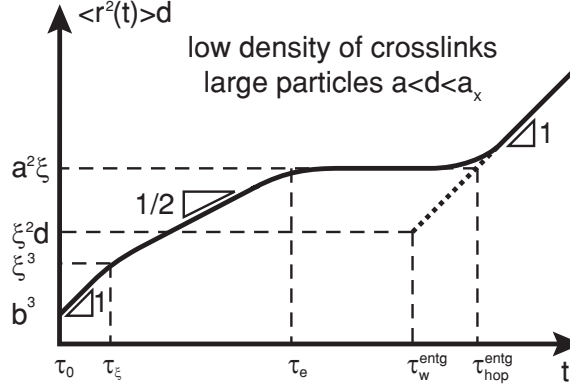
Figure 8.6: Time dependence of the product of mean-square displacement $\langle \Delta r^2(t)\rangle$ and the particle size d for large particles in entangled polymer solids with low density of crosslinks ($a_x > d > a$). The motion of the large particles is not affected by entanglement cages at time scales shorter than the relaxation time τ_e (see eq. 8.25) of an entanglement strand. At time scales longer than τ_e the particles are trapped by entanglement cages; they cannot move until time scale τ_w^{entg} (see eq. 8.24), at which the particles start to hop between neighboring entanglement cages. The hopping diffusion becomes experimentally observable on time scale $\tau_{\text{hop}}^{\text{entg}}$ (see eq. 8.28), at which the particle mean-square displacement due to hopping becomes comparable to the mean-square displacement due to fluctuation of the particle within an entanglement cage at time scale τ_e. Logarithmic scales.

Mean-square displacement of a large probe particles ($a < d < a_x$) due to hopping is proportional to the number of hops the particle makes within a certain time period t

$$
\begin{aligned}
\left\langle r^2\left(t\right)\right\rangle_{\text{hop}}^{\text{entg}} &\simeq \xi^2 t\,/\tau_w^{\text{entg}} \\
&\simeq \xi^2\exp\left(-d\,/a\right)\frac{t}{\tau_e}, \\
\text{for } t &> \tau_w^{\text{entg}} \text{ and } a < d < a_x
\end{aligned}
\tag{8.26}
$$

which is independent of molecular weight of a network strand as long as $a < d < a_x$ but determined by the relative size of the particles with respect to the entanglement mesh size a. Diffusion coefficient the large probe particles in entangled polymer solids

is

$$D_{\text{hop}}^{\text{entg}} \simeq \left(\xi^2/\tau_e \right) \exp\left(-d/a \right) \tag{8.27}$$

The contribution to the particle mean-square displacement from hopping ($\langle r^2\left(t\right)\rangle_{\text{hop}}^{\text{entg}}$) becomes important at certain time scale $\tau_{\text{hop}}^{\text{entg}}$, at which $\langle r^2\left(t\right)\rangle_{\text{hop}}^{\text{entg}}$ is comparable to $\xi a^2/d$ due to polymer dynamics, which gives

$$\tau_{\text{hop}}^{\text{entg}} \simeq \tau_e \left(a^2/\xi d \right) \exp\left(d/a \right) \tag{8.28}$$

Taking into account the fact that the probe particles have already moved with a distance $\xi a^2/d$ at time scale τ_e, mean-square displacement of particles at time scale longer than τ_e is

$$\begin{aligned} \langle r^2\left(t\right)\rangle^{\text{entg}} &\simeq \left(\xi a^2/d \right)\left(1 + t/\tau_{\text{hop}}^{\text{entg}} \right), \\ &\text{for } t > \tau_e \text{ and } a < d < a_x \end{aligned} \tag{8.29}$$

Mobility of very large particles with size d greater than the network mesh size a_x ($d > a_x > a$) is not affected by entanglements and network cages at time scales shorter than the relaxation time τ_e of an entanglement strand. At time scales shorter than τ_e, the particle motion is sub-diffusive with mean-square displacement proportional to the square root of time as the particles probe segmental dynamics of surrounding polymers (see eq. 7.11 and section 7.1.3). At time scales longer than τ_e, one would think that such very large particles "feel" the confinement from entanglement cages, and therefore, they can still jump between neighboring entanglement cages via a similar hopping mechanism discussed for large particles ($a_x > d > a$). In fact, the confinement from entanglements is not important since the local entanglements that surround the particle do not "exist" anymore. This is because the local entanglements are under large deformation due to the existence of the extremely large particles ($d > a_x$), leading to the slippage of entanglement crosslinks towards to the permanent crosslinks [204]. Therefore, the hopping diffusion of very large particles in entangled polymer solids with low density of crosslinks ($d > a_x > a$) is controlled by the permanent networks and similar to large particles in unentangled polymer solids (see sections 8.2 and 8.3).

8.5 Hopping diffusion in entangled polymer liquids

The motion of large particles ($d > a$) in entangled polymer liquids is not affected by the entanglements at time scales shorter than the relaxation time τ_e of an entanglement strand (see Figure 8.7a and chapter 7). At time scales longer than τ_e the large particles will be trapped by entanglement cages and they cannot move further until a time scale τ_{liquids}. Mean-square displacement of large particles at longer time scales is contributed from the particle motion due to chain reptation process and hopping mechanism. Therefore, physical meaning of the time scale τ_{liquids} is determined by the two processes that could lead to the particle motion at long time scales. The motion of large particles in entangled polymer liquids due to chain reptation process has been discussed in section 7.1.3. In section 8.4.1 we have discussed the mechanism of hopping diffusion of large particles in entangled polymer solids with low density of crosslinks ($a < d < a_x$). The results there can be readily applied to describe the hopping diffusion of large particles with size d larger than the entanglement strand size a (eq. 7.2) in entangled polymer liquids (melts and solutions). In the following we first focus on the mean-square displacement of large particles in entangled polymer liquids due to hopping mechanism, and then compare it with the MSD due to the chain reptation process.

8.5.1 Mean-square displacement

The waiting time τ_w^{liquids} for a large particle hopping in entangled polymer liquids is the same as τ_w^{entg} (see eq. 8.24) for the case of entangled polymer solids with low density of crosslinks. Mean-square displacement of a large probe particle due to hopping in entangled polymer liquids at time scales longer than the waiting time τ_w^{liquids} is
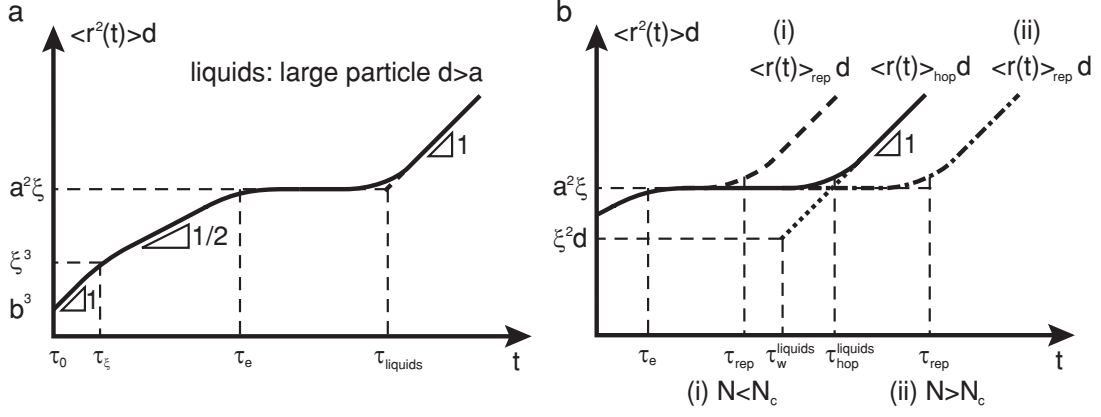
Figure 8.7: Time dependence of mean-square displacement of large particles $(d > a)$ in entangled polymer liquids. $a)$ The motion of large probe particles at time scales shorter than τ_e is not affected by entanglement[190]; at time scales longer than τ_e the large probe particles are trapped by entanglement mesh and they can only move further at time scales longer than τ_{liquids}, which is determined by the interplay between hopping diffusion and chain reptation process. $b)$ Different cases at which τ_{liquids} is determined by: (i) hopping process with $\tau_{\text{liquids}} \simeq \tau_{\text{hop}}^{\text{liquids}}$ if $d < d_c$ or $N > N_c$; (ii) chain reptation process with $\tau_{\text{liquids}} \simeq \tau_{\text{rep}}$ if $d > d_c$ or $N < N_c$. Logarithmic scales.

proportional to the number of hopping steps

$$
\begin{aligned}
\left\langle r^2\left(t\right)\right\rangle_{\text{hop}}^{\text{liquids}} &\simeq \xi^2 t \big/ \tau_w^{\text{liquids}} \\
&\simeq \xi^2 \exp\left(-d/a\right)\frac{t}{\tau_e},
\end{aligned}
\tag{8.30}
$$
$$
\text{for } t > \tau_w^{\text{liquids}} = \tau_w^{\text{entg}} \text{ and } d > a
$$

The mean-square displacement of particles due to hopping is independent of molecular weight but determined by the relative size of particles with respect to the entanglement mesh size a. Diffusion coefficients of a large probe particle in entangled polymer liquids due to hopping is

$$
D_{\text{hop}}^{\text{liquids}} \simeq \left(\xi^2/\tau_e\right)\exp\left(-d/a\right)
\tag{8.31}
$$

It is important to point out that above estimate (eqs. 8.30 and 8.31) does not apply for extremely large probe particles $(d > a^2/\xi)$, which requires the stretching of correlation blobs of size ξ. Here we focus our attention on probe particles slightly larger than entanglement strand size a and try to understand how the hopping contributes to the particle motion.

102

As illustrated by the dotted line in Figure 8.7*b*, the contribution to the particle mean-square displacement $\langle r^2(t) \rangle_{\text{hop}}$ from hopping becomes important at certain time scale $\tau_{\text{hop}}^{\text{liquids}}$, at which $\langle r^2(t) \rangle_{\text{hop}}$ is comparable to $\xi a^2/d$ due to polymer dynamics, which gives

$$\tau_{\text{hop}}^{\text{liquids}} \simeq \tau_e \left(a^2/\xi d \right) \exp\left(d/a \right) \tag{8.32}$$

Taking into account the fact that the probe particles already have mean-square displacement (MSD) $\xi a^2/d$ at time scale τ_e, their MSD at time scales longer than τ_e is

$$\begin{aligned} \langle r^2(t) \rangle_{\text{hop}}^{\text{liquids}} &\simeq \left(\xi a^2/d \right) \left(1 + t \left/ \tau_{\text{hop}}^{\text{liquids}} \right. \right), \\ &\text{for } t > \tau_e \end{aligned} \tag{8.33}$$

Note that eq. 8.33 includes only the contribution from hopping diffusion. Another process that could lead to the particle motion at time scales longer than τ_e is the chain reptation process (see chapter 7). It suggests that the large probe particle can also move further by waiting for the whole polymer system to relax at reptation time scale τ_{rep} (see eq. 7.18)

$$\tau_{\text{rep}} \simeq \tau_e (N/N_e)^3 \tag{8.34}$$

which increases as cube of degree of polymerization N. Mean-square displacement of the large particles due to chain reptation process is (refer to eq. 7.20)

$$\begin{aligned} \langle \Delta r^2(t) \rangle_{\text{rep}}^{\text{liquids}} &\simeq \left(\xi a^2/d \right) t/\tau_{\text{rep}} \\ &\simeq \frac{k_B T}{\eta d} t, \quad \text{for } t > \tau_{\text{rep}} \end{aligned} \tag{8.35}$$

in which η is the bulk viscosity of the entangled polymer liquids. Assuming no coupling between the two processes (chain reptation and hopping diffusion) the net mean-square displacement of the large probe particle in entangled polymer liquids can be written as a sum of contributions from both processes

$$\begin{aligned} \langle \Delta r^2(t) \rangle &\simeq \langle \Delta r^2(t) \rangle_{\text{rep}} + \langle \Delta r^2(t) \rangle_{\text{hop}}^{\text{liquids}} \\ &\simeq \left(\xi a^2/d \right) \left(1 + t \left/ \tau_{\text{hop}}^{\text{liquids}} + t/\tau_{\text{rep}} \right. \right), \\ &\text{for } t > \tau_e \end{aligned} \tag{8.36}$$

The corresponding particle terminal diffusion coefficient is

$$D_t \simeq \left(\xi a^2/d\right) \left(1 \Big/ \tau_{\text{hop}}^{\text{liquids}} + 1/\tau_{\text{rep}}\right) \tag{8.37}$$

The fastest process dominates the particle motion. As the reptation time increases with a power law of the degree of polymerization (eq. 8.34), at a certain crossover value N_c the reptation time τ_{rep} is comparable to $\tau_{\text{hop}}^{\text{liquids}}$.

$$N_c \simeq N_e \left[\left(\frac{a^2}{\xi d}\right) \exp\left(\frac{d}{a}\right)\right]^{1/3} \tag{8.38}$$

For polymer liquids with degree of polymerization larger than N_c, mean-square displacement of the large probe particle is dominated by hopping diffusion (see solid line in Figure 8.7b) and $\tau_{\text{liquids}} \simeq \tau_{\text{hop}}^{\text{liquids}}$ (Figure 8.7a). Mobility of probe particles in polymer liquids of shorter polymers ($N < N_c$) is dominated by chain reptation process (see the dashed line in Figure 8.7b) and $\tau_{\text{liquids}} \simeq \tau_{\text{rep}}$. Note that the reptation time τ_{rep} is independent of particle size, whereas the time scale $\tau_{\text{hop}}^{\text{liquids}}$ increases exponentially with particle size d (see eq. 8.32). Therefore, for a polymer solution with fixed polymer size N and concentration we can introduce a crossover particle size d_c,

$$\begin{aligned} d_c &\simeq a\left[3\ln\left(N/N_e\right) - \ln\left(a^2/\left(d_c\xi\right)\right)\right] \\ &\simeq a\left[3\ln\left(N/N_e\right) - \ln\left(a/\xi\right)\right] \end{aligned} \tag{8.39}$$

at which the time scale $\tau_{\text{hop}}^{\text{liquids}}$ is comparable to the reptation time τ_{rep}. For particles with size smaller than d_c ($a < d < d_c$) the contribution of hopping diffusion dominates the particle mobility ($\tau_{\text{liquids}} \simeq \tau_{\text{hop}}^{\text{liquids}}$, Figure 8.7$a$), whereas for larger particles ($d > d_c$) the hopping contribution is not important ($\tau_{\text{liquids}} \simeq \tau_{\text{rep}}$, Figure 8.7$a$).

8.5.2 Diffusion coefficient

The contribution of hopping diffusion adds small corrections to the terminal diffusion coefficient of large particles ($d > a$) in entangled polymer liquids (see eq. 8.37). We here describe the dependence of terminal particle diffusion coefficient on particle size, solution concentration, and degree of polymerization (polymer molecular weight).

Dependence of particle diffusion coefficient on particle size

Consider an entangled polymer liquids with fixed polymer molecular weight and concentration. There is a small window ($a < d < d_c$) in which the terminal particle diffusion coefficient is controlled by the contribution from hopping diffusion, whereas for particles with size d larger than d_c (see eq. 8.39) it is dominated by the contribution from chain reptation process.

$$D_t\left(d\right) \simeq \begin{cases} \xi a^2 \left/ \left(d\tau_{\mathrm{hop}}^{\mathrm{liquids}}\right)\right. \simeq \left(\xi^2/\tau_e\right)\exp\left(-d/a\right), & \text{for } a < d < d_c \\ \xi a^2 \left/ \left(d\tau_{\mathrm{rep}}\right)\right. \simeq k_B T / \left(\eta d\right), & \text{for } d > d_c \end{cases} \quad (8.40)$$

For the case of $a < d < d_c$ the terminal particle diffusion coefficient is independent of molecular weight but drops exponentially with the ratio of particle size to the tube diameter. However, the window ($a < d < d_c$) within which the particle motion is dominated by the hopping process is still appreciable and might be tested by experiments or computer simulations. For instance, the crossover particle size could be of one order of magnitude larger than the tube diameter ($d_c \simeq 10a$) in a highly entangled polymer liquid with $N/N_e \simeq 50$ providing $a/\xi \simeq 5$. The motion of very large particles with size larger than d_c (eq. 8.39) is diffusive with their terminal diffusion coefficient inversely proportional to the bulk viscosity particle size.

Dependence of particle diffusion coefficient on solution concentration

The correction from hopping diffusion to the concentration dependent terminal diffusion coefficient applies to particles with size d larger than the tube diameter $a\left(1\right)$ of entangled polymer melts without solvent. In addition to the two regimes expected for particles smaller than the tube diameter $a\left(\phi\right)$ (see section 7.2.2), there is an additional regime in which the terminal particle diffusion coefficient is affected by entanglements. This regime begins at a solution concentration ϕ_d^a, at which the tube diameter a (see eq. 7.2) is on the order of the particle size d: $a\left(\phi_d^a\right) \simeq d$. Therefore, the corresponding

crossover concentrations are

$$\phi_d^a \simeq \begin{cases} \left(\frac{a(1)}{d}\right)^{3/2}, & \text{theta} \\ \left(\frac{a(1)}{d}\right)^{1.32}, & \text{athermal} \end{cases} \tag{8.41}$$

In this regime ($\phi > \phi_d^a$) the terminal particle diffusion coefficient is contributed by both hopping diffusion and chain reptation process (refer to eq. 8.37). Recall the relations $\tau_e \simeq \tau_0 \left(\xi/b\right)^3 \left(a/\xi\right)^4$ (see eq. 8.25) and $\tau_{\text{rep}} \simeq \tau_e \left(N/N_e\left(\phi\right)\right)^3$ (see eq. 8.34) and using eqs. 7.1, 7.2, 7.6, 8.32 and the relation

$$N_e(\phi) \simeq N_e\left(1\right) \begin{cases} \phi^{-4/3}, & \text{theta} \\ \phi^{-1.32}, & \text{athermal} \end{cases} \tag{8.42}$$

one can simplify eq. 8.37 to obtain the concentration dependence of terminal particle diffusion coefficient by summing the two contributions:

$$D_t\left(\phi\right) \simeq \begin{cases} \frac{b^2}{\tau_0 N_e(1)^2} \exp\left[-\frac{d}{a(1)}\phi^{2/3}\right] \phi^{2/3} + \frac{b^3}{\tau_0 d} \frac{N_e(1)^2}{N^3} \phi^{-14/3}, & \text{theta} \\ \frac{b^2}{\tau_0 N_e(1)^2} \exp\left[-\frac{d}{a(1)}\phi^{0.76}\right] \phi^{0.76} + \frac{b^3}{\tau_0 d} \frac{N_e(1)^2}{N^3} \phi^{-3.93}, & \text{athermal} \end{cases} \tag{8.43}$$

for $\phi_d^a \;\; < \;\; \phi < 1$ and $d > a\left(1\right)$

In entangled polymer liquids of relatively short polymers ($N_e < N < N_c$) the terminal diffusion coefficient is mainly controlled by chain reptation process (see the second term in eq. 8.43). The crossover degree of polymerization N_c increases exponentially with relative particle size d/a (see eq. 8.38). For example, for $a/\xi \simeq 5$ and $d/a \simeq 4$ we have $N_c \simeq 4N_e$; when $a/\xi \simeq 5$ and $d/a \simeq 10$ we have $N_c \simeq 22N_e$.

In solutions of long polymers ($N > N_c$) there are two cases for the terminal particle diffusion coefficient depending on the particle size. If the size of particles is not very large: $a\left(1\right) < d < d_c\left(1\right)$, where $d_c\left(1\right)$ represents the value of crossover particle size d_c (see eq. 8.39) in polymer melt ($\phi = 1$)

$$d_c\left(1\right) \simeq a\left(1\right)\left[3\ln\left(N/N_e\left(1\right)\right) - \ln\left(a\left(1\right)/b\right)\right] \tag{8.44}$$

terminal particle diffusion coefficient is dominated by the contribution from hopping diffusion.

For particles with size larger than $d_c(1)$ the hopping diffusion still dominates as long as the solution concentration is below ϕ_{d_c}, at which the particle size d is comparable to crossover particle size $d_c(\phi_{d_c})$ (see eq. 8.39). Using eqs. 7.1, 7.2, 8.25 and 7.27, one can transform eq. 8.39 into logarithmic concentration dependence of the crossover particle size

$$
\begin{aligned}
d_c(\phi) &\simeq a(1)
\begin{cases}
\left[3\ln\left(\phi^{4/3} \frac{N}{N_e(1)} \right) - \ln\left(\phi^{1/3} [N_e(1)]^{1/2} \right) \right] \phi^{-2/3}, & \text{theta} \\[2mm]
\left[3\ln\left(\phi^{1.32} \frac{N}{N_e(1)} \right) - \ln\left([N_e(1)]^{1/2} \right) \right] \phi^{-0.76}, & \text{athermal}
\end{cases} \\[4mm]
&\simeq a(1)
\begin{cases}
\left[\ln\left(\frac{N^3 \phi^{11/3}}{[N_e(1)]^{7/2}} \right) \right] \phi^{-2/3}, & \text{theta} \\[2mm]
\left[\ln\left(\frac{N^3 \phi^{3.96}}{[N_e(1)]^{7/2}} \right) \right] \phi^{-0.76}, & \text{athermal}
\end{cases}
\end{aligned}
\tag{8.45}
$$

Note that in above calculation the solution volume fraction (concentration) ϕ is above the entanglement concentration, suggesting that the variation of the solution concentration is limited. Typically $d_c(\phi)$ decreases slowly by less than 10% as solution concentration increases by 20% for polymer solutions with long polymers $N > N_c(\phi)$. It suggests that changing the solution concentration will not significantly enlarge the window within which the particles experience hopping-dominated diffusion.

Particles with size d larger than $d_c(1)$ are expected to experience full solution viscosity above the crossover concentration ϕ_{d_c} and the terminal particle diffusion coefficient is dominated by the contribution from chain reptation process (see eq. 8.35).

Dependence of particle diffusion coefficient on polymer size

Consider the motion of large probe particles ($d > a$) of fixed size in entangled polymer liquids with different degrees of polymerization N but with the same concentration ϕ. The correction of hopping diffusion to the particle terminal diffusion coefficient is not important if the degree of polymerization is N smaller than the crossover value N_c (see eq. 8.38). Within the window $N_e < N < N_c$ the terminal particle diffusion coefficient is dominated by the contribution from chain reptation process (see eq. 8.37) and the large particles "feel" bulk solution viscosity at times longer than solution relaxation

time τ_{rep}. The terminal particle diffusion coefficient is reciprocally proportional to the solution viscosity η and decreases with increasing degree of polymerization N as

$$D_t(N) \simeq \frac{k_B T}{\eta d} \sim N^{-3}, \quad \text{for } N > N_e \tag{8.46}$$

The terminal particle diffusion coefficient will be controlled mainly from hopping diffusion for polymer liquids with very high degree of polymerization ($N > N_c$). For instance, using eq. 8.40 one can estimate the ratio of particle diffusion coefficient due to hopping diffusion to that due to chain reptation:

$$D_{\text{hop}}^{\text{liquids}} \Big/ D_{\text{rep}} \simeq \frac{d\xi}{a^2} \left(\frac{N}{N_e} \right)^3 \exp\left(-\frac{d}{a} \right) \tag{8.47}$$

which is about 7 for $a/\xi \simeq 5$, $d/a \simeq 5$, and $N/N_e \simeq 10$. In this case the diffusion coefficient is independent of polymer molecular weight and only determined by the relative value of the particle size with respect to the tube diameter (see eq. 8.31).

8.6 Summary: hopping diffusion of particles subjected to topological constraints

In this chapter we have discussed the mobility of large particles in unentangled polymer solids (networks and gels), entangled polymer solids, and entangled polymer liquids (melts and solutions). We introduce a novel hopping mechanism describing the diffusion of particles with size d larger than the network mesh size a_x of polymer solids (the tube diameter a of polymer liquids). It is found that although the large particles experience the topological constraints from the network (entanglement) cages, they can still move further by waiting for the fluctuations of surrounding confinement cages that would be large enough to allow them to slip through. Note that the calculation for hopping diffusion is based on the assumption that the confinement cages are uniform, i.e., all entropic barriers for hopping diffusion are the same. In reality the barriers have

distributions that make the problem more complex. For simplicity we do not take into account effect from the polydispersity of confinement cages.

In unentangled polymer solids the motion of particles with size larger than the network mesh size ($d > a_x$) at time scales shorter than the relaxation time τ_x of a network strand is not affected by network cages. Specifically, at time scales shorter than the relaxation time τ_ξ of a correlation blob the motion of large particles is not much affected by polymers and is diffusive with diffusion coefficient mainly determined by solvent viscosity. The large particles probe the modes of surrounding polymers at intermediate time scales $\tau_\xi < t < \tau_x$, and therefore, the particle motion is sub-diffusive with mean-square displacement $\langle \Delta r^2 \rangle \sim t^{1/2}$ (see eq. 8.14). At longer time scales ($t > \tau_x$) the large particles are trapped by network cages. In order to move further these particles have to wait until time τ_w^{gel}, at which the fluctuations of surrounding network cages will be large enough to allow the particles to pass through. Hopping diffusion coefficient of large particles exhibits an exponential dependence on the square of the ratio between the particle size and the network strand size: $D_{\text{hop}}^{\text{gel}} \sim \exp\left(-d^2/a_x^2\right)$.

In addition to permanent crosslinks, entangled polymer solids also contain entanglements. Unlike the permanent crosslinks, the entanglements are 'soft crosslinks' and thus the corresponding energy barrier for hopping diffusion between neighboring entanglement cages is weaker comparing to that for crosslinked network cages. The diffusion coefficient of large particles hopping between neighboring entanglement cages has a relatively weaker dependence on particle size, $D_{\text{hop}}^{\text{entg}} \sim \exp\left(-d/a_x\right)$, in comparison with that for crosslinked network cages. The hopping diffusion is the only mechanism via which a large particle can move further in entangled polymer solids because they cannot relax due to the existence of permanent crosslinks.

Besides hopping diffusion, large particles with size larger than the entanglement length a in entangled polymer liquids can also move further by waiting for the whole polymer liquids to relax at reptation time τ_{rep}. However, particles slightly larger than the tube diameter ($d \gtrsim a$) do not have to wait until τ_{rep} to move further; they can diffuse

by hopping between neighboring entanglement cages at time scales shorter than τ_{rep}. It is very difficult for extra large particles ($d >> a$) to hop between neighboring entanglement cages and in order to move further they have to wait for the whole polymer liquids to relax.

The hopping diffusion could be very interesting as it provides a novel explanation for the motion of particles with size around the characteristic length scales (network mesh size and tube diameter) of (unentangled and entangled) polymer solids and liquids. We are looking forward to experimental and computer simulation tests that will provide more information for diffusion of particles with size slightly larger than the network (entanglement) mesh size. Furthermore, a natural extension of the results presented in this chapter would be the mobility of particles in reversible polymer liquids, which will be briefly addressed in chapter 9.

CHAPTER 9

MOBILITY OF PARTICLES IN REVERSIBLE POLYMER LIQUIDS

If polymers form reversible associations (temporary bonds), such as hydrogen bonds [205–207], polymer dynamics is slowed down by these associations [182, 182, 192, 208–212]. In addition to the correlation length ξ, therefore, there are two other important length scales: the entanglement size (tube diameter) a and the reversible network strand size r_{st}, which is defined as the distance between two neighboring associations along the polymer chains. Similar to entangled polymer solids (see section 8.4), the mesh size r_{st} of a reversible network could be smaller or larger than the entanglement mesh size a depending on the density of reversible crosslinks, shown in Figure 9.1. We therefore have two cases for reversible polymer liquids: 1) high density of associations, in which the reversible network size r_{st} is smaller than the entangled mesh size a; 2) low density of associations, in which the reversible network size r_{st} is larger than the entangled mesh size a. The case for extremely high density of reversible associations ($r_{st} < \xi$) is not of our interests as reversible associations will form loops and thus not trap particles. The motion of particles in reversible polymer liquids is expected to combine the features of both entangled polymer liquids and polymer solids. In the following we shall discuss the mobility of probe particles with different sizes in these two types of reversible polymer networks formed via pairwise associations. We focus on identifying the main new features of particle mobility due to the reversible associations without considering the contribution from hopping diffusion mechanism.

9.1   High density of reversible associations

The mesh size of a reversible network with high density of reversible associations is smaller than the tube diameter ($r_{st} < a$). The regime for small particles (see section
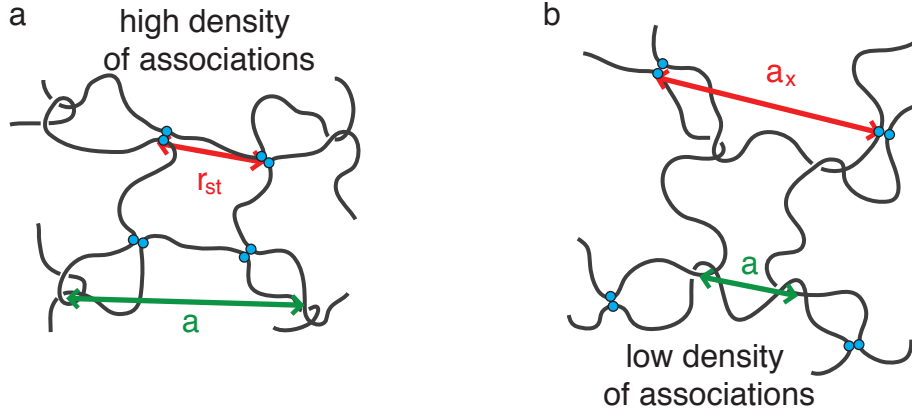
Figure 9.1: Schematic description of reversible polymer liquids formed via pairwise associations (pairs of green circles). a) The size r_{st} of a reversible network strand defined as the distance between two neighboring reversible associations along the chain is smaller than the entanglement size a if the density of reversible associations is high enough; b) The mesh size r_{st} of a reversible network strand is larger than the entanglement size a if the density of crosslinks is low enough.

7.1.1) is unchanged with particle mobility similar to that in pure solvent.

In comparison with the motion of particles in entangled polymer liquids (refer to section 7.1.2), the regime for intermediate size particles ($\xi < d < a$) in reversible polymer liquids splits into two parts (see Figure 9.2). Particles with size larger than the correlation length but smaller than the mesh size of reversible networks ($\xi < d < r_{st}$) are not affected by the temporary network. Therefore, their motion is similar to that in regular polymer liquids without associating polymers (see section 7.1.2).

Larger particles ($r_{st} < d < a$) are affected by reversible associations, but not yet entanglements. Such large particles are trapped by the reversible network, somewhat similar to the trapping of large particles by entanglements (see section 7.1.3), with the arrest of particle motion starting at time scale $\tau_{r_{st}}$, which corresponds the relaxation time of a polymer strand between two neighboring stickers that form a reversible bond,

$$\tau_{r_{st}} \simeq \tau_\xi \left(r_{st}/\xi \right)^4 \tag{9.1}$$

and ending at the lifetime τ_{st} of a reversible association (see the plateau in Figure 9.2). Here τ_{st} corresponds to the time it takes for a reversible association to break and the resulted two open stickers to find new partners. [210] Note that here we do no take into

Figure 9.2: Time dependence of the product of mean-square displacement and particle size ($\langle \Delta r^2(t) \rangle d$) for intermediate size particles ($\xi < d < a$) in reversible polymer liquids (melts and solutions) formed via pairwise associations. Here τ_0 is the relaxation time of a monomer; τ_ξ (eq. 7.8) is the relaxation time of a correlation blob; $\tau_{r_{st}}$ (eq. 9.1) is the relaxation time of a polymer section between two neighboring stickers, τ_{st} corresponds to the lifetime of a reversible association, τ_d^{st} (eq. 9.5) corresponds to the relaxation time of a polymer section with size on the order of the particle size d. Logarithmic scales.

account the possibility that particles may slip by if a reversible bond is open but the resulted two open stickers have not found new partners yet.

The temporary network starts to relax at time scale τ_{st} and thus it is possible for probe particles to move further. The effective viscosity felt by the particles increases with time, following a manner similar to the ordinary regime for intermediate particles in entangled polymer liquids (see section 7.1.2), but with sticker-controlled friction:

$$\eta_{\text{eff}}(t) \simeq \eta_s \left(\frac{r_{st}}{\xi} \right)^2 \left(\frac{\tau_{st}}{\tau_{r_{st}}} \right) \left(\frac{t}{\tau_{st}} \right)^{1/2}, \quad \text{for } t > \tau_{st} \tag{9.2}$$

Using eqs. 7.8 and 9.1 one can rewrite this expression (eq. 9.2) as

$$\begin{aligned}
\eta_{\text{eff}}(t) &\simeq \frac{k_B T \tau_\xi}{\xi^3} \left(\frac{r_{st}}{\xi} \right)^2 \frac{(\tau_{st} t)^{1/2}}{\tau_\xi (r_{st}/\xi)^4} \\
&\simeq \frac{k_B T}{(r_{st})^2 \xi} (\tau_{st} t)^{1/2}, \quad \text{for} \quad t > \tau_{st}
\end{aligned} \tag{9.3}$$

The physical explanation for the time-dependent effective viscosity "felt" by particles in reversible polymer liquids (eq. 9.3) is that the particles experience the sticky-Rouse dynamics of surrounding polymer chains [192]. Short chain sections with size smaller

113

than the entanglement length in reversible polymer liquids still follows Rouse dynamics, but slowed down by the sticker opening and closing. This modified chain dynamics in reversible polymer liquids is so-called sticky-Rouse [192]. The contribution from the reversible associations is represented by the term $(\tau_{st}/\tau_{r_{st}})$, which corresponds to the number of attempts to break a reversible bond before forming a new reversible association; the term $(t/\tau_{st})^{1/2}$ corresponds to the number of reversible network strands involved in the polymer Rouse mode at a certain time t.

Mean-square displacement of particles in the sticky-Rouse regime is

$$
\begin{aligned}
\left\langle \Delta r^2(t) \right\rangle &\simeq \frac{k_B T}{\eta_{\text{eff}}(t)\, d} t \simeq \frac{(r_{st})^2 \xi}{d} \left(\frac{t}{\tau_{st}} \right)^{1/2}, \\
&\text{for } \tau_{st} < t < \tau_{d_{st}} \text{ and } \xi < d < r_{st}
\end{aligned}
\tag{9.4}
$$

This second sub-diffusive regime (see the second regime with slope $1/2$ in Figure 9.2) continues until

$$
\tau_{d_{st}} \simeq \tau_\xi \left(\frac{\tau_{st}}{\tau_{r_{st}}} \right) \left(\frac{d}{\xi} \right)^4
\tag{9.5}
$$

at which the size of chain sections undergoing sticky-Rouse dynamics is on the order of the particle size. At longer times ($t > \tau_{d_{st}}$) the particles become diffusive but with mean-square displacement shifted by the factor of $\tau_{r_{st}}/\tau_{st}$ compared to that without stickers (refer to dash-dotted line in Figure 7.2).

$$
\begin{aligned}
\left\langle \Delta r^2(t) \right\rangle &\simeq \frac{k_B T}{\eta_{\text{eff}}(\tau_{d_{st}})\, d} t \simeq \frac{(r_{st})^4 \xi}{d^3} \frac{t}{\tau_{st}}, \\
&\text{for } t > \tau_{d_{st}} \text{ and } r_{st} < d < a
\end{aligned}
\tag{9.6}
$$

The effective viscosity felt by the particles

$$
\begin{aligned}
\eta_{\text{eff}}(\tau_{d_{st}}) &\simeq \frac{k_B T}{(r_{st})^2 \xi} (\tau_{st} \tau_{d_{st}})^{1/2} \\
&\simeq k_B T \frac{d^2 \tau_{st}}{(r_{st})^4 \xi}, \quad \text{for } t > \tau_{d_{st}} \text{ and } r_{st} < d < a
\end{aligned}
\tag{9.7}
$$

depends on particle size d and is $\tau_{st}/\tau_{r_{st}}$ times larger than that in the case without reversible associations (see eq. 7.14). Note that none of the above results depend on the molecular weight of polymers.

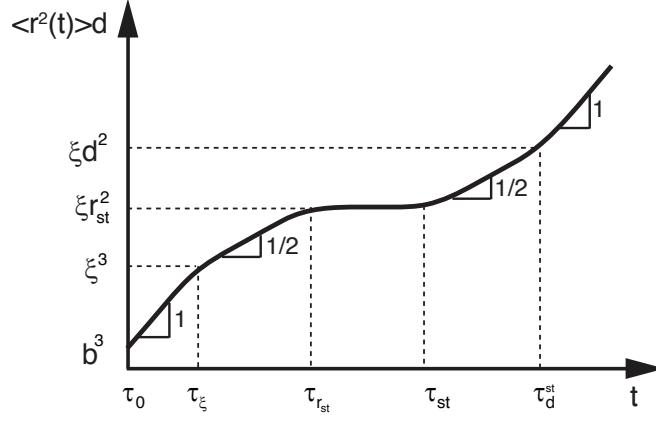**Figure 9.3:** Time dependence of the product of mean-square displacement and particle size ($\langle \Delta r^2(t)\rangle d$) for large particles ($d > a$) in reversible polymer liquids (melts and solutions) with high density of associations. Here τ_e^{st} (eq. 9.5) corresponds to the relaxation time of a polymer section with size on the order of the particle size d. Logarithmic scales.

Particles with size larger than the size of entanglement meshes ($d > a$) are affected by both reversible networks and entanglements. The particle motion is coupled to polymer sections undergoing a combination of sticky-Rouse and entangled dynamics (so-called sticky-reptation) [210]. Therefore, in addition to the plateau due to the trapping by reversible networks, there is another plateau for the time-dependent particle mean-square displacement, corresponding to the confinements from entanglement cages.

As shown in Figure 9.3, the first plateau starts around the relaxation time $\tau_{r_{st}}$ of a reversible network strand and continues up to the lifetime τ_{st} of a reversible association. At time scales longer than τ_{st} the motion of particles becomes subdiffusive as they probe the sticky-Rouse dynamics of surrounding polymer sections. This subdiffusive regime continues until the relaxation of an entanglement strand

$$
\begin{aligned}
\tau_e^{st} &\simeq \tau_\xi \left(a/\xi\right)^4 \left(\tau_{st}/\tau_{r_{st}}\right) \\
&\simeq \left(a/r_{st}\right)^4 \tau_{st}
\end{aligned}
\tag{9.8}
$$

which is longer than that without associations (eq. 8.25) by the factor of $\tau_{st}/\tau_{r_{st}}$.

At time scales longer than τ_e^{st} the particles "feel" the confinement from entangle-

ments. The particles are trapped, as demonstrated by the second plateau in Figure 9.3, and cannot move further until the whole reversible polymer liquids relax at the sticky-reptation time

$$\tau_{\text{rep}}^{st} \simeq \left(\tau_{st} / \tau_{r_{st}} \right) \tau_{\text{rep}} \tag{9.9}$$

in which τ_{rep} (eq. 8.34) is the relaxation time of a polymer liquid without associations. After that, the particles begin their terminal diffusion regime with diffusion coefficient determined by the viscosity of the reversible polymer liquids.

$$
\begin{aligned}
\left\langle \Delta r^2(t) \right\rangle \quad &\simeq \quad \frac{k_B T}{\eta d} t \simeq \frac{a^2 \xi}{d} \frac{\tau_{r_{st}}}{\tau_{st}} \frac{t}{\tau_{\text{rep}}} \\
&\simeq \quad \frac{a^2 \xi}{d} \frac{\tau_\xi \left(r_{st}/\xi \right)^4}{\tau_{st}} \frac{t}{\tau_\xi \left(a/\xi \right)^4 \left(N/N_e \right)^3} \\
&\simeq \quad \frac{a^2 \xi}{d} \left(\frac{r_{st}}{a} \right)^4 \left(\frac{N_e}{N} \right)^3 \frac{t}{\tau_{st}},
\end{aligned}
\tag{9.10}
$$

$$\text{for } t \quad > \quad \tau_{\text{rep}}^{st} \text{ and } d > a$$

9.2 Low density of reversible associations

In reversible polymer liquids with low density of associations the reversible network strand size could be larger than the entanglement length ($r_{st} > a$). Probe particles with size smaller than the entanglement length is not affected by neither entanglements nor reversible associations and their behavior is similar to that in polymer liquids without associations. Particles larger than the entanglement mesh size ($d > a$) start to "feel" the confinement from entanglement cages at time scales longer than the relaxation time τ_e of an entanglement strand. They cannot move until the whole reversible polymer liquids relax at the sticky-reptation time τ_{rep}^{st} (see eq. 9.9). Therefore, there is only one plateau regime ($\tau_e < t < \tau_{\text{rep}}^{st}$) for the time-dependent mean-square displacement of large particles, shown in Figure 9.4. This plateau is longer than that for large particles in regular entangled polymer liquids (see solid line in Figure 7.2) by the factor $\tau_{st}/\tau_{r_{st}}$,
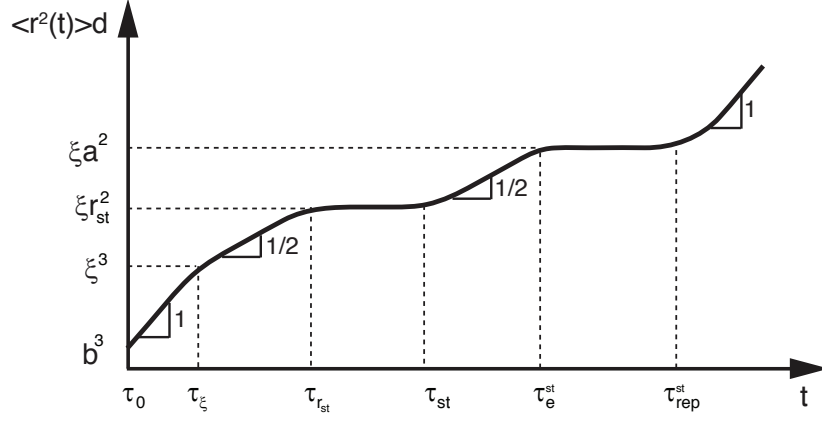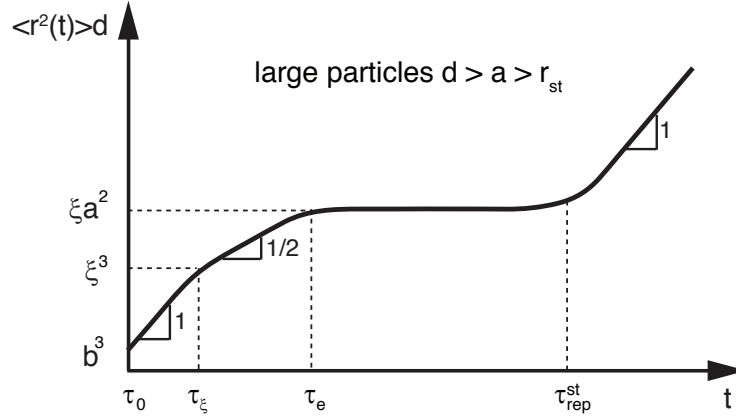
Figure 9.4: Time dependence of the product of mean-square displacement and particle size ($\langle \Delta r^2(t) \rangle d$) for large particles ($d > a$) in reversible polymer liquids (melts and solutions) with low density of associations ($r_{st} > a$). Logarithmic scales.

because it starts at entanglement time τ_e that does not depend on associations (eq. 8.25), but ends at a longer sticky-reptation time τ_{rep}^{st}.

9.3 Summary: particle diffusion is slowed down by reversible networks

Here we briefly summarize the main features of particle diffusion in reversible polymer liquids with high density of associations ($r_{st} < a$) by schematically presenting the dependence of terminal particle diffusion coefficient on particle size (Figure 9.5). Similar to that in entangled polymer liquids, there are three main regimes for the terminal particle diffusion coefficient depending on the particle size d with respect to the correlation length ξ, size r_{st} of a reversible network strand, and the entanglement length a.

The first regime is for small particles with size smaller than the correlation length ($b < d < \xi$). The motion of small particles is the same as that in polymer solutions with no associations, and thus diffusive with terminal diffusion coefficient inversely proportional to the particle size (pink zone in Figure 9.5).
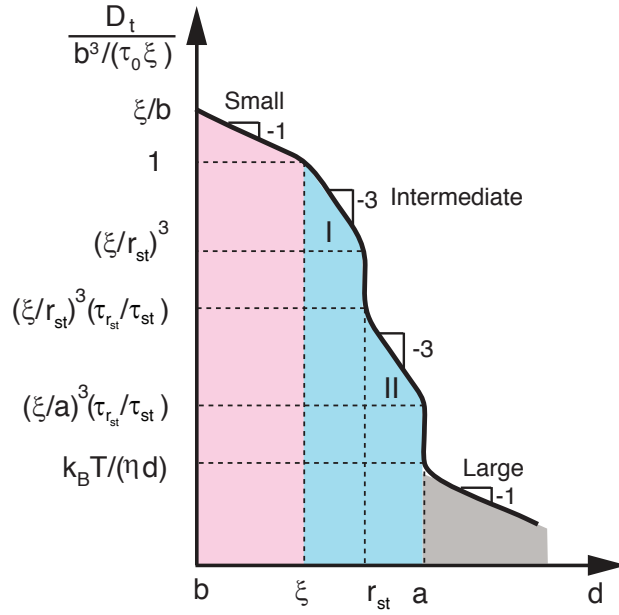
Figure 9.5: Dependence of terminal particle diffusion coefficient D_t on particle size d in reversible polymer liquids with high density of associations ($r_{st} < a$). Logarithmic scales.

The second regime corresponds to intermediate size particles with size larger the correlation length but smaller than the entanglement length ($\xi < d < a$), shown by the light blue region in Figure 9.5. Terminal particle diffusion of intermediate size particles consists of two sub-regimes due to the existence of reversible associations. In the first sub-regime particles with size smaller than the reversible network strand size ($\xi < d < r_{st}$) probe the segmental dynamics of surrounding polymer chains. In this sub-regime the terminal diffusion coefficient is inversely proportional to the cube of particle size. In the second sub-regime the terminal diffusion coefficient of relatively large particles ($r_{st} < d < a$) has a similar dependence on particle size ($D_t \sim d^{-3}$), but shifted down from the first sub-regime by the factor $\tau_{r_{st}}/\tau_{st}$.

The third regime corresponds to particles with size larger than the entanglement length ($d > a$). Terminal diffusion coefficient of such large particles is also shifted down by the factor of $\tau_{r_{st}}/\tau_{st}$ compared with that in polymer liquids without associations.

Finally, we would like to stress out that the shift of terminal diffusion coefficient due

118

to the arrested motion of particles by the temporary networks is the main new feature of particle diffusion in reversible polymer liquids.

CHAPTER 10

CONCLUSIONS AND REMARKS: PART II

In the second part of this thesis we have discussed the motion of particles in three polymeric systems: 1) polymer liquids; 2) polymer solids, and 3) reversible polymer liquids and linked the thermal motion of particles to the dynamics of the surrounding polymers.

The particle dynamics (mean-square displacement) exhibits different time dependencies on different time scales. At relatively short time scales the particle motion could be sub-diffusive with mean-square displacement proportional to $1/2$ power of time. At long time scales, the probe particles become diffusive with mean-square displacement linearly proportional to time, but not necessarily experiencing the bulk viscosity of the probed environments if the particles are not very large. In fact, they could "feel" an effective viscosity that is much smaller than the bulk value, which is so-called breakdown of Stokes-Einstein relation [139].

Large particles subjected to topological constraints, such as entanglements and crosslinks in networks, are not necessarily permanently trapped by local confinement cages. These large particles can still move further through a hopping diffusion mechanism, i.e., particles can wait for fluctuations of confinement cages that could be large enough to allow them to slip though.

It is expected that the results presented here can be applied to interpret the experiments using non-sticky probe particles to detect the local structure and dynamics of complex fluids such as semiflexible polymer solutions, biological gels, and active polymer solutions.

APPENDIX A

EXPERIMENTAL METHODS

Human tissue procurement and cell culture. Tissues and cells were provided by the Cystic Fibrosis (CF) Center Tissue Core Facility of the University of North Carolina at Chapel Hill under the auspices of protocols approved by the Institutional Committee on the protection of the rights of human subjects. HBE cells from non-CF lungs are harvested by enzymatic digestion as previously described [119]. Disaggregated human bronchial epithelial (HBE) cells are seeded on 12 mm diameter Transwell Clear supports (Corning Costar, Cambridge, MA) at a density of 2.5×10^5 cells/cm^2 in a well-defined airway cell media [119]. Cultures are maintained at an air-liquid interface until fully differentiated (~ 4 weeks).

Transmission electron microscopy (TEM). Samples for electron microscopy were obtained from cryopreserved HBE cell cultures. Cryopreservation was used to maintain native conformation of mucus layer, periciliary layer (PCL), plasma membranes and cilia. Cells sections were examined using a FEI/Phillips Tecnai 12 (FEI Company, Hillsboro, OR) TEM at 80 kV with a 1k×1k CCD camera (Gatan, Pleasanton, CA) to assess their structure at submicron level.

Fractionation of dextran (unlabeled and fluorescently labeled). Size exclusion chromatography was used to separate green fluorescently-labeled dextrans into fractions with well-defined molecular sizes (weight average hydrodynamic diameter d). Raw batches of 2 MDa dextran (purchased from Sigma-Aldrich, St. Louis, MO and Invitrogen, Carlsbad, CA) was fractionated by a Sepharose CL-2B column (GE Healthcare Life Sciences, Buckinghamshire, England) and eluted by phosphate buffered saline (PBS) with elution volume of 150 ml at a flow rate 0.2 ml/min using a Rheos 2000 pump (Flux Instruments, Basel, Switzerland). Fractions of 2 ml were collected and characterized by dynamic light scattering to obtain the hydrodynamic size of fraction-

ated polymers. Fractionated dextran with desired sizes was dialyzed (10 kDa molecular weight cutoff, Thermo Scientific, Rockford, IL) against distilled water and then lyophilized prior to use.

Measurements of the permeability of PCL using confocal microscopy. To image the penetration of dextran molecules of different sizes into PCL, we employed a dual-labeling technique of the PCL layer. In each experiment, a solution of green-fluorescent probe dextran of a particular hydrodynamic diameter d was mixed with the solution of small ($d \sim 2$ nm) unfractionated Texas Red fluorescent dextran (average molecular weight 3 kDa). Dilute solution of this mixture was then added to the lumen of a freshly washed HBE culture. Both fluorescent reagents were added at a concentration of ~ 0.1 mg/ml in PBS (with osmotic pressure on the order of 1 Pa). In each experiment, 50 μl solutions were added to cell culture and studied within 30 minutes to ensure no significant effects of water absorption by cells. High resolution XZ-confocal images were obtained using a Leica TCS SP5 laser scanning confocal microscope (Leica Microsystems, Wetzlar, Germany). The exclusion thickness of the green dye was measured as the difference in the thickness of the red and yellow (red + green) regions (Figure 3.3).

Transmission-light imaging of cilia height. Images of the airway cilia before and after exposure to the various osmotic reagents were obtained using differential interference contrast (DIC) microscopy of sections of airway cultures viewed in profile. Here, $1\text{mm} \times 12\text{mm}$ sections of HBE cell cultures were placed in a special chamber allowing access to the apical and basolateral solutions. After control images in PBS, the apical solution was replaced with the 150 μl desired osmotic reagents. A custom perfusion device was used to exchange solutions during these studies. For studies investigating the cilia height under various concentrations of endogenous mucus, immiscible perfluorocarbon (Fluorinert FC-77, 3M Specialty Materials, St. Paul, MN) was carefully placed on both the apical and basolateral compartments to prevent dehydration [213].

APPENDIX B

CHARACTERIZATION OF DEXTRAN AND AGAROSE

In our experiments fractionated dextran molecules of different sizes were used as molecular probes for quantifying the mesh size within the PCL. Large dextran molecules with weight average hydrodynamic diameter greater than 50 nm as well as agarose gel were used as mucus simulants to compress the PCL. Fractions of dextran molecules with different sizes were obtained using size exclusion chromatography (SEC) and then characterized by dynamic light scattering (DLS). The weight average hydrodynamic diameter of agarose was obtained using the dynamic light scattering.

B.1 Dynamic light scattering

Dynamic light scattering [214, 215] measurements involve the analysis of the time autocorrelation function of scattered light. The normalized time autocorrelation function of the intensity of the scattered light $g^2(\tau)$ for a given delay time τ is

$$g^2(\tau) = \frac{\langle I(t) I(t+\tau) \rangle}{\langle I(t) \rangle^2} \tag{B.1}$$

where $I(t)$ and $I(t+\tau)$ are the intensities of the scattered light at times t and $t + \tau$, respectively, and the braces indicate averaging over t. The intensity-intensity time autocorrelation function can be expressed in terms of the field-field time autocorrelation function $g^1(\tau)$:

$$g^2(\tau) = B + A\left[g^1(\tau)\right]^2 \tag{B.2}$$

in which A and B are fitting parameters: A–amplitude, B–baseline; and $g^1(\tau)$ is given by

$$g^1(\tau) = \frac{\langle E(t) E^*(t+\tau) \rangle}{\langle E(t) E^*(t) \rangle} \tag{B.3}$$

in which $E(t)$ and $E(t+\tau)$ are the scattered electric fields at times t and $t + \tau$.

For monodisperse particles in solution the field correlation function decays expo-

nentially

$$g^1(\tau) = \exp(-\Gamma\tau) \tag{B.4}$$

with a decay rate of

$$\Gamma = Dq^2 \tag{B.5}$$

where D is the diffusion coefficient of the particle and q is the magnitude of the scattering wave vector.

For a polydisperse sample, $g^1(\tau)$ can no longer be represented as a single exponential and must be represented as a sum or an integral over a distribution of decay rates $G(\Gamma)$:

$$g^1(\tau) = \int_0^\infty G(\Gamma)\exp(-\Gamma\tau)\,d\Gamma \tag{B.6}$$

where $G(\Gamma)$ is normalized:

$$\int_0^\infty G(\Gamma)\,d\Gamma = 1 \tag{B.7}$$

and $G(\Gamma)\,d\Gamma$ is the fraction of total intensity scattered, on average, by molecules for which $Dq^2 = \Gamma$, within the interval $d\Gamma$.

A simple method, called cumulants analysis [216–218], can be used to characterize $G(\Gamma)$ using DLS data. The form of $g^1(\tau)$ given by eq. B.6 is equivalent to the moment-generating function:

$$\ln\left[g^1(\tau)\right] = -\langle\Gamma\rangle\,\tau + \frac{\kappa_2}{2!}\tau^2 - \frac{\kappa_3}{3!}\tau^3 + \cdots \tag{B.8}$$

in which

$$\langle\Gamma\rangle \equiv \int_0^\infty \Gamma G(\Gamma)\,d\Gamma, \tag{B.9}$$

$$\kappa_2(\Gamma) = \mu_2, \tag{B.10}$$

$$\kappa_3(\Gamma) = \mu_3, \tag{B.11}$$

$$\cdots$$

where μ_m are the moments about the mean defined by

$$\mu_m \equiv \int_0^\infty (\Gamma - \langle\Gamma\rangle)^m\,G(\Gamma)\,d\Gamma \tag{B.12}$$

From eqs. B.2 and B.8 one can obtain

$$g^2(\tau) = B + A \exp\left[-2\langle\Gamma\rangle\tau + \kappa_2\tau^2 - \frac{\kappa_3}{3}\tau^3 + \cdots\right] \quad (\text{B.13})$$

The first cumulant describes the average decay rate of the distribution. The second cumulant corresponds to the variance, and the third term provides a measure of the skewness or asymmetry of the distribution.

It is worthwhile to point out the first cumulant (eq. B.9) is directly proportional to average diffusion coefficient, $\langle D\rangle$, whose physical meaning is described as following. Note that typically the intensity of light scattered by macromolecular species i is proportional to the molecular weight M_i of the species times the weight concentration c_i:

$$G(\Gamma) = \frac{\sum_i c_i M_i \delta(\Gamma - \Gamma_i)}{\sum_i c_i M_i} \quad (\text{B.14})$$

Therefore, $\langle D\rangle$ is called z-average diffusion coefficient

$$\begin{aligned}
\langle D\rangle &= \langle\Gamma\rangle/q^2 \\
&= D_z \equiv \sum_i c_i M_i D_i \Big/ \sum_i c_i M_i \quad (\text{B.15})
\end{aligned}$$

The software package integrated with Malvern dynamic scattering instruments provides three types of distributions to characterize the tested sample: 1) intensity-size distribution, 2) volume-size distribution, and 3) number-size distribution. Below we present a simple example to demonstrate the difference between intensity, volume, and number distributions. [219] Consider 2 populations of spherical particles of diameter 5 nm and 50 nm with equal numbers (Figure B.1a). If a number distribution of these 2 particle populations is plotted, a plot consisting of 2 peaks positioned at 5 nm and 50 nm of a 1 to 1 ratio will be obtained. If this number distribution is converted to volume, then the ratio of the 2 peaks will change to 1 : 1000 because the volume of a sphere is proportional to d^3. If this is further converted to an intensity distribution, a $1 : 10^6$ ratio between the 2 peaks will be obtained because the intensity of scattering is proportional to the product of concentration and mass and thus $G(\Gamma) \propto d^6$. In that sense, for a

polydisperse sample containing a wide size range of particles, the intensity distribution is dominated by the particles with larger size and the obtained results is biased by the contribution from larger particles. Therefore, it would be more realistic to convert the intensity distribution to the volume (concentration) distribution.
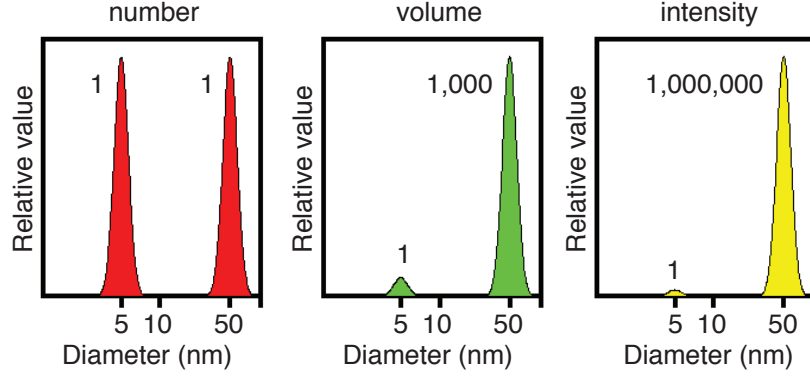
Figure B.1: Number, volume and intensity distributions of a bimodal mixture of 5 and 50 nm particles present in equal numbers.

In our experiments we measured the diffusion coefficient of flexible polymers with typical size smaller than the wavelength 633 nm of He-Ne laser. The results provided from Malvern DLS system are presented as intensity-size distribution. Recall that the scattered light intensity is proportional to the product of concentration and mass: $I \sim cM$, one can convert the intensity-size distribution to concentration-distribution via

$$c \sim I/R^{1/\upsilon} \tag{B.16}$$

because the mass M of polymers is proportional to the power of polymer size R:

$$M \sim R^{1/\upsilon} \tag{B.17}$$

where υ is Flory exponent for flexible polymers. In good solvent $\upsilon = 3/5$ [60] for linear polymers and $\upsilon = 1/2$ [114] for randomly branched polymers. Furthermore, one can convert the concentration distribution to number-size distribution

$$n \sim c/M \sim I/R^{2/\upsilon} \tag{B.18}$$

from which one can estimate the number average molecular size.

B.2 Weight average hydrodynamic diameter of dextran molecules

B.2.1 Unfractionated dextran molecules

The raw (unfractionated) dextrans samples at dilute concentrations were characterized by DLS and the results are shown in Figure B.2a. The measurements at different concentrations agree with each other.
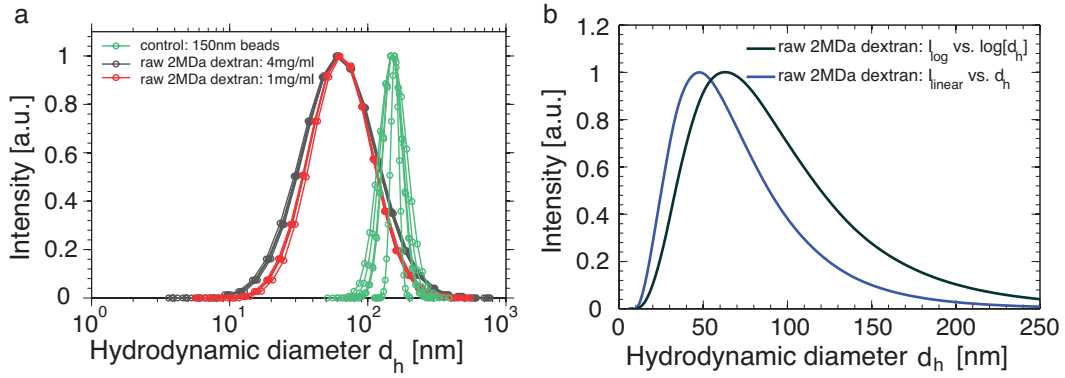
Figure B.2: Dynamic light scattering (DLS) characterization of dextran molecules. (a) DLS characterization of control 150 nm beads (green lines) and raw 2 MDa dextran molecules in solutions with concentrations of 4 mg/ml (black lines) and 1 mg/ml (red lines). (b) Transformation from $I_{\log}$ vs. $\log(d_h)$ to I_{linear} vs. d_h using eq. B.20.

Note that the results correspond to the intensity distribution on linear-logarithmic scale, i.e., $I_{\log}$ vs. $\log d_h$. Considering the invariance of the mass of molecules at different representations (linear-log and linear-linear coordinate systems), the scattered intensity of molecules with size in the interval $\Delta(\log d_h)$ within linear-log coordinate is the same as that in the interval Δd_h within linear-linear coordinate. Therefore, the conversion from linear-logarithmic to linear-linear scale can be obtained by considering the Jacobian of transformation

$$I_{\log}\Delta(\log d_h) = I_{\text{linear}}\Delta d_h \tag{B.19}$$

which gives

$$I_{\text{linear}}(d_h) = I_{\log}\frac{1}{d_h \ln 10} \propto I_{\log}/d_h \tag{B.20}$$

An example of using this relation to transform the $I_{\log}$ vs. $\log d_h$ distribution to I_{linear} vs. d_h distribution is shown by Figure B.2b.

From the I_{linear} vs. d_h distribution (blue line in Figure B.2b) the z-average hydrodynamic diameter (in fact, it should be z-average diffusion coefficient) of raw 2 MDa dextran molecules can be calculated:

$$\langle d_h \rangle_z \equiv \sum_i (I_{\mathrm{linear}})_i (d_h)_i \bigg/ \sum_i (I_{\mathrm{linear}})_i = 73 \text{ nm} \qquad \text{(B.21)}$$

where $(d_h)_i$ corresponds to the hydrodynamic diameter of dextran molecules with mass of M_i. This value is in exact agreement with that provided by the Malvern software package.

Considering the relation between molecular size and mass of dextran molecules in good solvent [115]

$$R \sim M^v \sim M^{0.48} \qquad \text{(B.22)}$$

using eqs. B.16 and B.18 one can the transform the intensity-size distribution into concentration-size and number-size distributions, shown in Figure B.3. From such dis-

Figure B.3: Representative plots showing the transformation from intensity-size distribution to concentration-size and number-size distributions.

tributions one can estimate the weight and number average sizes of dextran molecules
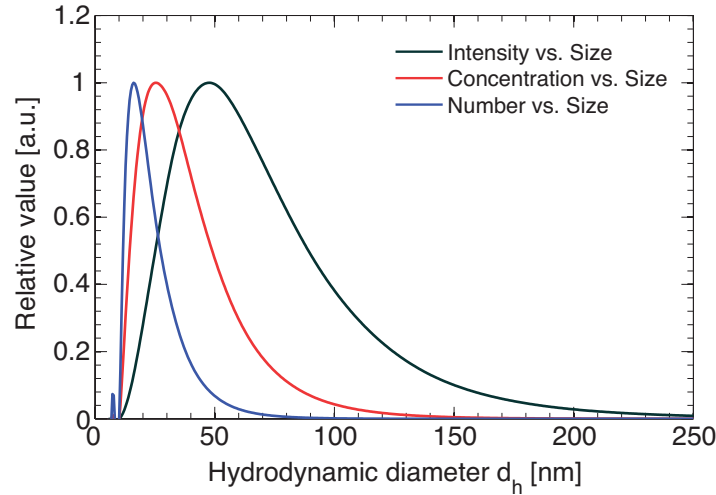
$$\langle d_h \rangle_w \equiv \sum_i c_i (d_h)_i \bigg/ \sum_i c_i = 41 \text{ nm} \qquad \text{(B.23)}$$

128

$$\langle d_h \rangle_n \equiv \sum_i n_i \, (d_h)_i \Big/ \sum_i n_i = 25 \text{ nm} \tag{B.24}$$

We can also estimate the number average of molecular volume $(d_h)^3$ using the number-size distribution in Figure B.3:

$$\left\langle (d_h)^3 \right\rangle_n \equiv \sum_i n_i \, [(d_h)_i]^3 \Big/ \sum_i n_i = 3.1 \times 10^4 \text{ nm}^3 \tag{B.25}$$

which gives

$$\left\langle (d_h)^3 \right\rangle_n^{1/3} \simeq 31 \text{ nm} \tag{B.26}$$

We would like to compare the $\left\langle (d_h)^3 \right\rangle_n^{1/3}$ values obtained from DLS (eq. B.26) with the size estimated from our osmotic pressure measurements. Our osmotic pressure measurements indicate that the number average molecular weight M_n of raw unlabeled dextran samples is about 200 kDa and the overlap concentration c^* is about 2.5×10^{-2} g/ml (see section 4.1.2). Note that the overlap concentration is defined as

$$\begin{aligned} c^* &\equiv \frac{M}{V} = \frac{\sum_i n_i M_i}{\sum_i n_i v_i} \simeq \frac{\sum_i n_i M_i}{\sum_i n_i \, (R_g)_i^3} \\ &\simeq \frac{M_n}{\left\langle (R_g)^3 \right\rangle_n} \end{aligned} \tag{B.27}$$

Therefore, the osmotic pressure measurements provide the number average value of $\left\langle (R_g)^3 \right\rangle^{1/3}$ for the raw dextran molecules:

$$\begin{aligned} \left\langle R_g^3 \right\rangle_n^{1/3} &\simeq \left(\frac{M_n}{N_{Av} c^*} \right)^{1/3} \\ &\simeq \left(\frac{2 \times 10^5 g/mol}{6.02 \times 10^{23}/mol \times 2.5 \times 10^{-2} g/ml} \right)^{1/3} \\ &\simeq 24 \text{ nm} \end{aligned} \tag{B.28}$$

Now we have to consider the relation between the hydrodynamic diameter d_h and radius of gyration R_g for dextran molecules. Dextran is a branched molecule. At relatively low molecular weight it is more linear-like and at high molecular weight it is more randomly-branched-like. [115, 220] Experimental measurements indicate that the ratio between radius of gyration R_g and hydrodynamic diameter d_h is (Table 8.4 in ref. [60])

$$R_g/d_h = \begin{cases} 1, & \text{for randomly branched} \\ 0.75, & \text{for linear} \end{cases} \tag{B.29}$$

Our results (eqs. B.26, B.41, and B.28) indicate that

$$R_g/d_h = \frac{24\ \mathrm{nm}}{31\ \mathrm{nm}} \simeq 0.77$$

which is in agreement with the prediction (eq. B.29), suggesting the consistence of our measurements.

B.2.2 Fractionated dextran molecules

Following the protocol described above one can estimate the weight and number average sizes of fractionated dextran molecules. The results are listed in Table B.1 below.

MW [kDa]^a	Frac. #^{b}	$\langle d_h \rangle_z$ [nm]	$\langle d_h \rangle_w$ [nm]	$\langle d_h \rangle_n$ [nm]	$\langle (d_h)^3 \rangle_n^{1/3}$ [nm]
3	N/A^c	2.8	2.2	1.8	2.0
75	9	8.9 ± 0.6	4.6 ± 0.8	2.6 ± 0.9	3.6 ± 0.8
500	13	20.1 ± 0.6	9.7 ± 2.4	5.6 ± 2.5	7.2 ± 2.6
500	10	26.6 ± 0.3	16.7 ± 1.0	11.2 ± 1.2	13.5 ± 1.2
500	7	51.9 ± 1.0	28.4 ± 1.3	17.3 ± 1.4	21.8 ± 1.4
2,000	36	23.8 ± 0.3	13.8 ± 0.5	8.7 ± 0.5	10.8 ± 0.5
2,000	32	32.1 ± 2.8	17.5 ± 1.4	11.1 ± 1.2	13.7 ± 1.3
2,000	28	40.9 ± 0.2	26.6 ± 0.5	18.2 ± 0.7	21.8 ± 0.6
2,000	25	50.2 ± 0.6	36.8 ± 1.1	27.7 ± 1.6	31.7 ± 1.4
2,000	24	52.9 ± 0.4	42.5 ± 2.6	34.7 ± 3.7	38.1 ± 3.4
2,000	22	59.6 ± 0.5	47.4 ± 0.5	38.2 ± 1.0	42.3 ± 0.8
2,000	20	65.0 ± 0.9	57.4 ± 1.6	50.9 ± 3.3	53.9 ± 2.6

Table B.1: Dynamic light scattering characterization of dextran molecules. ^{a}Molecular weight (MW) of raw dextran samples prior to fractionation. The values correspond to the labeled ones on the commercial products (see appendix A). Starting materials with different molecular weight were used to obtain fractionated molecules with a wide range of sizes. ^{b}The number of each fraction obtained from size exclusion chromatography. ^{c}Dextran molecules were directly used for experiments without fractionation.

B.2.3 Agarose

Solutions of agarose in PBS with three different low concentrations, 2 mg/ml, 0.25 mg/ml, and 0.2 mg/ml, were characterized by DLS. Note that solutions with concentration about 2 mg/ml become more gel-like at room temperature. Agarose solution with concentration lower than 0.2 mg/ml has very weak signal during DLS measurements and the measurements becomes unreliable. For each concentration five measurements were obtained and the results are shown in Figure B.4a. As shown by the different colored curves in Figure B.4a, agarose has a very wide molecular weight distribution.
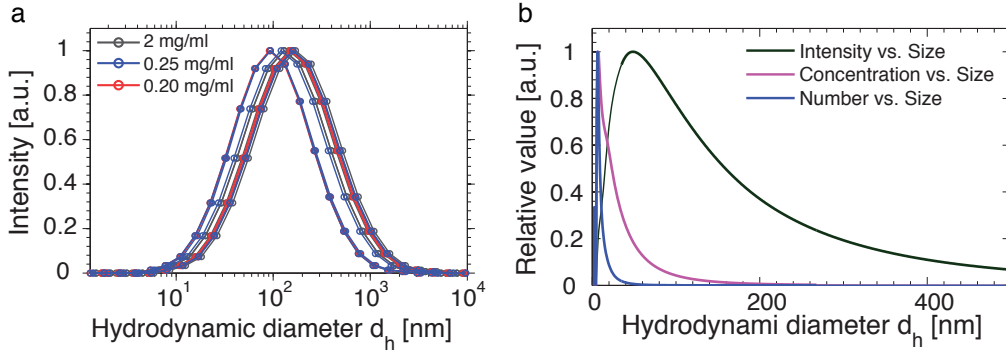
Figure B.4: Dynamic light scattering (DLS) characterization for agarose. a, DLS characterization agarose in dilute solutions of three different concentrations. b, Example plots showing the intensity-size, concentration-size, and number-size distributions of agarose from the DLS measurement.

Agarose is a linear polymer and the relation between the molecular size and mass is: $R \sim M^{v} \sim M^{0.588}$. Following a similar protocol used for dextran molecules one can convert the intensity-size distribution to concentration-size and number-size distributions. The z-average, weight average, and number average hydrodynamic diameters as well as the value of $\left\langle (d_h)^3 \right\rangle_n^{1/3}$ for agarose are listed in Table B.2.

The value of number average $\left\langle (d_h)^3 \right\rangle_n^{1/3}$ is

$$\left\langle (d_h)^3 \right\rangle_n^{1/3} \simeq 27 \pm 4 \text{ nm} \tag{B.30}$$

Now we would like to check this number against the value obtained from osmotic

Conc. [mg/ml]	$\langle d_h \rangle_z$ [nm]	$\langle d_h \rangle_w$ [nm]	$\langle d_h \rangle_n$ [nm]	$\langle (d_h)^3 \rangle_n^{1/3}$ [nm]
2.00	246.8 ± 29.5	47.4 ± 5.7	14.7 ± 1.8	28.8 ± 3.3
0.25	207.8 ± 59.6	42.0 ± 8.6	13.4 ± 2.4	26.0 ± 5.1
0.20	214.2 ± 61.2	43.0 ± 8.7	13.8 ± 2.2	26.8 ± 4.9
Average	222.9 ± 51.4	44.1 ± 7.6	14.0 ± 2.1	27.2 ± 4.4

Table B.2: Dynamic light scattering characterization of dilute solutions of agarose molecules with different concentrations.

pressure characterization. Our osmotic pressure measurements suggest that the number average molecular weight of agarose is about 7×10^4 Da and the overlap concentration is about 2.5×10^{-2} g/ml (see section 4.1.2). From this information one can estimate the number average molecular size of agarose

$$
\begin{aligned}
\langle R_g^3 \rangle_n^{1/3} & \simeq \left(\frac{M_n}{N_{Av} c^*} \right)^{1/3} \\
& \simeq \left(\frac{7 \times 10^4 g/mol}{6.02 \times 10^{23}/mol \times 2.7 \times 10^{-2} g/ml} \right)^{1/3} \qquad \text{(B.31)} \\
& \simeq 18 \text{ nm}
\end{aligned}
$$

The ratio between $\langle R_g^3 \rangle_n^{1/3}$ (eq. B.31) and $\langle (d_h)^3 \rangle_n^{1/3}$ (eq. B.30) is

$$
\frac{\langle R_g^3 \rangle_n^{1/3}}{\langle (d_h)^3 \rangle_n^{1/3}} = \frac{R_g}{d_h} \simeq 0.67 \pm 0.11 \qquad \text{(B.32)}
$$

which is in agreement with the predicted value of 0.75 for linear polymers (eq. B.29 and Table 8.4 in ref. [60]).

B.3   Size exclusion chromatography

The raw unlabeled 2 MDa dextran sample was also characterized by size exclusion chromatography using Sepharose CL-2B column with a flow rate of 0.2 ml/min. The total volume of the column is 110 ml and the elution volume was chosen to be from 130 to 150 ml. The volume of each fraction was chosen to be 2 or 3 ml. Typical distribution curves describing the relation between the UV absorbency and the elution volume is shown in Figure B.5. The UV absorbency distribution curves in Figure B.5
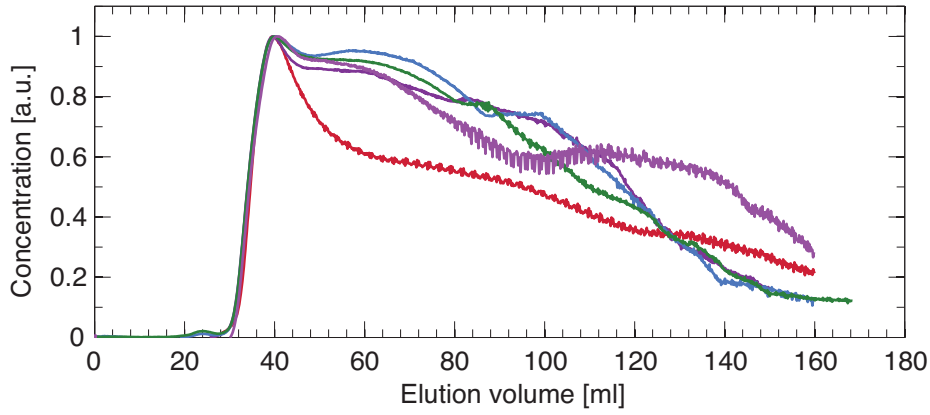
Figure B.5: Relationship between UV absorbency (concentration) of unlabeled dextran molecules and the elution volume using size exclusion chromatography (SEC). Different curves correspond to the characterization at different times but using the same protocol.

is equivalent to concentration-elution volume distributions because the UV absorbency for a polymer in solution is proportional to the polymer concentration (eq. 9.10 in ref. [221]).

B.3.1   Calibration of Sepharose CL-2B column

Typically the elution volume is linearly proportional to the logarithmic of molecular weight [221], and therefore, molecular size d

$$d \simeq a \exp\left(-v/b\right) \tag{B.33}$$

where parameters a and b are to be determined by column calibration. Provided the calibration curve for CL-2B column, in principle the relation between the relative amount of materials and the elution volume can be used to estimate the number average molecular mass and weight average molecular mass, and therefore, the polydispersity of the raw dextran sample. Unfortunately, CL-2B column has relatively large pore size covering molecular weight ranges from 10^5 Da to 2×10^7 Da, which is beyond the typical molecular weight ($< 10^5$ Da) of the calibration standards. We used Sepharose CL-2B column to fractionate 2 MDa dextran samples and each fraction was characterized by

dynamic light scattering (DLS) measurements and the results are shown in Table B.3.

Frac. #	Elution Volume v [ml]	$\langle d_h \rangle_z$ [nm]	$\langle d_h \rangle_w$ [nm]	$\langle d_h \rangle_n$ [nm]
11	33	137	104	79
15	45	114	91	77
20	60	95	74	63
25	75	84	57	40
30	90	76	42	24

Table B.3: Calibration of Sepharose CL-2B column for size exclusion chromatography.

Since UV detector in SEC measures the concentration of polymers, it is reasonable to use results for $\langle d_h \rangle_w$ vs. v in Table B.3 to determine the calibration parameters a and b. Fitting eq. B.33 by these results one obtains $a = 174 \pm 30$ nm and $b = 66 \pm 14$ ml for column Sepharose CL-2B:

$$d_h \simeq 174 \text{ nm} \exp\left(-\frac{v}{66 \text{ ml}}\right) \tag{B.34}$$

B.3.2 Dextran molecules

Eq. B.34 can be used to transform the concentration-volume (c_{vol}) distribution to the concentration-size (c_{size}) distribution. Recall the invariance of mass in different representations, the mass of molecules within the interval Δv in concentration vs. volume coordinates (c_{vol} vs. v) is the same as that within the interval $|\Delta d_h|$ in concentration vs. molecular size coordinates (c_{size} vs. d_h) coordinates:

$$c_{vol} \Delta v = c_{size} |\Delta d_h| \tag{B.35}$$

Substituting eq. B.34 into this relation (eq. B.34) one obtains

$$
\begin{aligned}
c_{size} &= c_{vol} \exp\left(v/b\right) b/a \\
&\propto c_{vol} \exp\left(v/b\right) = c_{vol} \exp\left(\frac{v}{66 \text{ ml}}\right)
\end{aligned} \tag{B.36}
$$

The resulting concentration-size distribution for raw 2 MDa dextran samples using eq.
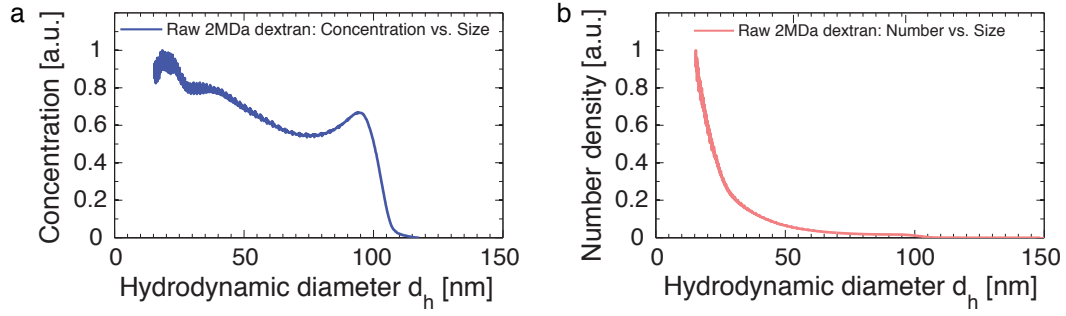
Figure B.6: Representative plots showing the transformation: a, from concentration-elution volume distribution obtained from SEC to concentration-size distribution using the relation eq. B.36; b, from concentration-size distribution to number-size distribution using relation eq. B.37.

B.36 is shown in Figure B.6a. Furthermore, using eqs. B.18 and B.22 one can obtain the number-size distribution (Figure B.6b):

$$n \propto c_{size}/M \propto \frac{c_{vol} \exp\left[v/\left(66 \text{ ml}\right)\right]}{\left(d_h\right)^{1/0.48}} \tag{B.37}$$

The estimated weight average and number average sizes based on these distributions (Figure B.6) are

$$\langle d_h \rangle_w = 42 \text{ nm} \tag{B.38}$$

$$\langle d_h \rangle_n = 25 \text{ nm} \tag{B.39}$$

and the number average of $(d_h)^3$ is

$$\left\langle \left(d_h\right)^3 \right\rangle_n = 3.2 \times 10^4 \text{ nm}^3 \tag{B.40}$$

which gives

$$\left\langle \left(d_h\right)^3 \right\rangle_n^{1/3} = 32 \text{ nm} \tag{B.41}$$

This value is in good agreement with the one (31 nm) obtained from DLS results (eq. B.26).

APPENDIX C

RESTORING FORCE CONFINING A PARTICLE IN A NETWORK CAGE

If a large particle ($d > a_x$) deviates from the center of the network cage by a small distance δr (see Figure C.1), the "elementary" network tends to drag the particle back towards its center with a restoring force f_s. As illustrated by a "dipole" model in Figure
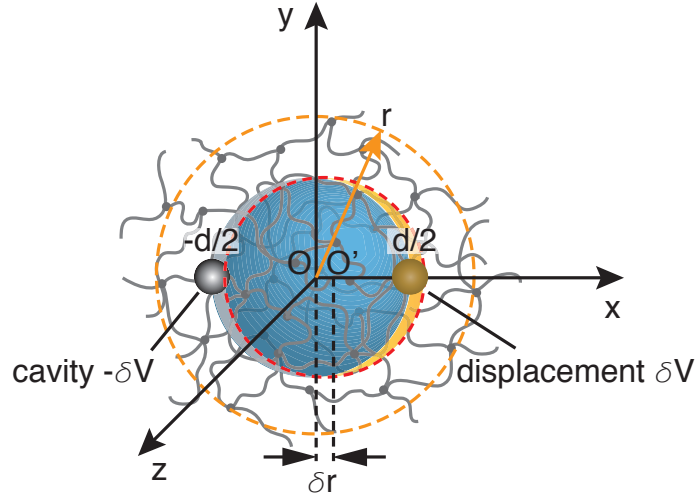
Figure C.1: "Dipole" model applied to estimate the strain in polymer network induced by the deviation of the particle of size d from position O to O' with displacement δr. The grey shadowed area corresponds to the actual volume left behind by the particle and the yellow shadowed area corresponds to the volume displaced by the particle.

C.1, the volume displaced by the large particle is $\delta V \simeq d^2 \delta r$. Meanwhile, the probe particle leaves a cavity with the same volume δV behinds it and this cavity has to be filled by the surrounding polymers. The distance between the displaced volume and the cavity is on the order the particle size d. The strain at distance r from the center of the probe particle in the "elementary" network induced by the particle motion with displacement δr is the contribution from both the displaced volume and the cavity: $\epsilon\left(r\right) = \epsilon_{\text{extra}}\left(r + d/2\right) + \epsilon_{\text{cavity}}\left(r - d/2\right)$, which gives

$$
\begin{aligned}
\epsilon\left(r\right) &\simeq -\frac{\delta V}{\left(r + d/2\right)^3} + \frac{\delta V}{\left(r - d/2\right)^3} \\
&\simeq \delta V \frac{d}{r^4} \simeq \delta r \frac{d^3}{r^4}
\end{aligned}
\tag{C.1}
$$

The above expression has a similar form to the electrostatic field induced by a dipole. Here the volume displaced by the large particle has positive value δV (analogy to the positive charge of the dipole) and the cavity can be considered with negative volume $-\delta V$ (analogy to the negative charge of the dipole). The corresponding elastic deformation energy of the "elementary" network due to the displacement of the probe particle with a deviation δr from its equilibrium position is

$$
\begin{aligned}
\Delta U_{\text{def}}\left(\delta r\right) &= k_B T \int_d^\infty \frac{1}{2}\epsilon^2\left(r\right)4\pi r^2 dr \\
&\simeq k_B T \frac{d^6\left(\delta r\right)^2}{a_x^3}\int_d^\infty \frac{1}{r^8}r^2 dr \\
&\simeq k_B T \frac{d}{a_x^3}(\delta r)^2
\end{aligned}
\tag{C.2}
$$

which is the parabolic potential cost of the displacement of a large particle from the center of the "elementary" network. Here k_B is the Boltzmann constant and T is the absolute temperature. Therefore, the restoring force is linearly proportional to the displacement of the particle from its equilibrium position.

$$
\begin{aligned}
f_s\left(\delta r\right) &\simeq \frac{\partial}{\partial r}\Delta U_{\text{def}}\left(\delta r\right) \\
&\simeq k_B T \frac{d}{a_x^3}\delta r \sim \delta r
\end{aligned}
\tag{C.3}
$$

The parabolic potential (eq. C.2) only serves as a potential well restricting fluctuation of the probe particle within the center of "elementary" networks and has nothing to do with the energy barrier of the particle hopping.

APPENDIX D

ESTIMATION OF AVERAGE LOOP SIZE IN A POLYMER NETWORK

A naive estimate for the entropic energy barrier for hopping diffusion is that each network strand is deformed from its unperturbed size a_x to the particle size d. In reality during a single hopping event the particle slips through a loop formed by network strands, which effectively lowers the extent of stretching of a single network strand. For instance, if a probe particle passes through a loop consisting of n_l network strands, each network strand is stretched from size a_x to d/n_l. Therefore, the corresponding free energy barrier becomes

$$\Delta U \simeq n_l k_B T \left(\frac{d}{n_l a_x} \right)^2 \simeq \frac{1}{n_l} k_B T \left(\frac{d}{a_x} \right)^2 \tag{D.1}$$

which implies that the energy barrier for hopping diffusion could be smaller than the value $k_B T \left(d/a_x \right)^2$ by the factor $1/n_l$.

The average loop size of an unentangled polymer network can be estimated as follows. Consider a network formed by precursor chains of functionality f, i.e., each network strand is connected to $f-1$ network strands at one of its ends. The topology of the network is fixed once the network is formed. Imagine that one randomly starts from one end of a network strand, walks along network strands, passes the crosslinks, and reaches the other end of the initial network strand after n_l steps on average, which corresponds to the average size of the loop. The number of network strands involved in the last step n_l is $(f-1)^{n_l-1}$; therefore, the total number of network strands m connected to this loop is the sum of a geometric series

$$
\begin{aligned}
m &= 1 + (f-1) + (f-1)^2 + \cdots (f-1)^{n_l-1} \\
&= \frac{(f-1)^{n_l} - 1}{f-2}
\end{aligned}
\tag{D.2}
$$

These m network strands are expected to overlap with each other. The average overlapping parameter P_x (number of network strands within the pervaded volume of a

network strand) in a polymer network is

$$P_x \simeq \frac{a_x^3}{\xi^3 \left(N_x/g\right)} \tag{D.3}$$

in which N_x corresponds to the number of monomers per network strand, ξ is the correlation length (eq. 7.1), and g corresponds to the number of monomers per correlation blob. Considering that the network strand size a_x (eq. 8.16) and the number of monomers g per correlation blob (eq. 7.1):

$$a_x \simeq \xi \left(N_x/g\right)^\nu \tag{D.4}$$

$$g \simeq (\xi/b)^{1/\nu} \tag{D.5}$$

where b corresponds to the monomer size, and ν is the scaling exponent depending on solvent quality ($\nu = 1/2$ for a theta solvent and $\nu = 3/5$ for a good solvent) [60], the overlapping parameter P_x (eq. D.3) can be rewritten as

$$
\begin{aligned}
P_x &\simeq \frac{[\xi \left(N_x/g\right)^\nu]^3}{\xi^3 \left(N_x/g\right)} \\
&\simeq \left(N_x/g\right)^{3v-1} \\
&\simeq \left(N_x\right)^{3v-1} (\xi/b)^{(1-3v)/\nu}
\end{aligned}
\tag{D.6}
$$

The average loop size n_l is given by the condition $m = P_x$, which gives

$$
\begin{aligned}
n_l &\simeq \frac{\ln\left[(f-2)\,P_x + 1\right]}{\ln\left(f-1\right)} \\
&\simeq \frac{1}{\ln\left(f-1\right)}\left[\ln\left(f-2\right) + \ln N_x\right] \\
&\simeq \frac{1}{\ln\left(f-1\right)}\ln\left(P_x\right)
\end{aligned}
\tag{D.7}
$$

The loop size has a relatively weak dependence on the size of a network strand and it adds a logarithmic correction to the energy barrier

$$
\begin{aligned}
\Delta U &\simeq \frac{1}{n_l}k_B T \left(\frac{d}{a_x}\right)^2 \\
&\simeq \frac{1}{\ln\left(P_x\right)}k_B T \left(\frac{d}{a_x}\right)^2
\end{aligned}
\tag{D.8}
$$

One would think that this logarithmic correction becomes important for estimating the corresponding waiting time for hopping diffusion since the waiting time τ_w (eq.

139

8.11) increases exponentially with the energy barrier:

$$\tau_w \sim \exp\left(\frac{\Delta U}{k_B T}\right) \sim \exp\left(\frac{d^2}{a_x^2}\frac{1}{\ln(P_x)}\right) \tag{D.9}$$

This is true if P_x is independent of network strand size a_x. However, the overlapping parameter (eq. D.3) is also a function of the network strand size: $P_x \sim a_x^{(3v-1)/\nu}$, suggesting that the waiting time

$$\tau_w \sim \exp\left(\frac{d^2}{a_x^2 \ln(a_x)}\right) \tag{D.10}$$

in which the value of the ratio $d^2/[a_x^2 \ln(a_x)]$ is dominated by the term d^2/a_x^2 (which can be numerically verified by considering the condition $d > a_x$). Therefore, the logarithmic term can be dropped if one keeps the calculation on the scaling level.

REFERENCES

[1] Ewald R. Weibel. *The Pathway for Oxygen: Structure and Function in the Mammalian Respiratory System.* Harvard University Press, Cambridge, Mass., 1984.

[2] Ewald R. Weibel, G. B. West, J. H. Brown, and B. J. Enquist. A general model for the origin of allometric scaling laws in biology. *Science*, 276:122–126, 1997.

[3] A. Wanner, M. Salathe, and T. G. O'Riordan. Mucociliary clearance in the airways. *American Journal of Respiratory and Critical Care Medicine*, 154:1868–902, 1996.

[4] T. F. Nonnenmacher, G. A. Losa, and Ewald R. Weibel. *Fractals in Biology and Medicine*. Birkhäuser Verlag, Basel ; Boston, 1994.

[5] Benoit B. Mandelbrot. *The Fractal Geometry of Nature*. W.H. Freeman, San Francisco, 1982.

[6] A. L. Goldberger and B. J. West. Fractals in physiology and medicine. *Yale Journal of Biology and Medicine*, 60:421–435, 1987.

[7] E. R. Weibel. What makes a good lung? the morphometric basis of lung function. *Swiss Medical Weekly*, 139:375–386, 2009.

[8] U. Schwab, M. Leigh, C. Ribeiro, J. Yankaskas, K. Burns, P. Gilligan, P. Sokol, and R. Boucher. Patterns of epithelial cell invasion by different species of the burkholderia cepacia complex in well-differentiated human airway epithelia. *Infection and Immunity*, 70:4547–4555, 2002.

[9] H. Matsui, B. R. Grubb, R. Tarran, S. H. Randell, J. T. Gatzy, C. W. Davis, and R. C. Boucher. Evidence for periciliary liquid layer depletion, not abnormal ion composition, in the pathogenesis of cystic fibrosis airways disease. *Cell*, 95:1005–1015, 1998.

[10] M. A. Sleigh, J. R. Blake, and N. Liron. The propulsion of mucus by cilia. *American Review of Respiratory Disease*, 137:726–741, 1988.

[11] P. M. Quinton. Physiological basis of cystic fibrosis: a historical perspective. *Physiological Reviews*, 79:S3–S22, 1999.

[12] J. J. Wine and N. S. Joo. Submucosal glands and airway defense. *Proceedings of the American Thoracic Society*, 1:47–53, 2004.

[13] J. V. Fahy and B. F. Dickey. Airway mucus function and dysfunction. *New England Journal of Medicine*, 363:2233–2247, 2010.

[14] M. Kaliner, Z. Marom, C. Patow, and J. Shelhamer. Human respiratory mucus. *Journal of Allergy and Clinical Immunology*, 73:318–323, 1984.

[15] M. R. Knowles and R. C. Boucher. Mucus clearance as a primary innate defense mechanism for mammalian airways. *Journal of Clinical Investigation*, 109:571–577, 2002.

[16] R. C. Boucher. New concepts of the pathogenesis of cystic fibrosis lung disease. *European Respiratory Journal*, 23:146–58, 2004.

[17] J. C. Hogg, F. Chu, S. Utokaparch, R. Woods, W. M. Elliott, L. Buzatu, R. M. Cherniack, R. M. Rogers, F. C. Sciurba, H. O. Coxson, and P. D. Pare. The nature of small-airway obstruction in chronic obstructive pulmonary disease. *New England Journal Of Medicine*, 350:2645–2653, 2004.

[18] R. C. Boucher. Airway surface dehydration in cystic fibrosis: Pathogenesis and therapy. In *Annual Review of Medicine*, volume 58, pages 157–170. 2007.

[19] R. Tarran, B. R. Grubb, J. T. Gatzy, C. W. Davis, and R. C. Boucher. The relative roles of passive surface forces and active ion transport in the modulation of airway surface liquid volume and composition. *Journal of of General Physiology*, 118:223–236, 2001.

[20] L. A. Clunes, C. M. Davies, R. D. Coakley, A. A. Aleksandrov, A. G. Henderson, K. L. Zeman, E. N. Worthington, M. Gentzsch, S. M. Kreda, D. Cholon, W. D. Bennett, J. R. Riordan, R. C. Boucher, and R. Tarran. Cigarette smoke exposure induces cftr internalization and insolubility, leading to airway surface liquid dehydration. *FASEB Journal*, 2011.

[21] S. A. Mortazavi, J. D. Smart, C. M. Lehr, J. A. Bouwstra, H. E. Bodde, and H. E. Junginger. A surface-energy analysis of mucoadhesion - contact-angle measurements on polycarbophil and pig intestinal-mucosa in physiologically relevant fluids. *Journal of Controlled Release*, 9:70–75, 1992.

[22] S. A. Mortazavi and J. D. Smart. An investigation into the role of water-movement and mucus gel dehydration in mucoadhesion. *Journal of Controlled Release*, 25:197–203, 1993.

[23] R. Tarran. Regulation of airway surface liquid volume and mucus transport by active ion transport. *Proceedings of the American Thoracic Society*, 1:42–6, 2004.

[24] M. Mall, B. R. Grubb, J. R. Harkema, W. K. O'Neal, and R. C. Boucher. Increased airway epithelial na+ absorption produces cystic fibrosis-like lung disease in mice. *Nature Medicine*, 10:487–493, 2004.

[25] H. Matsui, V. E. Wagner, D. B. Hill, U. E. Schwab, T. D. Rogers, B. Button, R. M. Taylor, R. Superfine, M. Rubinstein, B. H. Iglewski, and R. C. Boucher. A physical linkage between cystic fibrosis airway surface dehydration and pseudomonas aeruginosa biofilms. *Proceedings of the National Academy of Sciences of the United States of America*, 103:18131–18136, 2006.

[26] R. Bansil, E. Stanley, and J. T. Lamont. Mucin biophysics. *Annual Review of Physiology*, 57:635–657, 1995.

[27] R. Bansil and B. S. Turner. Mucin structure, aggregation, physiological functions and biomedical applications. *Current Opinion in Colloid & Interface Science*, 11:164–170, 2006.

[28] M. C. Rose and J. A. Voynow. Respiratory tract mucin genes and mucin glyco-proteins in health and disease. *Physiological Reviews*, 86:245–278, 2006.

[29] M. C. Rose. Mucins: structure, function, and role in pulmonary diseases. *American Journal of Physiology*, 263:L413–L429, 1992.

[30] D. J. Thornton, K. Rousseau, and M. A. McGuckin. Structure and function of the polymeric mucins in airways mucus. *Annual Review of Physiology*, 70:459–486, 2008.

[31] J. Bjorkander, B. Bake, V. A. Oxelius, and L. A. Hanson. Impaired lung function in patients with iga deficiency and low levels of igg2 or igg3. *New England Journal of Medicine*, 313:720–4, 1985.

[32] 3rd Ellison, R. T. and T. J. Giehl. Killing of gram-negative bacteria by lactoferrin and lysozyme. *Journal of Clinical Investigation*, 88:1080–91, 1991.

[33] K. Yamauchi, M. Tomita, T. J. Giehl, and 3rd Ellison, R. T. Antibacterial activity of lactoferrin and a pepsin-derived lactoferrin peptide fragment. *Journal of Clinical Investigation*, 61:719–28, 1993.

[34] J. Jacquot, A. Hayem, and C. Galabert. Functions of proteins and lipids in airway secretions. *European Respiratory Journal*, 5:343–58, 1992.

[35] S. Girod, C. Fuchey, C. Galabert, S. Lebonvallet, N. Bonnet, D. Ploton, and E. Puchelle. Identification of phospholipids in secretory granules of human sub-mucosal gland respiratory cells. *Journal of Histochemistry and Cytochemistry*, 39:193–8, 1991.

[36] R. S. Pillai, T. Chandra, I. F. Miller, J. Lloyd-Still, and D. B. Yeates. Work of adhesion of respiratory tract mucus. *Journal of Applied Physiology*, 72:1604–10, 1992.

[37] J. E. Sadler. Biochemistry and genetics of von willebrand factor. *Annual Review of Biochemistry*, 67:395–424, 1998.

[38] A. C. Erickson and J. R. Couchman. Still more complexity in mammalian basement membranes. *Journal of Histochemistry & Cytochemistry*, 48:1291–1306, 2000.

[39] J. Dekker, J. W. Rossen, H. A. Buller, and A. W. Einerhand. The muc family: an obituary. *Trends in Biochemical Sciences*, 27:126–31, 2002.

[40] C. L. Hattrup and S. J. Gendler. Structure and function of the cell surface (tethered) mucins. *Annual Review of Physiology*, 70:431–457, 2008.

[41] D. J. Thornton, I. Carlstedt, M. Howard, P. L. Devine, M. R. Price, and J. K. Sheehan. Respiratory mucins: identification of core proteins and glycoforms. *Biochemical Journal*, 316 (Pt 3):967–75, 1996.

[42] J. K. Sheehan, C. Brazeau, S. Kutay, H. Pigeon, S. Kirkham, M. Howard, and D. J. Thornton. Physical characterization of the muc5ac mucin: a highly oligomeric glycoprotein whether isolated from cell culture or in vivo from respiratory mucous secretions. *Biochemical Journal*, 347:37–44, 2000.

[43] G. Lamblin, M. Lhermitte, A. Klein, N. Houdret, A. Scharfman, R. Ramphal, and P. Roussel. The carbohydrate diversity of human respiratory mucins - a protection of the underlying mucosa. *American Review of Respiratory Disease*, 144:S19–S24, 1991.

[44] S. J. Gendler, G. Lamblin, S. Degroote, J. M. Perini, P. Delmotte, A. E. Scharfman, M. Davril, J. M. Lo-Guidice, N. Houdret, V. Dumur, A. Klein, and P. Roussel. Human airway mucin glycosylation: a combinatory of carbohydrate determinants which vary in cystic fibrosis. *Journal of Mammary Gland Biology and Neoplasia*, 18:661–684, 2001.

[45] D. J. Thornton and J. K. Sheehan. From mucins to mucus: toward a more coherent understanding of this essential barrier. *Proceedings of the American Thoracic Society*, 1:54–61, 2004.

[46] K. R. Bhaskar, D. Gong, R. Bansil, S. Pajevic, J. A. Hamilton, B. S. Turner, and J. T. Lamont. Profound increase in viscosity and aggregation of pig gastric mucin at low ph. *American Journal of Physiology*, 261:G827–G833, 1991.

[47] S. K. Lai, Y. Y. Wang, D. Wirtz, and J. Hanes. Micro- and macrorheology of mucus. *Advanced Drug Delivery Reviews*, 61:86–100, 2009.

[48] M. C. Rose. Characterization of human tracheobronchial mucin glycoproteins. *Methods Enzymol*, 179:3–17, 1989.

[49] I. Carlstedt, H. Lindgren, J. K. Sheehan, U. Ulmsten, and L. Wingerup. Isolation and characterization of human cervical-mucus glycoproteins. *Biochemical Journal*, 211:13–22, 1983.

[50] D. J. Thornton, J. K. Sheehan, H. Lindgren, I. Carlstedt, D. J. Thornton, J. R. Davies, M. Kraayenbrink, P. S. Richardson, J. K. Sheehan, and I. Carlstedt. Mucus glycoproteins from 'normal' human tracheobronchial secretion. *Biochemical Journal*, 265:179–86, 1990.

[51] D. J. Thornton, J. K. Sheehan, H. Lindgren, and I. Carlstedt. Mucus glycoproteins from cystic fibrotic sputum. macromolecular properties and structural 'architecture'. *Biochemical Journal*, 276:667–675, 1991.

[52] J. R. Davies, H. W. Hovenberg, C. J. Linden, R. Howard, P. S. Richardson, J. K. Sheehan, and I. Carlstedt. Mucins in airway secretions from healthy and chronic bronchitic subjects. *Biochemical Journal*, 313:431–439, 1996.

[53] B. D. Raynal, T. E. Hardingham, D. J. Thornton, and J. K. Sheehan. Concentrated solutions of salivary muc5b mucin do not replicate the gel-forming properties of saliva. *Biochemical Journal*, 362:289–96, 2002.

[54] J. K. Sheehan, K. Oates, and I. Carlstedt. Electron-microscopy of cervical, gastric and bronchial mucus glycoproteins. *Biochemical Journal*, 239:147–153, 1986.

[55] M. P. Deacon, S. McGurk, C. J. Roberts, P. M. Williams, S. J. B. Tendler, M. C. Davies, S. S. Davis, and S. E. Harding. Atomic force microscopy of gastric mucin and chitosan mucoadhesive systems. *Biochemical Journal*, 348:557–563, 2000.

[56] C. Wickstrom, J. R. Davies, G. V. Eriksen, E. C. I. Veerman, and I. Carlstedt. Muc5b is a major gel-forming, oligomeric mucin from human salivary gland, respiratory tract and endocervix: identification of glycoforms and c-terminal cleavage. *Biochemical Journal*, 334:685–693, 1998.

[57] J. K. Sheehan, M. Howard, P. S. Richardson, T. Longwill, and D. J. Thornton. Physical characterization of a low-charge glycoform of the muc5b mucin comprising the gel-phase of an asthmatic respiratory mucous plug. *Biochemical Journal*, 338:507–513, 1999.

[58] K. Rousseau, S. Kirkham, S. McKane, R. Newton, P. Clegg, and D. J. Thornton. Muc5b and muc5ac are the major oligomeric mucins in equine airway mucus. *American Journal of Physiology-Lung Cellular and Molecular Physiology*, 292:L1396–L1404, 2007.

[59] M. Kesimer, A. M. Makhov, J. D. Griffith, P. Verdugo, and J. K. Sheehan. Unpacking a gel-forming mucin: a view of muc5b organization after granular release. *American Journal of Physiology-Lung Cellular and Molecular and Molecular Physiology*, 298:L15–22, 2010.

[60] Michael Rubinstein and Ralph H. Colby. *Polymer Physics*. Oxford University Press, Oxford ; New York, 2003.

[61] N. Jentoft. Why are proteins o-glycosylated? *Trends in Biochemical Sciences*, 15:291–4, 1990.

[62] J. L. Rosenbaum and G. B. Witman. Intraflagellar transport. *Nature Reviews Molecular Cell Biology*, 3:813–825, 2002.

[63] G. R. Fulford and J. R. Blake. Mucociliary transport in the lung. *Journal of Theoretical Biology*, 121:381–402, 1986.

[64] I. Alexander, B. C. Ritchie, J. E. Maloney, and C. R. Hunter. Epithelial surfaces of the trachea and principal bronchi in the rat. *Thorax*, 30:171–7, 1975.

[65] U. Mercke, C. H. Hakansson, N. G. Toremalm, and U. Mercke. The influence of temperature on mucociliary activity. temperature range 40 degrees c to 50 degrees c. *Acta Otolaryngol*, 78:253–258, 1974.

[66] U. Mercke, C. H. Hakansson, and N. G. Toremalm. The influence of temperature on mucociliary activity. temperature range 20 degrees c-40 degrees c. *Acta Otolaryngol*, 78:444–450, 1974.

[67] C. K. Luk and M. J. Dulfano. Effect of ph, viscosity and ionic-strength changes on ciliary beating frequency of human bronchial explants. *Clinical Science*, 64:449–451, 1983.

[68] T. Sanchez, D. Welch, D. Nicastro, and Z. Dogic. Cilia-like beating of active microtubule bundles. *Science*, 333:456–9, 2011.

[69] S. K. Dutcher. Elucidation of basal body and centriole functions in chlamydomonas reinhardtii. *Traffic*, 4:443–451, 2003.

[70] H. A. Praetorius and K. R. Spring. A physiological view of the primary cilium. *Annual Review of Physiology*, 67:515–29, 2005.

[71] W. F. Marshall and S. Nonaka. Cilia: Tuning in to the cell's antenna. *Current Biology*, 16:R604–R614, 2006.

[72] P. Satir and S. T. Christensen. Overview of structure and function of mammalian cilia. *Annual Review of Physiology*, 69:377–400, 2007.

[73] M. Fliegauf, T. Benzing, and H. Omran. When cilia go bad: cilia defects and ciliopathies. *Nature Reviews Molecular Cell Biology*, 8:880–893, 2007.

[74] J. T. Eggenschwiler and K. V. Anderson. Cilia and developmental signaling. *Annual Review of Cell and Developmental Biology*, 23:345–373, 2007.

[75] C. Daghlian. Database: Powered by cilia. *Science*, 313, 2006.

[76] K. Fujiu, Y. Nakayama, A. Yanagisawa, M. Sokabe, and K. Yoshimura. Chlamydomonas cav2 encodes a voltage- dependent calcium channel required for the flagellar waveform conversion. *Current Biology*, 19:133–139, 2009.

[77] A. Desai and T. J. Mitchison. Microtubule polymerization dynamics. *Annual Review of Cell and Developmental Biology*, 13:83–117, 1997.

[78] D. Nojima, R. W. Linck, and E. H. Egelman. At least one of the protofilaments in flagellar microtubules is not composed of tubulin. *Current Biology*, 5:158–167, 1995.

[79] E. L. F. Holzbaur and R. B. Vallee. Dyneins - molecular-structure and cellular function. *Annual Review of Cell Biology*, 10:339–372, 1994.

[80] S. M. King. The dynein microtubule motor. *Biochimica Et Biophysica Acta*, 1496:60–75, 2000.

[81] I. Rodriguez-Crespo. The dynein microtubule motor: architecture and force generation, cellular roles of dynein light chain dynll and role of dynein during virus infection. *Febs Journal*, 278:2963, 2011.

[82] G. B. Witman, J. Plummer, and G. Sander. Chlamydomonas flagellar mutants lacking radial spokes and central tubules. structure, composition, and function of specific axonemal components. *Journal of Cell Biology*, 76:729–47, 1978.

[83] D. M. Woolley. Studies on the eel sperm flagellum. i. the structure of the inner dynein arm complex. *Journal of Cell Science*, 110:85–94, 1997.

[84] D. Nicastro, C. Schwartz, J. Pierson, R. Gaudette, M. E. Porter, and J. R. McIntosh. The molecular architecture of axonemes revealed by cryoelectron tomography. *Science*, 313:944–948, 2006.

[85] T. Heuser, M. Raytchev, J. Krell, M. E. Porter, and D. Nicastro. The dynein regulatory complex is the nexin link and a major regulatory node in cilia and flagella. *Journal of Cell Biology*, 187:921–933, 2009.

[86] E. F. Smith and P. F. Yang. The radial spokes and central apparatus: Mechanochemical transducers that regulate flagellar motility. *Cell Motility and the Cytoskeleton*, 57:8–17, 2004.

[87] K. G. Kozminski, K. A. Johnson, P. Forscher, and J. L. Rosenbaum. A motility in the eukaryotic flagellum unrelated to flagellar beating. *Proceedings of the National Academy of Sciences of the United States of America*, 90:5519–5523, 1993.

[88] D. G. Cole. The intraflagellar transport machinery of chlamydomonas reinhardtii. *Traffic*, 4:435–442, 2003.

[89] J. M. Scholey. Intraflagellar transport. *Annual Review of Cell and Developmental Biology*, 19:423–443, 2003.

[90] P. Satir. Studies on cilia. 3. further studies on the cilium tip and a "sliding filament" model of ciliary motility. *Journal of Cell Biology*, 39:77–94, 1968.

[91] W. L. Dentler. Structures linking the tips of ciliary and flagellar microtubules to the membrane. *Journal of Cell Science*, 42:207–220, 1980.

[92] B. Edde, J. Rossier, J. P. Lecaer, E. Desbruyeres, F. Gros, and P. Denoulet. Posttranslational glutamylation of alpha-tubulin. *Science*, 247:83–85, 1990.

[93] E. R. Dirksen. Centriole and basal body formation during ciliogenesis revisited. *Biology of the Cell*, 72:31–38, 1991.

[94] T. Benzing and B. Schermer. Transition zone proteins and cilia dynamics. *Nature Genetics*, 43:723–724, 2011.

[95] F. Hildebrandt and E. Otto. Cilia and centrosomes: a unifying pathogenic concept for cystic kidney disease? *Nature Reviews Genetics*, 6:928–940, 2005.

[96] J. A. Deane, D. G. Cole, E. S. Seeley, D. R. Diener, and J. L. Rosenbaum. Localization of intraflagellar transport protein ift52 identifies basal body transitional fibers as the docking site for ift particles. *Current Biology*, 11:1586–1590, 2001.

[97] E. T. O'Toole, T. H. Giddings, J. R. McIntosh, and S. K. Dutcher. Threedimensional organization of basal bodies from wild-type and delta-tubulin deletion strains of chlamydomonas reinhardtii. *Molecular Biology of the Cell*, 14:2999–3012, 2003.

[98] Alfred M. Lucas and L. C. Douglas. Principles underlying ciliary activity in the respiratory tract: Ii. a comparison of nasal clearance in man, monkey and other mammals. *Archives of Otolaryngology-Head & Neck Surgery*, 20:518–541, 1934.

[99] E. Houtmeyers, R. Gosselink, G. Gayan-Ramirez, and M. Decramer. Effects of drugs on mucus clearance. *European Respiratory Journal*, 14:452–467, 1999.

[100] H. Kalhoff. Mild dehydration: a risk factor of broncho-pulmonary disorders? *European Journal of Clinical Nutrition*, 57:S81–S87, 2003.

[101] D. J. Smith, E. A. Gaffney, and J. R. Blake. A model of tracer transport in airway surface liquid. *Bull. Math. Biol.*, 69:817–36, 2007.

[102] A. C. Hilding. The role of the respiratory mucosa in health and disease. *Minnesota Medicine*, 50:915–919, 1967.

[103] H. W. Hovenberg, J. R. Davies, and I. Carlstedt. Different mucins are produced by the surface epithelium and the submucosa in human trachea: identification of muc5ac as a major mucin from the goblet cells. *Biochemical Journal*, 318:319–324, 1996.

[104] B. Jachimska, M. Wasilewska, and Z. Adamczyk. Characterization of globular protein solutions by dynamic light scattering, electrophoretic mobility, and viscosity measurements. *Langmuir*, 24:6866–6872, 2008.

[105] J. H. Widdicombe and J. G. Widdicombe. Regulation of human airway surface liquid. *Respiratory Physiology*, 99:3–12, 1995.

[106] J. H. Raphael, D. A. Selwyn, S. D. Mottram, J. A. Langton, and C. O. O'Callaghan. Effects of 3 mac of halothane, enflurane and isoflurane on cilia beat frequency of human nasal epithelium in vitro. *British Journal of Anaesthesia*, 76:116–121, 1996.

[107] W. E. Finkbeiner, L. T. Zlock, M. Morikawa, A. Y. Lao, V. Dasari, and J. H. Widdicombe. Cystic fibrosis and the relationship between mucin and chloride secretion by cultures of human airway gland mucous cells. *American Journal of Physiology-Lung Cellular and Molecular Physiology*, 301:L402–L414, 2011.

[108] M. E. Monzon, S. M. Casalino-Matsuda, and R. M. Forteza. Identification of glycosaminoglycans in human airway secretions. *American Journal of Respiratory Cell and Molecular Biology*, 34:135–141, 2006.

[109] George B. Arfken and Hans-Jurgen Weber. *Mathematical Methods for Physicists*. Elsevier, Boston, 6th edition, 2005.

[110] D. Pristinski, V. Kozlovskaya, and S. A. Sukhishvili. Fluorescence correlation spectroscopy studies of diffusion of a weak polyelectrolyte in aqueous solutions. *Journal of Chemical Physics*, 122:14907, 2005.

[111] Arie J. Zuckerman, J. E. Banatvala, and J. R. Pattison. *Principles and Practice of Clinical Virology*. J. Wiley & Sons, Chichester ; New York, 4th edition, 2000.

[112] R. W. Atchison, B. C. Casto, and W. M. Hammon. Adenovirus-sssociated defective virus particles. *Science*, 149:754–756, 1965.

[113] J. Isaacson and T. C. Lubensky. Flory exponents for generalized polymer problems. *Journal de Physique Lettres*, 41:L469–L471, 1980.

[114] M. Daoud and J. F. Joanny. Conformation of branched polymers. *Journal de Physique*, 42:1359–1371, 1981.

148

[115] J. A. M. Smit, J. A. P. P. Vandijk, M. G. Mennen, and M. Daoud. Polymer sze exponents of branched dextrans. *Macromolecules*, 25:3585–3590, 1992.

[116] P. G. de Gennes. Conformations of polymers attached to an interface. *Macromolecules*, 13:1069–1075, 1980.

[117] C. M. Wijmans and E. B. Zhulina. Polymer brushes at curved surfaces. *Macromolecules*, 26:7214–7224, 1993.

[118] N. Moniaux, S. Nollet, N. Porchet, P. Degand, A. Laine, and J. P. Aubert. Complete sequence of the human mucin muc4: a putative cell membrane-associated mucin. *Biochemical Journal*, 338:325–333, 1999.

[119] M. L. Fulcher, S. Gabriel, K. A. Burns, J. R. Yankaskas, and S. H. Randell. Well-differentiated human airway epithelial cell cultures. *Methods in Molecular Medicine*, 107:183–206, 2005.

[120] C. M. Ribeiro, H. Hurd, Y. Wu, M. E. Martino, L. Jones, B. Brighton, R. C. Boucher, and W. K. O'Neal. Azithromycin treatment alters gene expression in inflammatory, lipid metabolism, and cell cycle pathways in well-differentiated human airway epithelia. *PLoS One*, 4:5806, 2009.

[121] C. J. Martens, S. K. Inglis, V. G. Valentine, J. Garrison, G. E. Conner, and S. T. Ballard. Mucous solids and liquid secretion by airways: studies with normal pig, cystic fibrosis human, and non-cystic fibrosis human bronchi. *American Journal of Physiology-Lung Cellular and Molecular Physiology*, 301:L236–46, 2011.

[122] N. O. Chahine, F. H. Chen, C. T. Hung, and G. A. Ateshian. Direct measurement of osmotic pressure of glycosaminoglycan solutions by membrane osmometry at room temperature. *Biophysical Journal*, 89:1543–1550, 2005.

[123] S. Singh, K. C. Khulbe, T. Matsuura, and P. Ramamurthy. Membrane characterization by solute transport and atomic force microscopy. *Journal of Membrane Science*, 142:111–127, 1998.

[124] M. P. Kinsky, S. M. Milner, B. Button, M. A. Dubick, and G. C. Kramer. Resuscitation of severe thermal injury with hypertonic saline dextran: Effects on peripheral and visceral edema in sheep. *Journal of Trauma: Injury, Infection, and Critical Care*, 49:844–853, 2000.

[125] L. W. Matthews, S. Spector, J. Lemm, and J. L. Potter. Studies on pulmonary secretions. i. the over-all chemical composition of pulmonary secretions from patients with cystic fibrosis, bronchiectasis, and laryngectomy. *American Review of Respiratory Disease*, 88:199–204, 1963.

[126] R. S. Baltimore, C. D. Christie, and G. J. Smith. Immunohistopathologic localization of pseudomonas aeruginosa in lungs from patients with cystic fibrosis. implications for the pathogenesis of progressive lung deterioration. *American Review of Respiratory Disease*, 140:1650–61, 1989.

[127] D. Worlitzsch, R. Tarran, M. Ulrich, U. Schwab, A. Cekici, K. C. Meyer, P. Birrer, G. Bellon, J. Berger, T. Weiss, K. Botzenhart, J. R. Yankaskas, S. Randell, R. C. Boucher, and G. Doring. Effects of reduced mucus oxygen concentration in airway pseudomonas infections of cystic fibrosis patients. *Journal of Clinical Investigation*, 109:317–25, 2002.

[128] Brian Button*, Li-Heng Cai*, Camille Ehre; Mehmet Kesimer, David B. Hill, John K. Sheehan, Richard C. Boucher, and Michael Rubinstein. Osmotic interactions between the mucus and periciliary layers determine the success or failure of mucus flow in the lung. Submitted.

[129] S. K. Lai, Y. Y. Wang, and J. Hanes. Mucus-penetrating nanoparticles for drug and gene delivery to mucosal tissues. *Advanced Drug Delivery Reviews*, 61:158–171, 2009.

[130] T. G. Mason and D. A. Weitz. Optical measurements of frequency-fependent linear viscoelastic moduli of complex fluids. *Physical Review Letters*, 74:1250–1253, 1995.

[131] T. G. Mason. Estimating the viscoelastic moduli of complex fluids using the generalized stokes-einstein equation. *Rheologica Acta*, 39:371–378, 2000.

[132] T. M. Squires and T. G. Mason. Fluid mechanics of microrheology. *Annual Review of Fluid Mechanics*, 42:413–438, 2010.

[133] T. A. Waigh. Microrheology of complex fluids. *Reports on Progress in Physics*, 68:685–742, 2005.

[134] X. Ye, P. Tong, and L. J. Fetters. Transport of probe particles in semidilute polymer solutions. *Macromolecules*, 31:5785–5793, 1998.

[135] Q. Lu and M. J. Solomon. Probe size effects on the microrheology of associating polymer solutions. *Physical Review E*, 66:061504, 2002.

[136] R. A. Omari, A. M. Aneese, C. A. Grabowski, and A. Mukhopadhyay. Diffusion of nanoparticles in semidilute and entangled polymer solutions. *Journal of Physical Chemistry B*, 113:8449–8452, 2009.

[137] H. Kang, K. H. Ahn, and S. J. Lee. Rheological properties of dilute polymer solutions determined by particle tracking microrheology and bulk rheometry. *Korea-Australia Rheology Journal*, 22:11–19, 2010.

[138] C. A. Grabowski, B. Adhikary, and A. Mukhopadhyay. Dynamics of gold nanoparticles in a polymer melt. *Applied Physics Letters*, 94:021903, 2009.

[139] A. Tuteja, M. E. Mackay, S. Narayanan, S. Asokan, and M. S. Wong. Breakdown of the continuum stokes-einstein relation for nanoparticle diffusion. *Nano Letters*, 7:1276–1281, 2007.

[140] H. Y. Guo, G. Bourret, M. K. Corbierre, S. Rucareanu, R. B. Lennox, K. Laaziri, L. Piche, M. Sutton, J. L. Harden, and R. L. Leheny. Nanoparticle motion within glassy polymer melts. *Physical Review Letters*, 102:075702, 2009.

[141] F. Amblard, A. C. Maggs, B. Yurke, A. N. Pargellis, and S. Leibler. Subdiffusion and anomalous local viscoelasticity in actin networks. *Physical Review Letters*, 77:4470–4473, 1996.

[142] J. Y. Xu, A. Palmer, and D. Wirtz. Rheology and microrheology of semiflexible polymer solutions: actin filament networks. *Macromolecules*, 31:6486–6492, 1998.

[143] D. T. Chen, E. R. Weeks, J. C. Crocker, M. F. Islam, R. Verma, J. Gruber, A. J. Levine, T. C. Lubensky, and A. G. Yodh. Rheological microscopy: local mechanical properties from microrheology. *Physical Review Letters*, 90:108301, 2003.

[144] P. A. Janmey, U. Euteneuer, P. Traub, M. Schliwa, J. Y. Xu, A. Palmer, and D. Wirtz. Rheology and microrheology of semiflexible polymer solutions: Actin filament networks. *Journal of Cell Biology*, 31:6486–6492, 1998.

[145] E. Helfer, S. Harlepp, L. Bourdieu, J. Robert, F. C. MacKintosh, and D. Chatenay. Microrheology of biopolymer-membrane complexes. *Physical Review Letters*, 85:457–460, 2000.

[146] J. Liu, M. L. Gardel, K. Kroy, E. Frey, B. D. Hoffman, J. C. Crocker, A. R. Bausch, and D. A. Weitz. Microrheology probes length scale dependent rheology. *Physical Review Letters*, 96:118104, 2006.

[147] A. Papagiannopoulos, T. A. Waigh, and T. E. Hardingham. The viscoelasticity of self-assembled proteoglycan combs. *Faraday Discussions*, 139:337–357, 2008.

[148] H. Lee, J. M. Ferrer, F. Nakamura, M. J. Lang, and R. D. Kamm. Passive and active microrheology for cross-linked f-actin networks in vitro. *Acta Biomaterialia*, 6:1207–1218, 2010.

[149] J. He and J. X. Tang. Surface adsorption and hopping cause probe-size-dependent microrheology of actin networks. *Physical Review E*, 83:041902, 2011.

[150] M. Bai, A. R. Missel, A. J. Levine, and W. S. Klug. On the role of the filament length distribution in the mechanics of semiflexible networks. *Acta Biomaterialia*, 7:2109–2118, 2011.

[151] G. Pesce, L. Selvaggi, G. Rusciano, and A. Sasso. High- and low-frequency mechanical properties of living starfish oocytes. *Journal of Biophotonics*, 4:324–334, 2011.

[152] M. Arrio-Dupont, S. Cribier, G. Foucault, P. F. Devaux, and A. d'Albis. Diffusion of fluorescently labeled macromolecules in cultured muscle cells. *Biophysical Journal*, 70:2327–2332, 1996.

[153] E. Bertseva, D. Grebenkov, S. Jeney, and L. Forro. Optical trapping microrheology in cultured human cells. *European Biophysics Journal with Biophysics Letters*, 40:158–158, 2011.

151

[154] A. S. Kozlov, D. Andor-Ardo, and A. J. Hudspeth. Anomalous brownian motion discloses viscoelasticity in the ear's mechanoelectrical-transduction apparatus. *Proceedings of the National Academy of Sciences of the United States of America*, 109:2896–2901, 2012.

[155] P. H. Wu, C. M. Hale, W. C. Chen, J. S. H. Lee, Y. Tseng, and D. Wirtz. High-throughput ballistic injection nanorheology to measure cell mechanics. *Nature Protocols*, 7:155–170, 2012.

[156] B. R. Daniels, C. M. Hale, S. B. Khatau, S. Kusuma, T. M. Dobrowsky, S. Gerecht, and D. Wirtz. Differences in the microrheology of human embryonic stem cells and human induced pluripotent stem cells. *Biophysical Journal*, 99:3563–3570, 2010.

[157] P. Kollmannsberger and B. Fabry. Linear and nonlinear rheology of living cells. In D. R. Clarke and P. Fratzl, editors, *Annual Review of Materials Research*, volume 41, pages 75–97. 2011.

[158] C. Gambini, B. Abou, A. Ponton, and A. J. M. Cornelissen. Micro- and macrorheology of jellyfish extracellular matrix. *Biophysical Journal*, 102:1–9, 2012.

[159] T. G. Mason, H. Gang, and D. A. Weitz. Rheology of complex fluids measured by dynamic light scattering. *Journal of Molecular Structure*, 383:81–90, 1996.

[160] D. J. Pine, D. A. Weitz, P. M. Chaikin, and E. Herbolzheimer. Diffusing-wave spectroscopy. *Physical Review Letters*, 60:1134–1137, 1988.

[161] T. G. Mason, K. Ganesan, J. H. vanZanten, D. Wirtz, and S. C. Kuo. Particle tracking microrheology of complex fluids. *Physical Review Letters*, 79:3282–3285, 1997.

[162] S. Rathgeber, H. J. Beauvisage, H. Chevreau, N. Willenbacher, and C. Oelschlaeger. Microrheology with fluorescence correlation spectroscopy. *Langmuir*, 25:6368–6376, 2009.

[163] R. E. Mahaffy, C. K. Shih, F. C. MacKintosh, and J. Kas. Scanning probe-based frequency-dependent microrheology of polymer gels and biological cells. *Physical Review Letters*, 85:880–883, 2000.

[164] D. Wirtz. Particle-tracking microrheology of living cells: principles and applications. *Annual Review of Biophysics*, 38:301–26, 2009.

[165] L. Lee. Mechanisms of mammalian ciliary motility: Insights from primary ciliary dyskinesia genetics. *Gene*, 473:57–66, 2011.

[166] D. Mizuno, D. A. Head, F. C. MacKintosh, and C. F. Schmidt. Active and passive microrheology in equilibrium and nonequilibrium systems. *Macromolecules*, 41:7194–7202, 2008.

[167] A. R. Bausch, W. Moller, and E. Sackmann. Measurement of local viscoelasticity and forces in living cells by magnetic tweezers. *Biophysical Journal*, 76:573–579, 1999.

[168] R. I. Cukier. Diffusion of brownian spheres in semidilute polymer solutions. *Macromolecules*, 17:252–255, 1984.

[169] G. D. J. Phillies, G. S. Ullmann, K. Ullmann, and T. H. Lin. Phenomenological scaling laws for semidilute macromolecule solutions from light-scattering by optical probe particles. *Journal of Chemical Physics*, 82:5242–5246, 1985.

[170] T. Odijk. Depletion theory of protein transport in semi-dilute polymer solutions. *Biophysical Journal*, 79:2314–2321, 2000.

[171] T. H. Fan, J. K. G. Dhont, and R. Tuinier. Motion of a sphere through a polymer solution. *Physical Review E*, 75:51405, 2007.

[172] R. Tuinier and T. H. Fan. Scaling of nanoparticle retardation in semi-dilute polymer solutions. *Soft Matter*, 4:254–257, 2008.

[173] M. Kruger and M. Rauscher. Diffusion of a sphere in a dilute solution of polymer coils. *Journal of Chemical Physics*, 131:94902, 2009.

[174] A. G. Ogston. The spaces in a uniform random suspension of fibres. *Transactions of the Faraday Society*, 54:1754–1757, 1958.

[175] A. G. Ogston, B. N. Preston, J. D. Wells, A. G. Ogston, B. N. Preston, J. M. Snowden, and J. D. Wells. Transport of compact particles through solutions of chain polymers. *Proceedings of the Royal Society of London Series a-Mathematical Physical and Engineering Sciences*, 333:297–316, 1973.

[176] A. R. Altenberger and M. Tirrell. On the theory of self-diffusion in a polymer gel. *Journal of Chemical Physics*, 80:2208–2213, 1984.

[177] L. Johansson, C. Elvingson, and J. E. Lofroth. Diffusion and interaction in gels and solutions .3. theoretical results on the obstruction effect. *Macromolecules*, 24:6024–6029, 1991.

[178] B. Amsden. Solute diffusion in hydrogels. an examination of the retardation effect. *Polymer Gels and Networks*, 6:13–43, 1998.

[179] B. Amsden. Solute diffusion within hydrogels. mechanisms and models. *Macromolecules*, 31:8382–8395, 1998.

[180] B. Amsden. An obstruction-scaling model for diffusion in homogeneous hydrogels. *Macromolecules*, 32:874–879, 1999.

[181] J. Sprakel, J. van der Gucht, M. A. C. Stuart, and N. A. M. Besseling. Rouse dynamics of colloids bound to polymer networks. *Physical Review Letters*, 99:208301, 2007.

[182] J. Sprakel, J. van der Gucht, M. A. C. Stuart, and N. A. M. Besseling. Brownian particles in transient polymer networks. *Physical Review E*, 77:061502, 2008.

[183] S. A. Egorov. Anomalous nanoparticle diffusion in polymer solutions and melts: A mode-coupling theory study. *Journal of Chemical Physics*, 134:084903, 2011.

[184] U. Yamamoto and K. S. Schweizer. Theory of nanoparticle diffusion in unentangled and entangled polymer melts. *Journal of Chemical Physics*, 135:224902, 2011.

[185] L. Masaro and X. X. Zhu. Physical models of diffusion for polymer solutions, gels and solids. *Progress in Polymer Science*, 24:731–775, 1999.

[186] P. G. de Gennes. Dynamics of entangled polymer-solutions .2. inclusion of hydrodynamic interactions. *Macromolecules*, 9:594–598, 1976.

[187] Pierre-Gilles de Gennes. *Scaling Concepts in Polymer Physics*. Cornell University Press, Ithaca, N.Y., 1979.

[188] M. Doi and S. F. Edwards. *The Theory of Polymer Dynamics*. Clarendon Press; Oxford University Press, Oxford; New York, 1988.

[189] F. B. Wyart and P. G. de Gennes. Viscosity at small scales in polymer melts. *European Physical Journal E*, 1:93–97, 2000.

[190] L. H. Cai, S. Panyukov, and M. Rubinstein. Mobility of nonsticky nanoparticles in polymer liquids. *Macromolecules*, 44:7853–7863, 2011.

[191] F. Brochard-Wyart, A. Ajdari, L. Leibler, M. Rubinstein, and J. L. Viovy. Dynamics of stars and linear-chains dissolved in a polymer melt. *Macromolecules*, 27:803–808, 1994.

[192] A. N. Semenov and M. Rubinstein. Thermoreversible gelation in solutions of associative polymers. 1. statics. *Macromolecules*, 31:1373–1385, 1998.

[193] J. Liu, D. P. Cao, and L. Q. Zhang. Molecular dynamics study on nanoparticle diffusion in polymer melts: A test of the stokes-einstein law. *Journal of Physical Chemistry C*, 112:6653–6661, 2008.

[194] F. Hamada, S. Kinugasa, H. Hayashi, and A. Nakajima. Small-angle x-ray-scattering from semidilute polymer-solutions .1. polystyrene in toluene. *Macromolecules*, 18:2290–2294, 1985.

[195] James E. Mark. *Physical Properties of Polymers Handbook*. Springer, 2 edition, 2007.

[196] D. C. Rapaport. *The Art of Molecular Dynamics Simulation*. Cambridge University Press, Cambridge, UK ; New York, NY, 2nd edition, 2004.

[197] Suresh N. Chinai and Rudolph A. Guzzi. Poly-n-butyl methacrylate. iii. dilute solution properties by viscosity and light scattering. *Journal of Polymer Science*, 21:417–426, 1956.

[198] M. Kroger, W. Loose, and S. Hess. Rheology and structural changes of polymer melts via nonequilibrium molecular dynamics. *Journal of Rheology*, 37:1057–1079, 1993.

[199] F. Ould-Kaddour and D. Levesque. Molecular-dynamics investigation of tracer diffusion in a simple liquid: test of the stokes-einstein law. *Physical Review E*, 63:011205, 2001.

[200] S. Sen, S. K. Kumar, and P. Keblinski. Viscoelastic properties of polymer melts from equilibrium molecular dynamics simulations. *Macromolecules*, 38:650–653, 2005.

[201] F. Brochard and P. G. de Gennes. Shear-dependent slippage at a polymer solid interface. *Langmuir*, 8:3033–3037, 1992.

[202] S. K. Lai, D. E. O'Hanlon, S. Harrold, S. T. Man, Y. Y. Wang, R. Cone, and J. Hanes. Rapid transport of large polymeric nanoparticles in fresh undiluted human mucus. *Proceedings of the National Academy of Sciences of the United States of America*, 104:1482–1487, 2007.

[203] S. K. Lai, Y. Y. Wang, K. Hida, R. Cone, and J. Hanes. Nanoparticles reveal that human cervicovaginal mucus is riddled with pores larger than viruses. *Proceedings of the National Academy of Sciences of the United States of America*, 107:598–603, 2010.

[204] M. Rubinstein and S. Panyukov. Nonaffine deformation and elasticity of polymer networks. *Macromolecules*, 30:8036–8044, 1997.

[205] R. P. Sijbesma, F. H. Beijer, L. Brunsveld, B. J. Folmer, J. H. Hirschberg, R. F. Lange, J. K. Lowe, and E. W. Meijer. Reversible polymers formed from self-complementary monomers using quadruple hydrogen bonding. *Science*, 278:1601–1604, 1997.

[206] Ronald F. M. Lange, M. Van Gurp, and E. W. Meijer. Hydrogen-bonded supramolecular polymer networks. *Journal of Polymer Science Part A: Polymer Chemistry*, 37:3657–3670, 1999.

[207] Philippe Cordier, François Tournilhac, Corinne Soulié-Ziakovic, and Ludwik Leibler. Self-healing and thermoreversible rubber from supramolecular assembly. *Nature*, 451:977–980, 2008.

[208] Ludwik Leibler, Michael Rubinstein, and Ralph H. Colby. Dynamics of reversible networks. *Macromolecules*, 24:4701–4707, 1991.

[209] Michael Rubinstein and Alexander N. Semenov. Thermoreversible gelation in solutions of associating polymers. 2. linear dynamics. *Macromolecules*, 31:1386–1397, 1998.

[210] Michael Rubinstein and Alexander N. Semenov. Dynamics of entangled solutions of associating polymers. *Macromolecules*, 34:1058–1068, 2001.

[211] A. N. Semenov and Michael Rubinstein. Dynamics of entangled associating polymers with large aggregates. *Macromolecules*, 35:4821–4837, 2002.

[212] Evgeny B. Stukalin, N. Arun Kumar, Li-Heng Cai, Ludwik Leibler, and Michael Rubinstein. Self-healing of unentangled polymer networks with reversible bonds. To be submitted.

[213] R. Tarran and R. C. Boucher. Thin-film measurements of airway surface liquid volume/composition and mucus transport rates in vitro. *Methods in Molecular Medicine*, 70:479–492, 2002.

[214] H. C. van de Hulst. *Light Scattering by Small Particles*. Dover Publications, New York, 1981.

[215] Bruce J. Berne and Robert Pecora. *Dynamic Light Scattering: with Applications to Chemistry, Biology, and Physics*. Dover Publications, Mineola, N.Y., 2000.

[216] D. E. Koppel. Analysis of macromolecular polydispersity in intensity correlation spectroscopy: the method of cumulants. *Journal of Chemical Physics*, 57:4814, 1972.

[217] R. Finsy. Particle sizing by quasi-elastic light-scattering. *Advances in Colloid and Interface Science*, 52:79–143, 1994.

[218] B. J. Frisken. Revisiting the method of cumulants for the analysis of dynamic light-scattering data. *Applied Optics*, 40:4087–4091, 2001.

[219] www.malvern.com/common/downloads/campaign/mrk656-01.pdf.

[220] E. Nordmeier. Static and dynamic light-scattering solution behavior of pullulan and dextran in comparison. *Journal of Physical Chemistry*, 97:5770–5785, 1993.

[221] Andre M. Striegel. *Modern Size-Exclusion Liquid Chromatography: Practice of Gel Permeation and Gel Filtration Chromatography*. Wiley, Hoboken, N.J., 2nd edition, 2009.